THE UNIVERSITY OF QUEENSLAND

AUSTRALIA

Frontiers of Quantum Optics: photonics tolls, computational complexity, quantum metrology, and quantum correlations.

Raphael Akel Abrahão

M. Eng.

A thesis submitted for the degree of Doctor of Philosophy at

The University of Queensland in 2020

School of Mathematics and Physics

Abstract

The concept that light comes in discrete units of energy, the quantum of light named photon, is a cornerstone of Quantum Physics. Current technology allow experimentalists to generate, manipulate and detect photons in ways only imaginable for the earlier formulators of Quantum Physics. Nowadays, we can use photons to test fundamental aspects of Quantum Physics, as well as to develop applications, specially in the fields of quantum computation, communication, cryptography, metrology and sensing.

This thesis aims to explore the frontiers of Quantum Optics in 4 fronts: (1) quantum photonics tools, (2) quantum computing and computational complexity, (3) quantum metrology, and (4) quantum correlations. The research presented here can be formulated in 4 respective questions:

- How to prepare a state with a large number of single photons?
  Using our Multiple Channel Optical Switcher photonic chip.

- How to scale Boson Sampling experiments, specially to a regime where it is closer to the quantum computational advantage and/or can challenge the Extended Church-Turing Thesis?
  Combining continuous-variables optical technology with temporal encoding.

- How to demonstrate an optimal method to estimate the spacial characteristics of a distant source of thermal light?
  Using recent advances in quantum metrology and number-resolving photon detectors.

- Are there quantum correlations beyond entanglement and discord?
  Probably yes.

Of course, even to better understand what each of these questions and answers mean, it is necessary a minimum background which I tried to provide in the beginning of the thesis and in each chapter. The reader will find out the details of each of these questions and answers. I wish you a good reading!

Declaration by author

This thesis is composed of my original work, and contains no material previously published or written by another person except where due reference has been made in the text. I have clearly stated the contribution by others to jointly-authored works that I have included in my thesis.

I have clearly stated the contribution of others to my thesis as a whole, including statistical assistance, survey design, data analysis, significant technical procedures, professional editorial advice, financial support and any other original research work used or reported in my thesis. The content of my thesis is the result of work I have carried out since the commencement of my higher degree by research candidature and does not include a substantial part of work that has been submitted to qualify for the award of any other degree or diploma in any university or other tertiary institution. I have clearly stated which parts of my thesis, if any, have been submitted to qualify for another award.

I acknowledge that an electronic copy of my thesis must be lodged with the University Library and, subject to the policy and procedures of The University of Queensland, the thesis be made available for research and study in accordance with the Copyright Act 1968 unless a period of embargo has been approved by the Dean of the Graduate School.

I acknowledge that copyright of all material contained in my thesis resides with the copyright holder(s) of that material. Where appropriate I have obtained copyright permission from the copyright holder to reproduce material in this thesis and have sought permission from co-authors for any jointly authored works included in the thesis.

Publications included in this thesis

1. [1] F. Lenzini, B. Haylock, J. C. Loredo, **R. A. Abrahão**, N. A. Zakaria, S. Kasture, I. Sagnes, A. Lemaitre, H.-P. Phan, D. V. Dao, P. Senellart, M. P. Almeida, A. G. White, and M. Lobino, Active demultiplexing of single photons from a solid-state source, *Laser Photonics Reviews* 11, No. 3, 1600297, 2017.

2. [2] L. A. Howard, G. G. Gillett, M. E. Pearce, **R. A. Abrahao**, T. J. Weinhold, P. Kok, A. G. White, Optimal imaging of remote bodies using quantum detectors, *Physical Review Letters* 123, 143604, 2019.

Submitted manuscripts included in this thesis

1. [3] **Raphael A. Abrahao** and Austin P. Lund, Continuous-Variables Boson Sampling: Scaling and Verification, *arXiv:1812.08978*, 2018.

Other publications during candidature

Conference abstracts

1. R. A. Abrahão, F. Shahandeh, G. Gillet, M. Ringbauer, M. P. Almeida, T. C. Ralph and A. G. White, "The Quest for Nonclassicality using Number-Resolving Single-Photon Detectors", in Australian and New Zealand Conference on Optics and Photonics (ANZCOP) 2017, Queenstown, New Zealand.

2. [4] R. A. Abrahão, F. Shahandeh, G. Gillett, M. Ringbauer, T. Weinhold, M. P. Almeida, T. C. Ralph, and A. G. White, "The Quest for Nonclassicality using Number-Resolving Single-Photon Detectors", in Frontiers in Optics / Laser Science, OSA Technical Digest (Optical Society of America, 2018), paper JTu2A.55.

Contributions by others to the thesis

Before Chapters 2, 3, 4 and 5, the contributions of each author for each project are stated.

Statement of parts of the thesis submitted to qualify for the award of another degree

No works submitted towards another degree have been included in this thesis.

Research involving human or animal subjects

No animal or human subjects were involved in this research.

Acknowledgments

I would like to sincerely thank my PhD Advisory team: Prof. Andrew White, Dr Till Weinhold, Dr Austin Lund, and Dr Martin Ringbauer. In particular, without limiting to, I would like to thank Prof. Andrew White for the opportunity to study on the Quantum Technology Laboratory (QT Lab) and for the encouragement to take different projects; Dr Till Weinhold for many assistances in different parts of my PhD, from technical questions in the lab to general candidature help; Dr Austin Lund for his help on theoretical physics (and the best Quantum Physics discussion in a beachfront bar); and Dr Martin Ringbauer for pointing me in the direction of quantum foundations, a truly deep influence. Certainly was a special time of my life. My heartfelt gratitude!

I would like to extend my gratitude to Dr Marcelo de Almeida, specially for his help during my first year, Dr Jacquiline Romero and all my fellow PhD students in the QT Lab. Additionally, I would like to thank Dr Magdalena Zych for the many interesting discussions about General Relativity and Quantum Physics. Also, I would like to thank all the people that contributed to the projects presented in this thesis.

This PhD was immensely facilitated by the extraordinary work of many University of Queensland staffs, especially Angela Bird, Murray Kane, Jonathan Paul, and Dr Timo Nieminen.

I also would like to thank Dr Nathan Langford, who provided me encouragement, advice and support though the EQUS Mentorship Program.

Muito obrigado!

Financial support

This research was supported by the University of Queensland International Scholarship (UQI), Australian Research Council Centre of Excellence for Engineered Quantum Systems (EQUS), and Australian Research Council Centre of Excellence for Quantum Computation and Communication Technology (CQC2T).

Keywords

Quantum Physics, optics, metrology, correlations, photonics, computational complexity.

Australian and New Zealand Standard Research Classifications (ANZSRC)

ANZSRC code: 020604, Quantum Optics, 100%

Fields of Research (FoR) Classification

FoR code: 0206, Quantum Physics, 100%

To God

To Amanda Akel Abrahão, *in memoriam*

To Mario Isaac Abrahão, *in memoriam*

To Constantino Nicolau Akel, *in memoriam*

To my beloved wife, Renata

To my beloved children, Mario, Amanda and Miguel

To my beloved father and mother, Sergio and Irlane

To my beloved grandmothers, Lily and Irene

To my siblings, Gabriel and Mariana

Sacred Heart of Jesus, in whom are all treasures of wisdom and knowledge, have mercy on us.

Immaculate Heart of Mary, pray for us.

Saint Joseph, pray for us.

Contents

List of figures

List of tables

Preamble: the study of Quantum Optics

From Eratosthenes's measurement of the circumference of Earth in ancient times through the observations of shadows, to the detection of gravitational waves with optical interferometry [5], light has played a pivotal role in the development of Physics. Either as a tool or as the main subject, light has enriched scientists with many properties to explore. The emergence of Modern Physics from the blackbody radiation problem and the Michelson-Morley experiment was only possible through a detailed understanding of the fundamental properties of light. Nowadays, the technologies based on light are ubiquitous, ranging from fiber-optic communication to medical imaging. The reader of this thesis very likely only had access to this material because of these optical technologies. Even the reading of it relies on the optical system of the eyes.

Motivated by the ever-fascinating field of optics, this thesis aims to explore the frontier of optics: the field of quantum optics. As illustrated in Fig 0.1 which contains a few examples of concepts and applications, quantum optics takes into account all the known observed properties of light as explained by quantum mechanics. For obvious reasons, our scope in this thesis is limited to a few concepts. Chapter 1 introduces the concept of photon and the fundamentals of single-photon sources. Chapter 2 presents our photonic chip called Multiple Channel Optical Switcher (MuChOS). Chapter 3 presents our theoretical proposal to scale Boson Sampling experiments by combining continuous variables quantum information and temporal encoding. Chapter 4 explains an optimal approach to imaging via photon counting. Chapter 5 presents the experimental progress in our project to demonstrate a new kind of quantum correlation even in the absence of other correlations such as quantum entanglement and quantum discord. Finally, Chapter 6 presents the conclusion and outlook.

Detailed introduction to quantum optics can be found in References [6–14], while the formalism of quantum mechanics is well explained in Reference [15]. For optical quantum information processing, see Ref. [16].

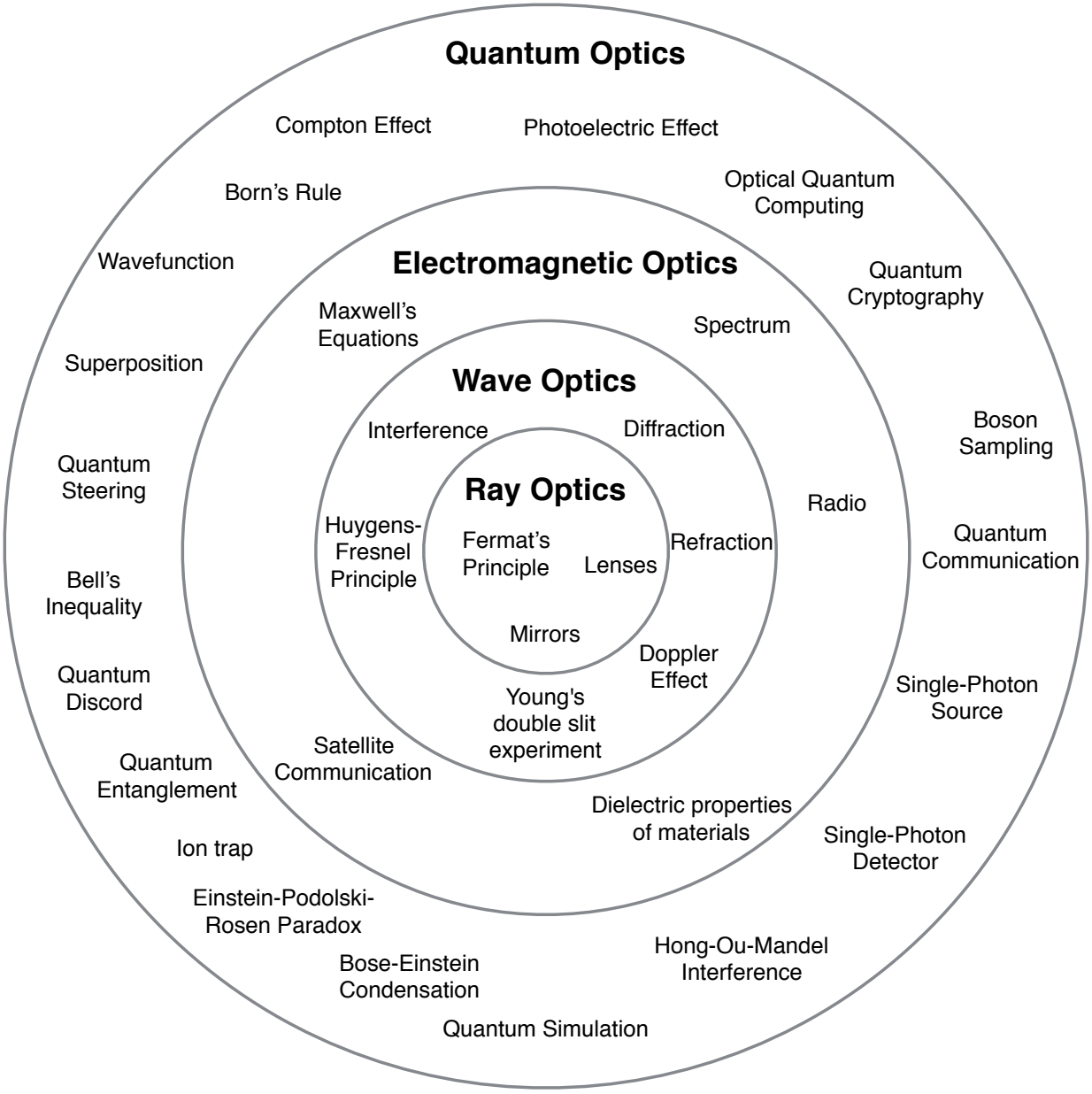

Figure 0.1: Conceptual diagram of optics. From the most simple explanation, ray optics, then wave optics, electromagnetic optics, until the most advanced explanation in quantum optics. Each subset presents a list of phenomena and technologies associated with the corresponding description of light.

Chapter 1

Fundamentals of Single-Photon Sources

1.1 What is a photon?

In this Chapter, we will discuss the background for this thesis and present the fundamentals of single-photon sources. Firstly, let us define the photon: the fundamental particle of light and the particle responsible to mediate the electromagnetic force. For a more operational definition, one can take the fundamental process which generates a photon. Consider an atom and its discrete energy levels, also known as quantised levels. Take two of the levels, here named "excited" and "ground" as in Figure 1.1. When the atom changes its state from the excited state to the ground states, the energy difference is released as a discrete packet of light, a photon. This process is described by Planck's relation $\Delta E = hf$, where the energy difference of the two levels is given by ΔE, h is Planck's constant ($h = 6.626070040$ x$10^{-34} Js$), and f is the frequency of the emitted photon. In addition to that, the photon is a spin-1 particle and obeys the Bose-Einstein distribution.

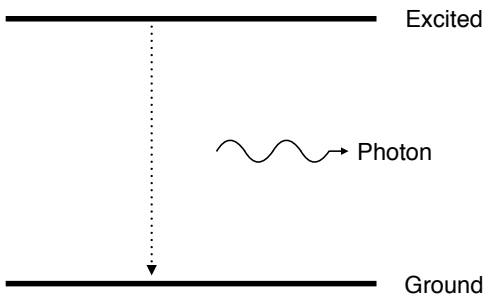

Figure 1.1: A two-level model of the energy levels of an atom. If the atom is in the excited state and decays to the ground state, the corresponding energy difference will be emitted as a single photon.

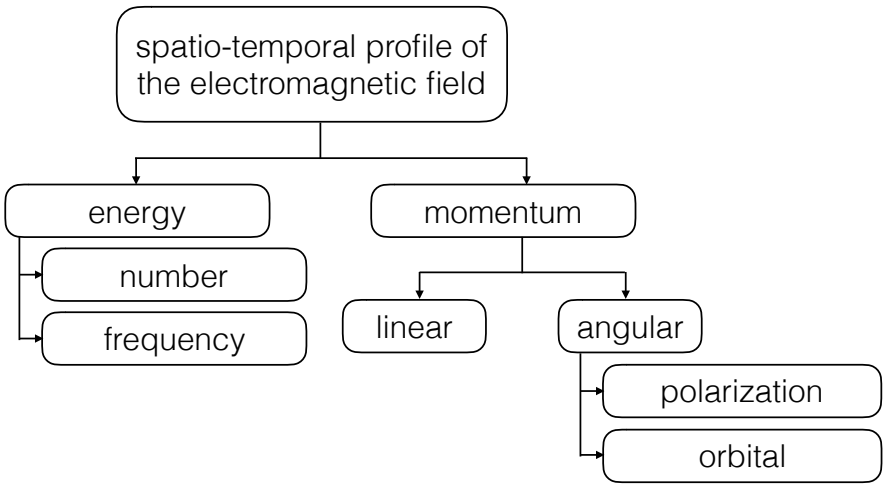

Figure 1.2: The spatio-temporal profile of the electromagnetic field can be decomposed into two components: energy and momentum. The further details are explained in the main text.

1.1.1 Properties of photons

The different degrees of freedom for the photon are manifested in the spatio-temporal profile of the electromagnetic field. The spatio-temporal profile of the electromagnetic field can be decomposed into two components: energy and momentum. The energy component relates to the frequency ω and to the number of photons n. The momentum component decomposes as a linear and an angular part. The linear momentum leads to the wavenumber $\vec{k}$. On the other hand, the angular component leads to two properties: (1) under the paraxial approximation, to polarization, and (2) to the orbital angular momentum (OAM). See Fig. 1.2. The reader may be already familiar with these concepts, but an explanation of each of these properties can be found in many books [17, 18]. Each of these properties is a degree of freedom for encoding information, with polarization being one of the most commonly used in optical quantum computing.

1.2 Metrics of single-photon sources

If any light source, such as a light bulb, produces photons, what differentiate light sources? Are the photons produced in any kind of source equally good for any application? Why not using light bulbs for quantum optics experiments? The general answer is simple: for quantum optics experiments one wishes the ability to produce a single photon with controlled properties in each production event. Then, the particular application will require photons with specific properties. Thus, we must discuss some metrics to differentiate single-photon sources.

1.2.1 Photon number purity (a.k.a single-photon purity or multiphoton suppression)

The idea that photons are discrete units leads to the concept of number state representation, in which a state is represented by the number of particles that occupy that state [6], simply named Fock state. From Reference [6], one will found the following definition:

> "We therefore describe the excitations of the quantized electromagnetic field in terms of the number of photons excited at angular frequency ω. The **photon number state** $|n\rangle$ then represents a monochromatic quantized field of angular frequency ω containing n photons." (Reference [6], page 156)

An ideal single-photon source should emit only one single photon (Fock state $|1\rangle$) and no higher order Fock states ($|n\rangle$, for $n > 1$). The number purity[1] is used to quantify the contribution of these higher order Fock terms and is measured using the **second-order correlation function** $g^{(2)}(0)$, in which intensity fluctuations for two detected photons from the same source are observed. This function quantifies intensity correlations and is also called degree of second-order coherence. In terms of number basis, we have the following equation:

$$g^{(2)}(0) = \frac{n(n-1)}{n^2}. \tag{1.1}$$

From Eq. 1.1, one can see that an ideal single-photon source has $g^{(2)}(0) = 0$. The presence of higher Fock terms will necessarily increase the value of $g^{(2)}(0)$, and that is why the number purity is also called single-photon purity or multiphoton suppression. The derivation of Eq. 1.1 can be found below.

Second-order correlation function $g^{(2)}(0)$ derivation.
Note: the derivation presented here follows the steps of *Quantum Optics: An Introduction* by Mark Fox [6].

Consider a 50:50 beamsplitter were E_1 and E_2 are the input fields, and E_3 and E_4 are the output fields, see Fig.1.3. The phase shifts of the field on transmission and reflection are ϕ_i^t and ϕ_i^r, respectively, with $i = 1,2$. The fields E_1 and E_2 are assumed to be real. The coefficients of transmission and reflection are T and R, and due to normalization, $|T|^2 + |R|^2 = 1$. Then $T = R = \frac{1}{\sqrt{2}}$.

For the E_3:

$$E_3 = TE_1 e^{i\phi_1^t} + RE_2 e^{i\phi_2^r} \tag{1.2}$$

$$E_3 = \frac{1}{\sqrt{2}}(E_1 e^{i\phi_1^t} + E_2 e^{i\phi_2^r}). \tag{1.3}$$

[1] Not to be confused with spectral purity.

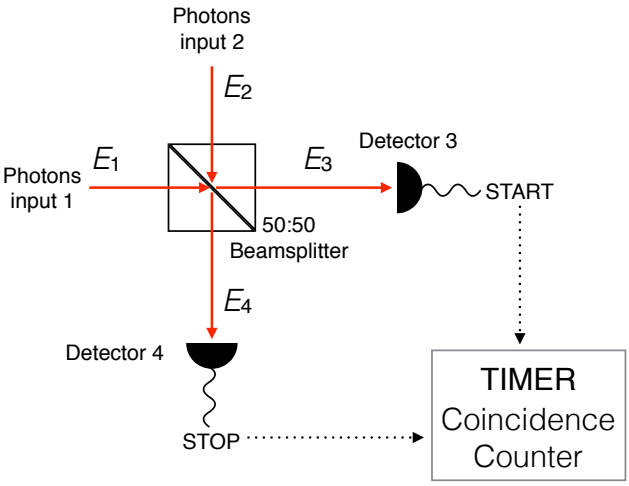

Figure 1.3: Photons at a 50:50 beamsplitter. E_1 and E_2 are the input classical fields, and E_3 and E_4 are the output classical fields. Detectors 3 and 4 are single-photon detectors. These are also connected to a timer that registers coincidence counts. This figure will assist us on the derivation of second-order correlation function $g^{(2)}(0)$ and the Hong-Ou-Mandel effect. It also accounts for the quantum version of the intensity interferometer of the Hanbury Brown–Twiss (HBT) experiment. Figure adapted from [6].

Likewise, for E_4:

$$E_4 = RE_1 e^{i\phi_1^r} + TE_2 e^{i\phi_2^t} \tag{1.4}$$

$$E_4 = \frac{1}{\sqrt{2}}(E_1 e^{i\phi_1^r} + E_2 e^{i\phi_2^t}). \tag{1.5}$$

Next, we must apply conservation of energy. The energy density is given by $u = \frac{1}{2}\varepsilon|\vec{E}|^2$, where ε is the permittivity of the medium. So,

$$u_1 + u_2 = u_3 + u_4 \tag{1.6}$$

$$\frac{1}{2}\varepsilon|E_1|^2 + \frac{1}{2}\varepsilon|E_2|^2 = \frac{1}{2}\varepsilon|E_3|^2 + \frac{1}{2}\varepsilon|E_4|^2 \tag{1.7}$$

$$|E_1|^2 + |E_2|^2 = |E_3|^2 + |E_4|^2. \tag{1.8}$$

Using the property $|E|^2 = EE^*$, then:

$$|E_1|^2 + |E_2|^2 = \frac{1}{2}[E_1 e^{i\phi_1^t} + E_2 e^{i\phi_2^r}][E_1 e^{-i\phi_1^t} + E_2 e^{-i\phi_2^r}] + \frac{1}{2}[E_1 e^{i\phi_1^r} + E_2 e^{i\phi_2^t}][E_1 e^{-i\phi_1^r} + E_2 e^{-i\phi_2^t}] \tag{1.9}$$

$$= \frac{1}{2}[E_1^2 e^{i(\phi_1^t - \phi_1^t)} + \underbrace{E_1 E_2 e^{i(\phi_1^t - \phi_2^r)}}_{A} + \underbrace{E_2 E_1 e^{i(\phi_2^r - \phi_1^t)}}_{B} + E_2^2 e^{i(\phi_2^r - \phi_2^r)}] \tag{1.10}$$

$$+\frac{1}{2}[E_1^2 e^{i(\phi_1^r - \phi_1^r)} + \underbrace{E_1 E_2 e^{i(\phi_1^r - \phi_2^t)}}_{C} + \underbrace{E_2 E_1 e^{i(\phi_2^t - \phi_1^r)}}_{D} + E_2^2 e^{i(\phi_2^t - \phi_2^t)}] \tag{1.11}$$

$$= \frac{1}{2}[2E_1^2 + 2E_2^2 + (A + B + C + D)] \tag{1.12}$$

$$= E_1^2 + E_2^2 + \frac{1}{2}(A + B + C + D). \tag{1.13}$$

Therefore,

$$E_1^2 + E_2^2 = E_1^2 + E_2^2 + \frac{1}{2}(A+B+C+D) \tag{1.14}$$

$$\Rightarrow \frac{1}{2}(A+B+C+D) = 0 \tag{1.15}$$

$$\Rightarrow A+B+C+D = 0. \tag{1.16}$$

Now, working with the $A+B+C+D=0$ terms and using Euler's identity $e^{i\theta} = \cos\theta + i\sin\theta$:

$$E_1E_2[e^{i(\phi_1^t-\phi_2^r)} + e^{i(\phi_2^r-\phi_1^t)} + e^{i(\phi_1^r-\phi_2^t)} + e^{i(\phi_2^t-\phi_1^r)}] = 0 \tag{1.17}$$

$$E_1E_2[\underbrace{e^{-i(\phi_2^r-\phi_1^t)} + e^{i(\phi_2^r-\phi_1^t)}} + \underbrace{e^{i(\phi_1^r-\phi_2^t)} + e^{-i(\phi_1^r-\phi_2^t)}}] = 0 \tag{1.18}$$

$$E_1E_2[2\cos(\phi_2^r-\phi_1^t) + 2\cos(\phi_1^r-\phi_2^t)] = 0 \tag{1.19}$$

$$\Rightarrow \cos(\phi_2^r-\phi_1^t) + \cos(\phi_1^r-\phi_2^t) = 0. \tag{1.20}$$

So, in order to obey conservation of energy, the condition on Eq. 1.20 must be fulfilled. The phase change in transmission is assumed to be zero, then, Eq.1.20 turns into:

$$\cos(\phi_2^r) + \cos(\phi_1^r) = 0. \tag{1.21}$$

Equation 1.21, and thus conservation of energy, is satisfied when there is a π phase shift between the two reflections. To verify so:

$$\phi_2^r - \phi_1^r = \pi \Rightarrow \phi_2^r = \phi_1^r + \pi, \tag{1.22}$$

then,

$$\cos(\pi+\phi_1^r) + \cos(\phi_1^r) = 0 \tag{1.23}$$

$$\cos(\pi)\cos(\phi_1^r) - \sin(\pi)\sin(\phi_1^r) + \cos(\phi_1^r) = 0 \tag{1.24}$$

$$-\cos(\phi_1^r) + \cos(\phi_1^r) = 0 \Rightarrow 0 = 0. \tag{1.25}$$

Therefore, when there is a relative phase shift of π between the two reflections, we satisfy the conservation of energy. We find (without loss of generality), the description of the classical output fields:

$$E_3 = \frac{1}{\sqrt{2}}(E_1 - E_2) \tag{1.26}$$

$$E_4 = \frac{1}{\sqrt{2}}(E_1 + E_2). \tag{1.27}$$

The minus sign on Eq. 1.26 could have been applied to Eq. 1.27 instead. This makes no difference, provided the minus sign from the π phase shift from reflection is applied to one of the fields equations. The classical field equation can then be converted to a quantum mechanical description using creation ($\hat{a}^\dagger$) and annihilation ($\hat{a}$) operators:

$$\hat{a}_3 = \frac{1}{\sqrt{2}}(\hat{a}_1 - \hat{a}_2) \tag{1.28}$$

$$\hat{a}_4 = \frac{1}{\sqrt{2}}(\hat{a}_1 + \hat{a}_2). \tag{1.29}$$

The Hermitian conjugate expressions are:

$$\hat{a}_3^\dagger = \frac{1}{\sqrt{2}}(\hat{a}_1^\dagger - \hat{a}_2^\dagger) \tag{1.30}$$

$$\hat{a}_4^\dagger = \frac{1}{\sqrt{2}}(\hat{a}_1^\dagger + \hat{a}_2^\dagger). \tag{1.31}$$

The results in Eq. 1.28–1.31 will be used shortly.

In Fig. 1.3, Detector 3 (D3) and Detector 4 (D4) are single-photon detectors working on a "click/no-click" basis, i.e. when at least one single photon is detected, the detector clicks. Then, a signal is sent to a timer. Detector 3 is connect to a "start" port on the timer, while Detector 4 is connect to a "stop" port. Doing so, the timer can register the time difference between detection events from D3 and D4 and acts as a coincidence counter. Say a detection event occurs in D3 at the given time t, and another detection event occurs in D4 at $t+\tau$. Then, the timer will record it as a coincidence count in the time interval τ. Repeating this experimental run many times, a histogram of the detection events can be made for each time interval τ. Normalizing these counts to the total number of counts in both D3 and D4, leads to the time-dependent second-order correlation function $g^{(2)}(\tau)$:

$$g^{(2)}(\tau) = \frac{\langle n_3(t) n_4(t+\tau)\rangle}{\langle n_3(t)\rangle\langle n_4(t+\tau)\rangle}, \tag{1.32}$$

where $n_3(t)$ and $n_4(t)$ are the counts detected in D3 and D4, respectively, for a given time t, and $\langle\cdots\rangle$ represents the expectation value for a given input state and over many experimental runs.

We will use the following Quantum Optics formulas [6, 15]:

$$[\hat{a}_i, \hat{a}_j^\dagger] = \hat{a}_i\hat{a}_j^\dagger - \hat{a}_j^\dagger\hat{a}_i = \delta_{ij} = \begin{cases} 1 & \text{, if } i = j \\ 0 & \text{, if } i \neq j \end{cases} \tag{1.33}$$

where δ_{ij} is the Kronecker delta.

$$\hat{n} = \hat{a}^\dagger\hat{a} \text{ (number operator definition)} \tag{1.34}$$

$$\hat{n}\,|n\rangle = n\,|n\rangle \text{ (eigenvalue equation for the number operator)} \tag{1.35}$$

$$\hat{a}^\dagger\,|n\rangle = \sqrt{n+1}\;\,|n+1\rangle \text{ (creation operator action on a number state)} \tag{1.36}$$

$$\hat{a}\,|n\rangle = \sqrt{n}\;\,|n-1\rangle \text{ (annihilation operator action on a number state)} \tag{1.37}$$

$$\hat{a}\,|0\rangle = 0 \text{ (annihilation operator acting on a vacuum state)} \tag{1.38}$$

$$\langle 0|\,\hat{a}^\dagger = 0 \text{ (Hermitian conjugate of Eq. 1.38)} \tag{1.39}$$

Rewriting the time-dependent second-order correlation function $g^{(2)}(\tau)$ (Eq. 1.32) using the number operator formula (Eq. 1.34), one obtains:

$$g^{(2)}(\tau) = \frac{\langle \hat{a}_3^\dagger(t)\hat{a}_3(t)\hat{a}_4^\dagger(t+\tau)\hat{a}_4(t+\tau)\rangle}{\langle \hat{a}_3^\dagger(t)\hat{a}_3(t)\rangle\langle \hat{a}_4^\dagger(t+\tau)\hat{a}_4(t+\tau)\rangle}. \tag{1.40}$$

Taking $\tau = 0$, dropping the explicit time-dependence notation, using the commutation relation and the normal ordering (creation operators to the left and annihilation operator to the right), it then follows:

$$g^{(2)}(0) = \frac{\langle \hat{a}_3^\dagger\hat{a}_4^\dagger\hat{a}_4\hat{a}_3\rangle}{\langle \hat{a}_3^\dagger\hat{a}_3\rangle\langle \hat{a}_4^\dagger\hat{a}_4\rangle} \tag{1.41}$$

Let's now calculate the terms of Eq. 1.41. The input state is given by $|\Psi\rangle_{input} = |\psi_1, 0_2\rangle$, which means an arbitrary $|\psi_1\rangle$ in input 1 and vacuum state $|0\rangle$ in input 2.

$$\langle \hat{a}_3^\dagger \hat{a}_3 \rangle = \frac{1}{2} \langle \psi_1, 0_2 | (\hat{a}_1^\dagger - \hat{a}_2^\dagger)(\hat{a}_1 - \hat{a}_2) | \psi_1, 0_2 \rangle \tag{1.42}$$

$$= \frac{1}{2} \langle \psi_1, 0_2 | (\hat{a}_1^\dagger \hat{a}_1 - \hat{a}_1^\dagger \hat{a}_2 - \hat{a}_2^\dagger \hat{a}_1 + \hat{a}_2^\dagger \hat{a}_2) | \psi_1, 0_2 \rangle \tag{1.43}$$

$$= \frac{1}{2} \langle \psi_1, 0_2 | (\hat{a}_1^\dagger \hat{a}_1) | \psi_1, 0_2 \rangle \tag{1.44}$$

$$= \frac{1}{2} \langle \psi_1, 0_2 | \hat{n}_1 | \psi_1, 0_2 \rangle . \tag{1.45}$$

Similarly,

$$\langle \hat{a}_4^\dagger \hat{a}_4 \rangle = \frac{1}{2} \langle \psi_1, 0_2 | (\hat{a}_1^\dagger + \hat{a}_2^\dagger)(\hat{a}_1 + \hat{a}_2) | \psi_1, 0_2 \rangle \tag{1.46}$$

$$= \frac{1}{2} \langle \psi_1, 0_2 | (\hat{a}_1^\dagger \hat{a}_1 + \hat{a}_1^\dagger \hat{a}_2 + \hat{a}_2^\dagger \hat{a}_1 + \hat{a}_2^\dagger \hat{a}_2) | \psi_1, 0_2 \rangle \tag{1.47}$$

$$= \frac{1}{2} \langle \psi_1, 0_2 | (\hat{a}_1^\dagger \hat{a}_1) | \psi_1, 0_2 \rangle \tag{1.48}$$

$$= \frac{1}{2} \langle \psi_1, 0_2 | \hat{n}_1 | \psi_1, 0_2 \rangle . \tag{1.49}$$

Now, we must calculate the numerator of Eq. 1.41:

$$\langle \hat{a}_3^\dagger \hat{a}_4^\dagger \hat{a}_4 \hat{a}_3 \rangle = \frac{1}{4} \langle \psi_1, 0_2 | (\hat{a}_1^\dagger - \hat{a}_2^\dagger)(\hat{a}_1^\dagger + \hat{a}_2^\dagger)(\hat{a}_1 + \hat{a}_2)(\hat{a}_1 - \hat{a}_2) | \psi_1, 0_2 \rangle \tag{1.50}$$

$$= \frac{1}{4} \langle \psi_1, 0_2 | (\hat{a}_1^\dagger \hat{a}_1^\dagger \hat{a}_1 \hat{a}_1) | \psi_1, 0_2 \rangle \tag{1.51}$$

$$= \frac{1}{4} \langle \psi_1, 0_2 | \hat{a}_1^\dagger (\hat{a}_1 \hat{a}_1^\dagger - 1) \hat{a}_1 | \psi_1, 0_2 \rangle \tag{1.52}$$

$$= \frac{1}{4} \langle \psi_1, 0_2 | \hat{a}_1^\dagger \hat{a}_1 \hat{a}_1^\dagger \hat{a}_1 - \hat{a}_1^\dagger \hat{a}_1 | \psi_1, 0_2 \rangle \tag{1.53}$$

$$= \frac{1}{4} \langle \psi_1, 0_2 | \hat{n}_1 \hat{n}_1 - \hat{n}_1 | \psi_1, 0_2 \rangle \tag{1.54}$$

$$= \frac{1}{4} \langle \psi_1, 0_2 | \hat{n}_1 (\hat{n}_1 - 1) | \psi_1, 0_2 \rangle \tag{1.55}$$

Combining the results of Eq. 1.55, Eq. 1.45, and Eq. 1.49:

$$g^{(2)}(0) = \frac{\langle \psi_1, 0_2 | \hat{n}_1 (\hat{n}_1 - 1) | \psi_1, 0_2 \rangle}{(\langle \psi_1, 0_2 | \hat{n}_1 | \psi_1, 0_2 \rangle)^2} \tag{1.56}$$

Considering for input $|\psi_1, 0_2\rangle$ a Fock state such as $|n_1, 0_2\rangle$, it the follows:

$$g^{(2)}(0) = \frac{\langle n_1, 0_2 | \hat{n}_1 (\hat{n}_1 - 1) | n_1, 0_2 \rangle}{(\langle n_1, 0_2 | \hat{n}_1 | n_1, 0_2 \rangle)^2} \tag{1.57}$$

$$\Rightarrow g^{(2)}(0) = \frac{n_1 (n_1 - 1)}{n_1^2} \tag{1.58}$$

$$\Rightarrow g^{(2)}(0) = 1 - \frac{1}{n_1} \tag{1.59}$$

where Eq. 1.58 is exactly Eq. 1.1, ending the derivation.

A value of $g^{(2)}(0) = 0$ is only achieved by using a nonclassical state, like a single-photon state $|1\rangle$. The derivation presented here is a quantum version of the intensity interferometer of Hanbury

Brown–Twiss (HBT) experiment [19–22]. The importance of the second-order correlation function $g^{(2)}(0)$ is that it became a metric to classify light, see Table 1.1. A discussion of the second-order correlation function $g^{(2)}(0)$ in much further details can be found, for example, in References [23–25].

Type of Light	Photon stream	second-order correlation function $g^{(2)}(0)$
Classical (chaotic or thermal)	Bunching	> 1
Coherent (laser)	Random	=1
Nonclassical	Antibunching	< 1

Table 1.1: Classification of light according to second-order correlation function. Adapted from Ref. [6].

1.2.2 Indistinguishability

If two photons are identical in all degrees of freedom, they are called indistinguishable. To test that, we refer to the Hong-Ou-Mandel (HOM) effect [26]. In Fig. 1.3, consider single photons coming in inputs 1 and 2. Once again, the timer registers coincidence counts. For convenience, we will repeat Eq. 1.30 and Eq. 1.31, so we have:

$$\hat{a}_3^\dagger = \frac{1}{\sqrt{2}}(\hat{a}_1^\dagger - \hat{a}_2^\dagger), \tag{1.60}$$

$$\hat{a}_4^\dagger = \frac{1}{\sqrt{2}}(\hat{a}_1^\dagger + \hat{a}_2^\dagger). \tag{1.61}$$

Adding Eq. 1.60 and Eq. 1.61:

$$\hat{a}_3^\dagger + \hat{a}_4^\dagger = \frac{1}{\sqrt{2}}(2\hat{a}_1^\dagger) \tag{1.62}$$

$$\Rightarrow \hat{a}_1^\dagger = \frac{1}{\sqrt{2}}(\hat{a}_3^\dagger + \hat{a}_4^\dagger). \tag{1.63}$$

Subtracting,

$$\hat{a}_3^\dagger - \hat{a}_4^\dagger = \frac{1}{\sqrt{2}}(-2\hat{a}_2^\dagger) \tag{1.64}$$

$$\Rightarrow \hat{a}_2^\dagger = \frac{1}{\sqrt{2}}(-\hat{a}_3^\dagger + \hat{a}_4^\dagger). \tag{1.65}$$

Now, consider input state given by $|1_1, 1_2\rangle$, which means one single photon at input port 1 and one single photon at input port 2.

$$|1_1, 1_2\rangle \tag{1.66}$$

$$= \hat{a}_1^\dagger \hat{a}_2^\dagger |0, 0\rangle \tag{1.67}$$

Then, it implies:

$$\Rightarrow \frac{1}{2}(\hat{a}_3^\dagger + \hat{a}_4^\dagger)(-\hat{a}_3^\dagger + \hat{a}_4^\dagger)\,|0,0\rangle \tag{1.68}$$

$$= \frac{1}{2}(-\hat{a}_3^\dagger\hat{a}_3^\dagger + \hat{a}_3^\dagger\hat{a}_4^\dagger - \hat{a}_4^\dagger\hat{a}_3^\dagger + \hat{a}_4^\dagger\hat{a}_4^\dagger)\,|0,0\rangle \tag{1.69}$$

$$= \frac{1}{2}(-\hat{a}_3^\dagger\hat{a}_3^\dagger + \hat{a}_3^\dagger\hat{a}_4^\dagger - \hat{a}_3^\dagger\hat{a}_4^\dagger + \hat{a}_4^\dagger\hat{a}_4^\dagger)\,|0,0\rangle \tag{1.70}$$

$$= \frac{1}{2}(-\hat{a}_3^\dagger\hat{a}_3^\dagger + \hat{a}_4^\dagger\hat{a}_4^\dagger)\,|0,0\rangle \tag{1.71}$$

$$= \frac{1}{2}(-\hat{a}_3^\dagger\,|1,0\rangle + \hat{a}_4^\dagger\,|0,1\rangle) \tag{1.72}$$

$$= \frac{1}{2}(-\sqrt{2}\;|2,0\rangle + \sqrt{2}\;|0,2\rangle) \tag{1.73}$$

$$= \frac{1}{\sqrt{2}}(-|2,0\rangle + |0,2\rangle)\ \text{(Hong-Ou-Mandel effect)} \tag{1.74}$$

The Hong-Ou-Mandel (HOM) effect, Eq. 1.74, tells us that the two incoming photons coalesce at the output of a beamsplitter. Classically, one expects 4 possible outcome configurations, however due to quantum interference, only 2 outputs actually occur, i.e., the two incoming photons emerge out of the beamsplitter together in either one of the output ports, as depicted in Fig. 1.4. This quantum interference, and therefore the HOM effect, happens for indistinguishable incoming photons, and thus, the strength of the effect can be used as a measure of indistinguishability. Assume that the two input photons are perfectly indistinguishable in all degrees of freedom, except for the time of arrival at the beamsplitter. So, one can fix the time of arrival for one photon, while adjusting the time of arrival for the second photon. Usually, this is done by fixing the path of one photon, while varying the path of the second photon using a mechanical stage.

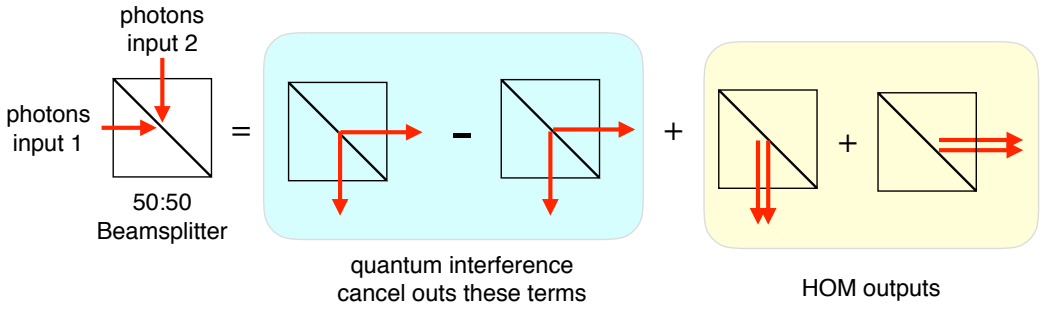

Figure 1.4: The Hong-Ou-Mandel (HOM) effect. Two indistinguishable incoming photons coalesce in a beamsplitter. Classically, there are 4 possible outcome configurations, however due to quantum interference, only 2 outputs actually occur, i.e., the two incoming photons emerge out of the beamsplitter together in either one of the output ports. The light blue box shows the two output configurations cancelled out. The light yellow box shows the only permitted Hong-Ou-Mandel outputs.

Now, what would happen to the coincidence counts? When the photons arrive at difference times (distinguishable), the photons can come out of the beamsplitter according to the 4 classical possibilities, and therefore detections in both D3 and D4 can happen, leading to a coincidence count. However,

when the photons arrive on the beamsplitter at the same time, the HOM effect takes place, and no coincidence count between D3 and D4 is recorded, as both photons are coming out of the same output port. This leads to a dip in the coincidence counts as shown in Fig. 1.5 (a). From there, one can calculate a visibility formula (Eq. 1.75), as depicted in Fig. 1.5 (b):

$$V_{HOM} = \frac{C_{max} - C_{min}}{C_{max}} \tag{1.75}$$

where C_{max} is the maximum value of coincidence counts rate and C_{min} is the minimum value of coincidence counts rate. If the incoming photons are truly indistinguishable, C_{min} will approach zero, in practice, it will tend to reach the detectors noise level. Therefore, a $V_{HOM} = 100\%$ corresponds to 100% indistinguishability between the two incoming photons.

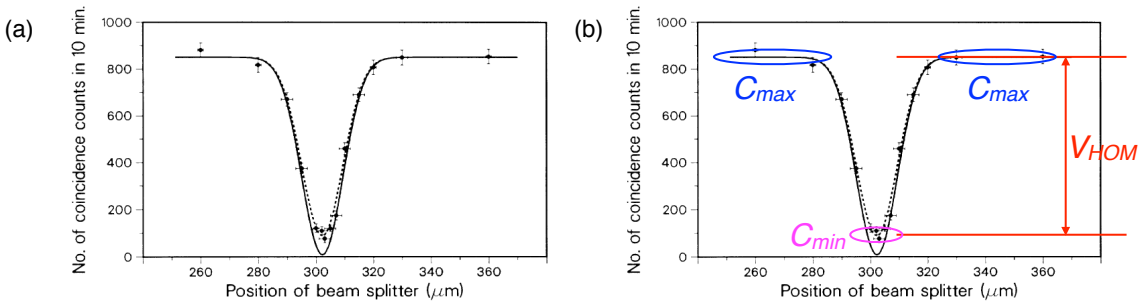

Figure 1.5: The Hong-Ou-Mandel (HOM) Dip. (a) When photons arrive at different times, they are distinguishable, both detectors can click and a coincidence count is register. When photons arrive at the same time, and are indistinguishable in all degrees of freedom, they coalesce accordingly to the HOM effect, and no coincidence counts occurs, causing a dip in the graph. Figure (a) from the original Hong-Ou-Mandel article [26]. (b) Same picture as (a) but with the inclusion of the terms of the visibility formula (Eq. 1.75). C_{max} (blue) is the maximum value of coincidence counts rate and C_{min} (magenta) is the minimum value of coincidence counts rate.

The Hong-Ou-Mandel effect expands over many applications in quantum optics, including optical quantum computing [27], frequency-domain interference [28], and atomic interference using a Bose–Einstein condensate of metastable ^{4}He atoms [29]. Since the HOM effect is a benchmark in quantum optics, it was used in many different contexts, such as in the evaluation of spectrally-narrow single photons designed for quantum memory [30], in the test of the performance of solid-state single-photon sources [31], and showing quantum interference between photons from the Sun and a quantum dot source [32]. A video of the HOM effect can be found in Ref. [33, 34].

Another aspect that makes the HOM effect interesting is that it is an entangling[2] operation. This means that in the input we have separable states, while the output is in an entangled state. Furthermore, the HOM effect changed the field of quantum optics by directly opposing one of Dirac's most known statement: "each photon then interferes only with itself. Interference between two different photons never occurs" [35]. Now we can say conclusively that it does!

[2]Entanglement is introduced in section 1.4.

1.2.3 Brightness

In general terms, "the brightness of the source represents the maximum rate at which single photons can be emitted (or collected)" [36]. More specifically, there are two common definitions used in the quantum optics community. Those usually involved in fabrication of solid-state single-photon sources define brightness as "the number of photons collected per excitation pulse into the first lens" [37], where the first lens here refers to the one outside the solid-state cavity used in the optical setup. Solid-state single-photons sources are discussed in section 1.3.1. However, those interested in the manipulation of the single photons usually tend to refer to the same definition but not "into the first lens", rather at the output of the first single-mode optical fibre. The former definition is also called "source brightness", whilst the latter definition is referred as "absolute brightness" [38]. For practical purposes the latter is more convenient, as it represents the number of photons available for experimentalists.

Other metrics of single-photons sources can be defined, but for our purposes, these 3 properties suffice for now and are broadly applied for different kinds of sources. The requirements on each of these metrics is determined by the particular application being investigated. Consider the two examples from Reference [36]: if an experimentalist would like to implement a protocol of quantum cryptography [39] called BB84 [40], indistinguishability in a train of single photons is not a crucial parameters, provided the photons are uncorrelated, but $g^{(2)}(0) < 0.1$ is required; in another case, for one-way (cluster-state) quantum computing [41, 42], high indistinguishability and low $g^{(2)}(0)$ are essential.

1.2.4 Nomenclature: manifold single photons *vs* multiphotons

For the sake of clarity, we will differentiate two terms: manifold single photons and multiphotons. Using a number-basis representation, we will define:

- **Manifold single photons** or simply single photons as n copies of a single photon. Mathematically, $n|1\rangle$. This means the one has, in principle, the ability to manipulate each of these n single photons individually.

- **Multiphotons** as a wavepacket composed of n photons. Mathematically, $|n\rangle$, for $n > 1$ (if $n = 1$, we have the previous case). This means that, in principle, these n photons are manipulated collectively.

Unless explicit otherwise, we will try to use this nomenclature consistently.

1.3 Single-photon sources

There are several techniques to generate single photons. For this thesis, we will discuss 2 main techniques: **Quantum Dots (QDs)** as solid-state sources, and **Spontaneous Parametric Down Conversion (SPDC)** as a quantum nonlinear source.

1.3.1 Quantum Dots: solid-state single-photon sources

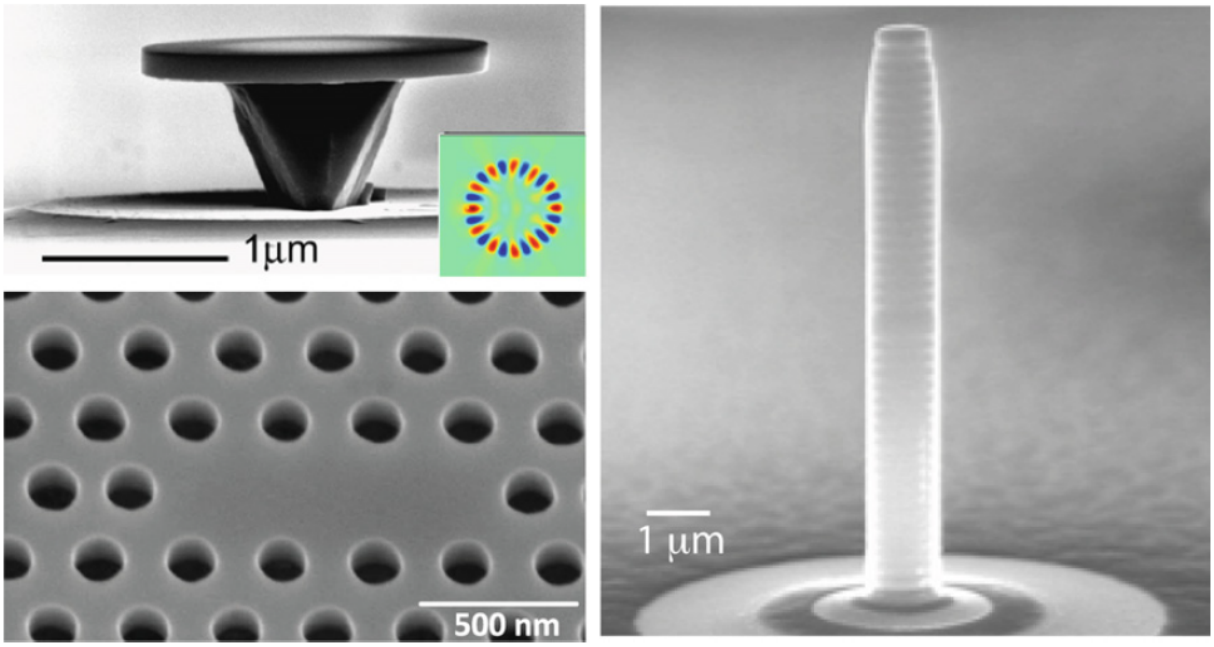

Figure 1.6: Examples of cavity systems for solid-state single-photon sources. Top Left: whispering gallery mode. Bottom Left: photonic crystal. Right: micropillar. Image from Reference [43].

Quantum dots [46] are engineered semiconductor "artificial atoms" that behave like the two-level atom model as in Fig.1.1. Although they are composed of many atoms, in the range of 10^5 atoms [47], the two-level model is a good approximation. Once the QD is excited, it can decay to the lower energy level emitting a single photon. Quantum dots can be formed by an island of semiconductor material embedded in a different semiconductor. Commonly used materials are InAs, GaAs and AlAs. When the semiconductor crystal lattice space is approximately the de Broglie wavelength of electrons in the lattice, the motion of the electron is quantized in that direction, an effect named quantum confinement. When confinement is achieved in the three dimensions, a quantum dot is formed [6, 48].

The next step is to give a preferential emission direction. That is achieved by fabricating the quantum dot inside a cavity, making use of the Purcell effect [49, 50]: spontaneous emission is enhanced in one particular mode and/or suppressed in all other modes. Examples of cavity systems used for such purpose are whispering gallery modes resonators, photonic crystals and micropillars, see Fig. 1.6.

In order to generate single photons, the QD must be properly excited. There are 3 main ways to do so:

> "The excitation energy can be either (1) above band, i.e., above the band gap of the barrier material, (2) quasiresonant, i.e., matching an excited excitonic state or continuum of states in the wetting layer, or (3) resonant, i.e., exactly matching the energy of the exciton transition under investigation." (Reference [47], page 357.)

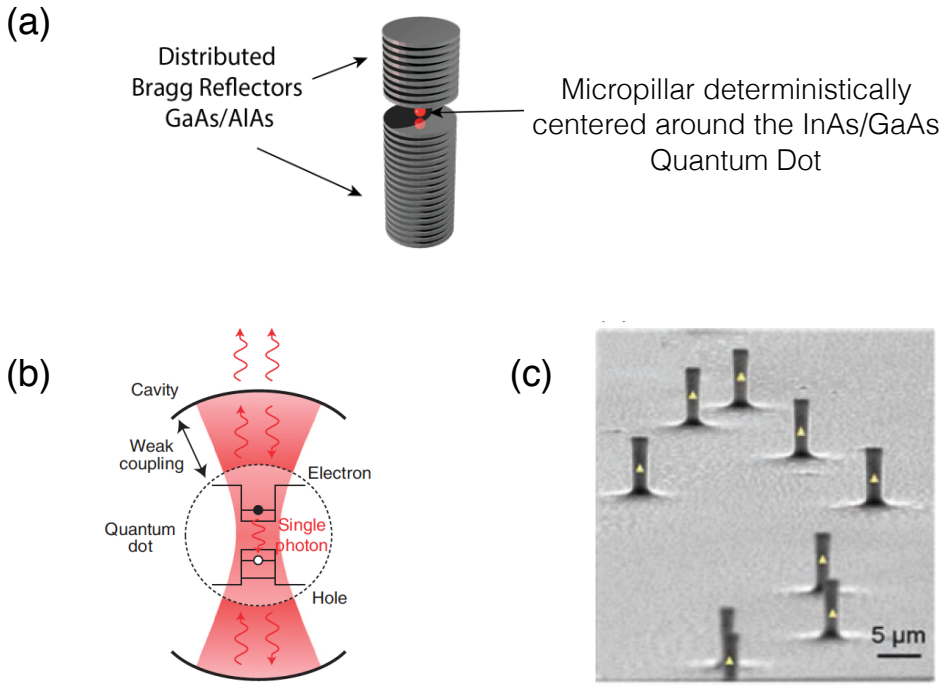

Figure 1.7: Quantum dot QD2013. (a) Conceptual view of the QD and the micropillar cavity. Bragg Reflectors are alternating layers of semiconductor that act as mirrors. The bottom Bragg Reflectors should reflect all the light back to inside the cavity. The top Bragg Reflector should act as partial reflecting mirrors, reflecting a fraction of the light back to the cavity, while allowing some of the light to escape the cavity. The QD is excited from the top, and the generated single photons are also extracted from the top. Credit of the image: QT Lab - UQ. (b) Additional conceptual view of the QD and the micropillar cavity. Credit of the image: [44]. (c) Scanning Electron Microscope (SEM) image of a single wafer with several micropillar QDs. Credit of the image: [45].

The most desired excitation technique is the resonant excitation because it increases the indistinguishability of the emitted photons. However, it is the most difficult to achieve as one must match the resonant conditions of the QD itself (the two-level model), the cavity surrounding the QD, and the pumping laser, this last one also built with a cavity. Despite its technical difficulties, resonant excitation has been demonstrated, for example References [37, 51, 52]. Highly indistinguishable single photons from quantum dots were demonstrated, for instance, in Reference [31].

Let us now address our particular QD system. The quantum dots (QDs) used in the Quantum Technology Laboratory at the University of Queensland employ the micropillar approach and are fabricated by our French partners led by Professor Dr. Pascale Senellart at the University of Paris – Saclay. The QT Lab has operated 2 kinds of these QDs:

- **Quantum dot QD2013**. The quantum dot position is imaged, and subsequently a micropillar is deterministically manufactured centered at the quantum dot location, as indicated in Fig. 1.7. The manufacturing details can be found in Reference [44]. A quantum dot of this kind was used in the demonstration of our Multiple Channel Optical Switcher (MuChOS) photonic chip, which is the topic of Chapter 2.

- **Quantum dot with electrical control QD2016**. The addition of electrical control was a major advance compared to the previous technology. It allows to explore the Stark effect in order to achieve the resonant excitation conditions, causing a great improvement in indistinguishability. The Stark effect corresponds to the shift of the energy levels of a atom (our case an artificial atom, the quantum dot) in the presence of an electric field. More details about this QD can be found in Fig. 1.8 and Reference [37].

Both QDs operate at cryogenic temperature, usually below 20 K, and in a vacuum chamber, below 12 mPa (0.09 mTorr). A comparison of the metrics of QD2013 and QD2016 can be found in Table 1.2. The QD2016 is now a commercial product [53] and it was installed at QT Lab in 2018.

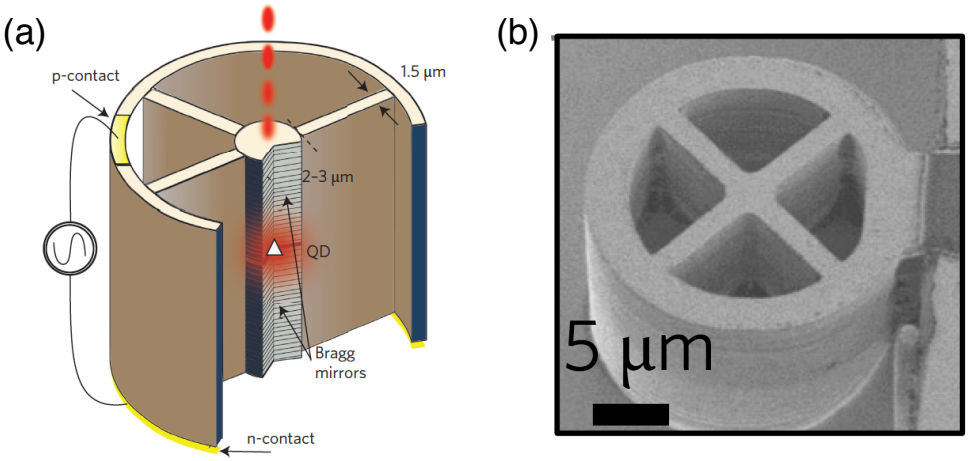

Figure 1.8: Quantum dot with electrical control QD2016. (a) Conceptual view of the QD2016. Credit of image: [37]. (b) Image of a real QD2016. Credit of image: [54].

QD Metrics	QD2013	QD2016
$g^{(2)}(0)$	< 0.15	0.0028 ± 0.0012
Indistinguishability (HOM)	0.82 ± 0.1	0.9956 ± 0.0045
Brightness (collected photon per pulse)	0.79 ± 0.08	0.65 ± 0.07

Table 1.2: Quantum dots metrics. A comparison between QD2013 and QD2016. Data taken by the manufacturer [37, 44].

1.3.2 Quantum nonlinear sources

Using nonlinear optics [55, 56], there are two main techniques to obtain single photons: **Spontaneous Parametric Down Conversion (SPDC)**[3] and **Spontaneous Four Wave mixing (SFWM)**, SPDC being the most commonly used to date. Here we will discuss SPDC due to the fact it was used in our quantum correlation experiment (Chapter 5). The reader may find more details about SPDC in Ref. [58, 59], and about SFWM, for example, in Ref. [60–62]. SPDC explores a $\chi^{(2)}$ optical nonlinearity, while SFWM uses $\chi^{(3)}$.

[3] A SPDC source was even capable of working after a rocket explosion [57].

In SPDC, the pump laser reaches a nonlinear crystal [63], and once the phase-matching condition and energy conservation are fulfilled, a pair of single photons can be probabilistically produced. The pump laser can be either pulsed or continuous wave. Spontaneous Parametric Down Conversion (SPDC) is an intrinsic probabilistic single-photon generation process, therefore it demands a heralding detection to confirm a photon pair production. One of the single photons from the pair is detected in one mode, and it heralds the presence of the other single photon of the pair in the other mode. Thus, they are commonly named signal and idler or signal and trigger, see Fig. 1.9.

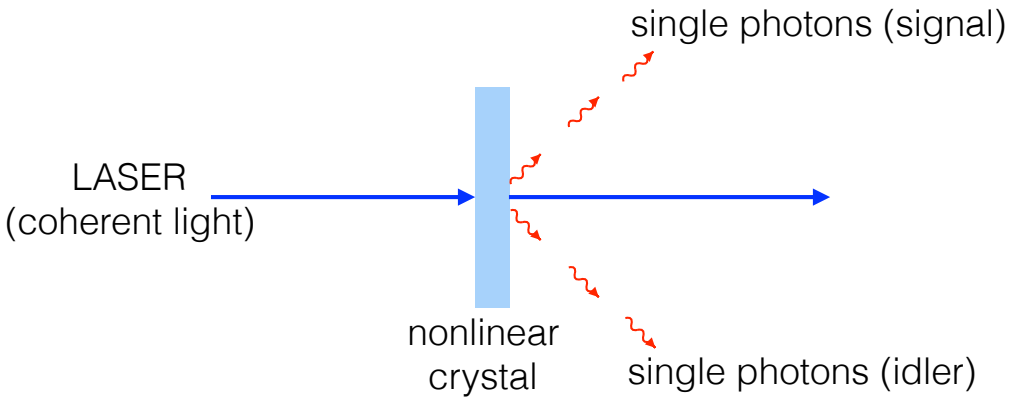

Figure 1.9: Spontaneous Parametric Down Conversion (SPDC) - signal and idler. As the laser pump passes through a nonlinear crystal, a single-photon pair can be probabilistically produced. One photon heralds the presence of the other one, and thus, they are named signal and idler, or signal and trigger.

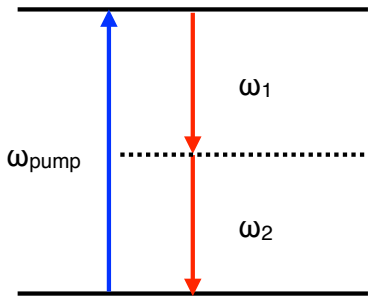

Figure 1.10: Spontaneous Parametric Down Conversion (SPDC) - Diagram Levels. A photon with angular frequency ω_{pump} is absorbed from the pump laser. This corresponding energy is then released by the emission of two single photons (ω_1 and ω_2). If ω_1=ω_2, the process is called degenerated.

This process can only occur when certain conditions are obeyed: momentum conservation (phase-matching) and energy conservation. The phase-matching must obey Equation 1.76, where $\vec{k}$ represents the wave vector[4]:

$$\vec{k}_{pump} = \vec{k}_{signal} + \vec{k}_{idler}. \tag{1.76}$$

[4]Equation 1.76 is a simplified model. A more realistic model should also include the momentum of the crystal.

The energy conservation condition leads to:

$$E_{pump} = E_{signal} + E_{idler} \tag{1.77}$$

$$\hbar\omega_{pump} = \hbar\omega_{signal} + \hbar\omega_{idler} \tag{1.78}$$

$$\omega_{pump} = \omega_{signal} + \omega_{idler}, \tag{1.79}$$

where $\hbar$ is the Planck's reduced constant, $\hbar = \frac{h}{2\pi}$. If $\omega_{signal} = \omega_{idler}$, it is called *degenerated*. Otherwise, if $\omega_{signal} \neq \omega_{idler}$, it is called *non-degenerated*. For a diagram level of SPDC, see Fig. 1.10.

The SPDC single-photon generation process can be of 3 kinds [58]:

1. Type 0: Pump laser, trigger and signal fields all have the same polarization;
2. Type I: Trigger and signal have the same polarization and it is orthogonal to the pump laser polarization;
3. Type II: Trigger and signal have orthogonal polarization to each other.

In number basis, the quantum state obtained in SPDC is given by Equation 5.71:

$$|\psi\rangle_{SPDC} = \sqrt{1-\chi^2} \sum_{n=0}^{\infty} \chi^n |n_1 n_2\rangle = c_0 |00\rangle + c_1 |11\rangle + c_2 |22\rangle + c_3 |33\rangle + \cdots, \tag{1.80}$$

where n_i is the photon number on the i^{th} mode, $0 \leq \chi < 1$ is a parameter representing the strength of the SPDC, and c_n is the coefficient for each ket state. For quantum information processing, the critical term is the $|11\rangle$, when one obtains exactly one single photon as idler and one single photon as signal. The higher order terms ($|n_1 n_2\rangle$ for $n > 1$) will be discussed in more detail in Chapter 5.

Some SPDC sources employ bulk crystals such as BBO and BiBO [63]. Others use a technique called periodic poling, in which the crystal domains are engineered to increase the optical nonlinearity and facilitate the phase-matching, leading the brighter sources [58].

Another parameter in the design of SPDC single photon source is the focusing of the pump on the crystal, since it affects the collection of the single photons and the coupling to optical fibers [64].

1.4 Entangled states

Entanglement is a key concept in quantum mechanics. To say two photons (or qubits[5]) are entangled means that these two photons (or qubits) cannot be mathematically described as the product of separable states. In other words, the joint properties of a pair of entangled quantum systems are not completely described by the properties of the individual systems, an effect with no classical analogue. Consider the simplest case, pure bipartite states [66]: $|\Psi_{AB}\rangle \in \mathscr{H}_{AB} = \mathscr{H}_A \otimes \mathscr{H}_B$, where $\mathscr{H}$ is the corresponding Hilbert space. If $|\Psi_{AB}\rangle$ can be decomposed as the product of two vectors subsystems, then $|\Psi_{AB}\rangle$ is called a product state and there is no entanglement, $|\Psi_{AB}\rangle = |\phi_a\rangle\,|\psi_B\rangle$. On the other

[5]Classical information theory uses the bit, a binary unit of information typically encoded as 0 or 1; in the quantum version, the quantum bit (**qubit**) is a coherent superposition of two quantum states, as opposed to an incoherent mixture of those two states [65].

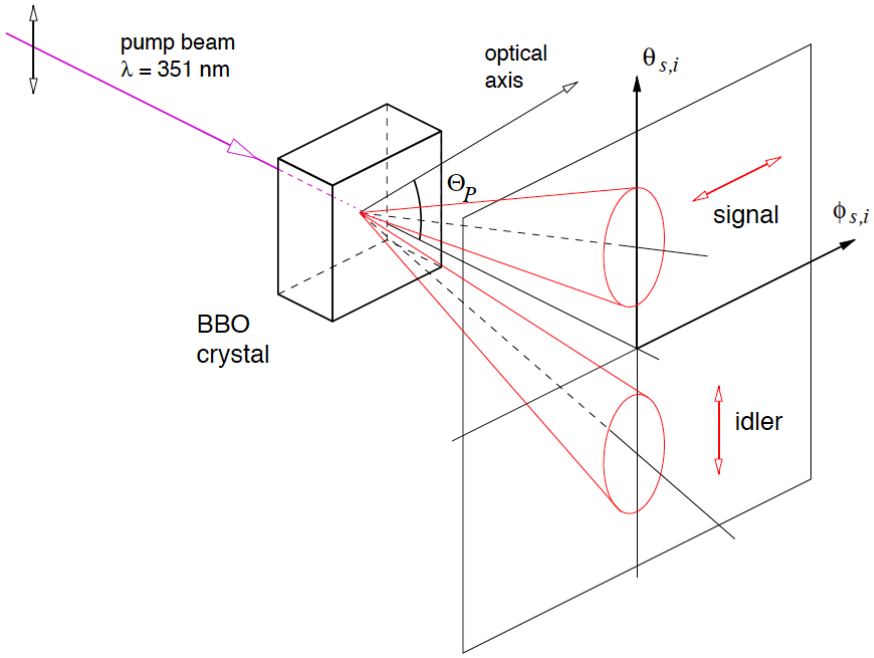

Figure 1.11: Example of a Spontaneous Parametric Down Conversion (SPDC) - type II single-photon source. A laser pump with $\lambda = 351$ nm reaches a BBO crystal. The signal and idler single photons emerge out of the crystal with the cone structure as shown in the picture. Note that pump and idler have the same polarization, while signal has a polarization orthogonal to them. Credit of image: [59].

hand, $|\Psi_{AB}\rangle$ is entangled if it cannot be written as a separable state, i.e., a convex combination of product states. In our example, if $|\Psi_{AB}\rangle$ is an entangled state, then $|\Psi_{AB}\rangle \neq |\phi_a\rangle\,|\psi_B\rangle$.

Entanglement is related to the famous Einstein-Podolsky-Rosen Paradox from 1935 [67] arguing the incompleteness of Quantum Mechanics. In response to that, Niels Bohr introduced the concept of complementarity [68]. The term *entanglement* does not appear on the original Einstein, Podolsky and Rosen paper. It was latter coined by Erwin Schrödinger [69]. Entanglement is one kind of quantum correlation, but there are a few others. This is the topic of Chapter 5.

Any degree of freedom of two quantum systems can be used to produce an entangled state. For example, both quantum dots and SPDC can produce polarization-entangled photons, as in References [10, 59, 70–73]. In SPDC, one way to generate polarization-entangled photons is to overlap the two down-converted cones, see Fig. 1.12. This is obtained by rotating/tilting the crystal, equivalently to change the phase-matching. Moreover, the SPDC technique was also applied to demonstrate entanglement of the orbital angular momentum states of photons [74]. In QDs, for instance, if there are two paths from the excited state to ground on the QD energy levels, then two entangled photons can be emitted, see Fig. 1.13.

Additionally, two single photons can also be entangled in more than one degree of freedom, leading to the so-called hyperentanglement [75, 76]. For instance, Barreiro *et al* [75] report entanglement between two photons in the polarization, time energy, and spatial mode degrees of freedom using a SPDC source. Prilmuller *et al* [77] describe hyperentanglement of single photons from a quantum dot

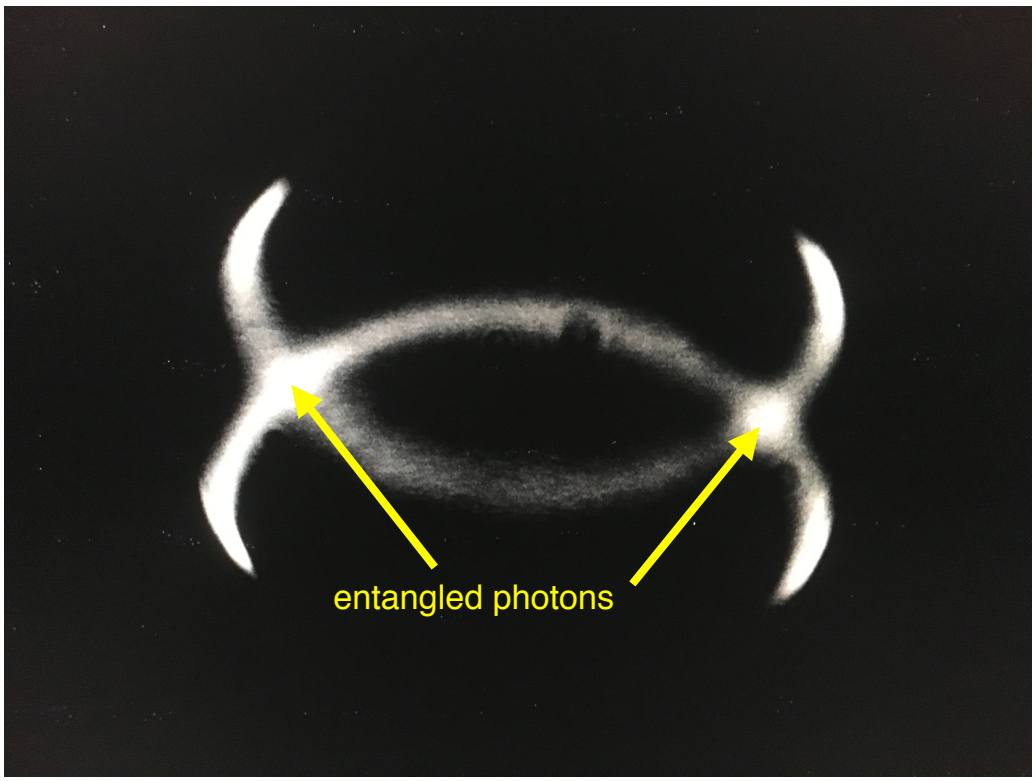

Figure 1.12: Image of the SPDC cones - type II. Photo taken by Raphael A. Abrahao and Ming Su at the QT Lab - UQ. The overlap of the two down-converted cones with orthogonal polarizations results in entangled photons from the intersection points.

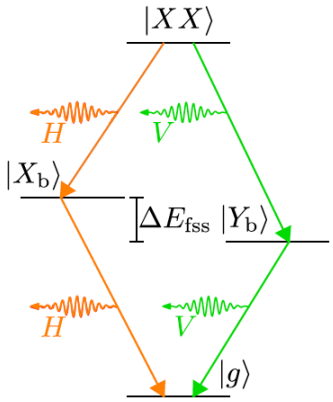

Figure 1.13: Entangled photons from a quantum dot. Biexciton configuration. From the top $|XX\rangle$ QD energy level to the ground $|g\rangle$, there are two paths for decaying. ΔE_{fss} is the energy corresponding to the fine-structure splitting. The ΔE_{fss} should be much smaller than the natural linewidth in order to erase the "which-path information" and then to obtain entangled photons. Credit of image: [47].

source in the degrees of freedom of polarization and time-bin.

Parts of the following publication have been incorporated as Chapter 2.

[1] Francesco Lenzini, Ben Haylock, Juan C. Loredo, **Raphael A. Abrahão**, Nor A. Zakaria, Sachin Kasture, Isabelle Sagnes, Aristide Lemaitre, Hoang-Phuong Phan, Dzung Viet Dao, Pascale Senellart, Marcelo P. Almeida, Andrew G. White, and Mirko Lobino, Active demultiplexing of single photons from a solid-state source, *Laser Photonics Reviews* 11, No. 3, 1600297, 2017.

Contribution to the article [1]:

The Quantum dot used in this experiment was fabricated by P. Senellart, I. Sagnes, and A. Lemaitre. The demultiplexer chip (MuChOS) was fabricated by F. Lenzini, B. Haylock, S. Kasture, H.-P. Phan, and D. V. Dao with the supervision of M. Lobino. The Quantum dot properties were studied by J. C. Loredo and N. A. Zakaria with the supervision of M. P. Almeida and A. White. The tests of the demultiplexer chip (MuChOS) were performed by R. A. Abrahão, J. C. Loredo, and N. A. Zakaria with the supervision of M. P. Almeida and A. White. The manuscript was written by F. Lenzini, B. Haylock with contributions from J. C. Loredo, R. A. Abrahão, N. A. Zakaria, M. P. Almeida, A. White, and M. Lobino.

R. A. Abrahão contributed to design and construction of the experiment and to data acquisition. R. A. Abrahão also contributed to data analysis and interpretation, first draft of manuscript, referee replies and manuscript revision.

Chapter 2

Multiple Channel Optical Switcher (MuChOS): The Photonics Railway on Chip

This Chapter is based on the article **Active demultiplexing of single photons from a solid-state source** published at *Laser & Photonics Reviews* on April 11 2017, which I am an author [1]. Parts of this above-mentioned publication are incorporated here.

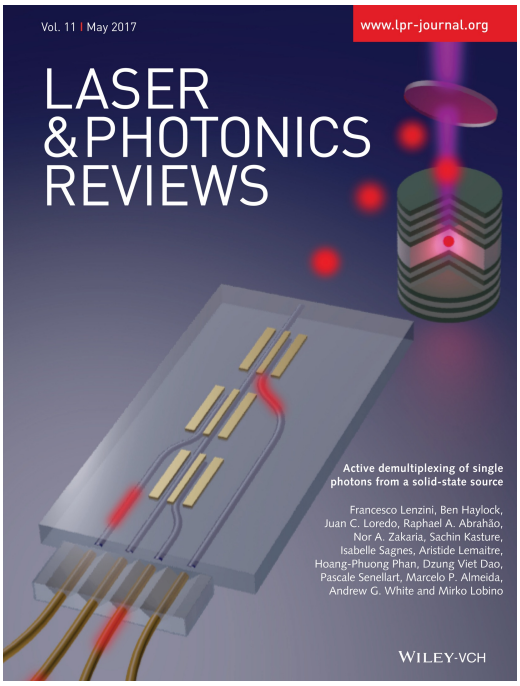

Figure 2.1: Electronic cover of *Laser & Photonics Reviews* featuring the article *Active demultiplexing of single photons from a solid-state source*.

2.1 The need for manifold single photons

The general structure of photonics experiments is given in Fig 2.2. We start with a single-photon source, followed by a preparation stage of the desired photon state in case the source was not capable of delivering so, then a manipulation stage of the photons accordingly to the the particular experiment, and finally photons detection. The manipulation consists of some kind of optical circuit which explores one or more of the photon properties and can use linear and nonlinear optical elements.

Figure 2.2: General structure of photonics experiments. We start with a single-photon source like SPDC or quantum dots. If we do not obtain the desired state from the source, we then enter a preparation stage of the desired state. For instance, if one obtains horizontally polarized photons from the source and one wishes a superposition of horizontal (H) and vertical (V) polarizations photons, let the photon pass though a 22.5° Half-Wave Plate (HWP) followed by a Polarization Beamsplitter (PBS). This will make a qubit as well. Next, the manipulation stage encapsulates the particular application, for example, a quantum controlled-not gate, or a quantum simulation experiment. Finally, we must detect the photons.

Consider the case of a single-photon source that produces photons on a temporal stream. In order to implement more sophisticated quantum optical experiments, we need to take the temporal stream of n single photons from the source and convert them to a source of n single photons in orthogonal spatial modes. This can be called a n-manifold photon source. As a motivation, consider the case of photonic quantum simulation [78]. The quantum simulation of the smallest molecular system, the hydrogen molecule in a minimal basis, was reported in 2010 using 2 photons (2 qubits) [79]. However, the problem for a water molecule (H_2O) would required near 50 photons (qubits) [78]. The number of qubits increases much more when considering even more complicated molecules. Another example is the preparation of a large number of manifold single photons to perform Boson Sampling experiments. Boson Sampling was conceived as a particular mathematical problem where a quantum device could outperform the best classical computers, reaching the so-called quantum computational advantage. Boson Sampling is the topic of Chapter 3.

In this Chapter we will discuss how to achieve the goal of obtaining manifold single photons using a quantum dot source and active demultiplexing. The quantum dot used for this purpose was the QD2013 introduced in Chapter 1. The discussion of the same problem with SPDC or SFWM is not the scope of this chapter, however this can be found in References [80–82].

2.2 Demultiplexing Photons from a Quantum Dot

Quantum dots [46] produce singe photons in the same spatial mode, but different temporal modes. Transferring these photons to the same temporal mode but different spatial modes is called demulti-

plexing. See Fig. 2.3.

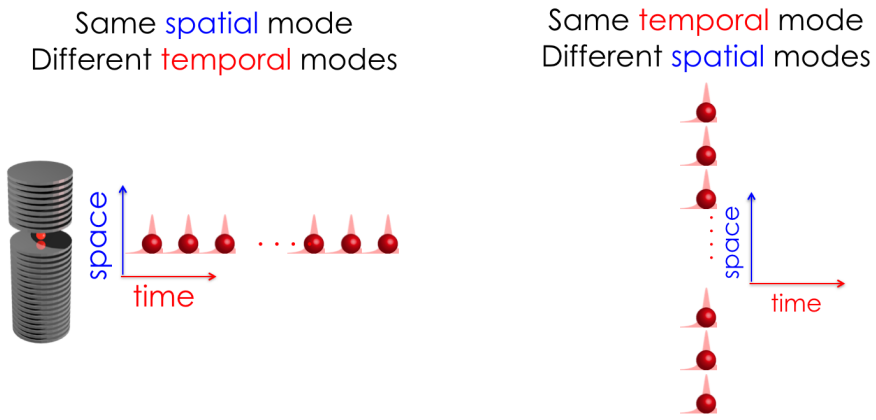

Figure 2.3: Demultiplexing photons from a quantum dot. The photons are emitted in the same spatial mode, but different temporal modes. To produce manifold single photons, one must demultiplex these photons: transfer them to the same temporal mode, but different spatial modes. In order to demultiplex n single photons from a quantum dot source, firstly one must wait a stream of n single photons, which are produced at a given rate, say C_i of counts per second. Then, if the demultiplex is done perfectly, the rate of counts for the demultiplexed single photons is $C_f = \frac{1}{n} \times C_i$. To confirm the success of the demultiplexing operation, one must then detect n single photons coincidence counts. Credit of Image: Andrew G. White.

Demultiplexing can be achieved passively or actively. The former relies on the use of passive optical elements, i.e., not dynamically tunable, with fixed properties. The latter relies on the use of dynamical elements that can be adjusted on demand. One way to implement active demultiplexing is to employ Pockels cells (PC) or other kind of Electro-Optic Modulators (EOM). Alternatively, one can use integrated photonics. See Fig. 2.4.

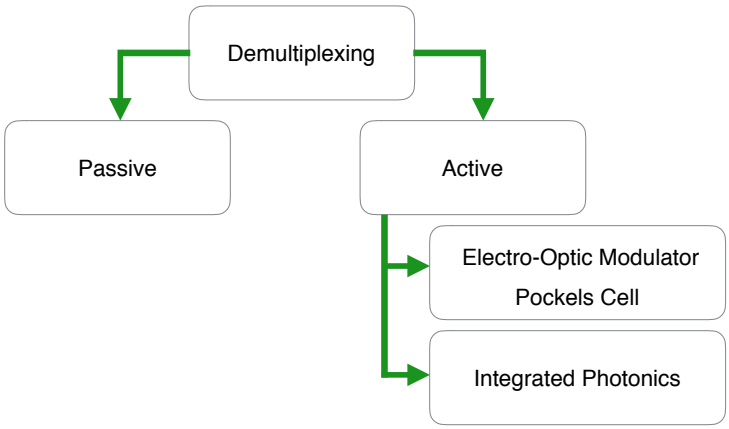

Figure 2.4: Demultiplexing: Passive *vs* Active.

2.3 Passive Demultiplexing

Passive demultiplexing uses a cascade of beamsplitters (BS) with different reflectivity. Let's work out one example. Say one wishes to demultiplex 3 single photons from a QD. The first beamsplitter has $\frac{1}{3}$ reflectivity, and the second beamsplitter has $\frac{1}{2}$ reflectivity. This is represented in Fig. 2.5 (a). The probability of detecting photon 1 at the output is $P_1 = \frac{1}{3}$. The probability of detecting photon 2 at the output is $P_2 = (1-\frac{1}{3})(\frac{1}{2}) = \frac{1}{3}$. The probability of detecting photon 3 at the output is $P_3 = (1-\frac{1}{3})(1-\frac{1}{2}) = \frac{1}{3}$. Therefore, the probability of detecting the 3 demultiplexed single photons is $P_{demux} = P_1P_2P_3 = (\frac{1}{3})^3 = \frac{1}{27}$. The general case for an arbitrary n single photons is depicted in Fig. 2.5 (b). The reflectivities of the cascaded beamsplitters are $\frac{1}{n}$, $\frac{1}{n-1}$, $\frac{1}{n-2}$... until the last beamsplitter with reflectivity $\frac{1}{2}$. The count rates after demultiplexing will be multiplied by a factor of $(\frac{1}{n})^n$, posing a great difficulty to scale experiments for a large number of single photons.

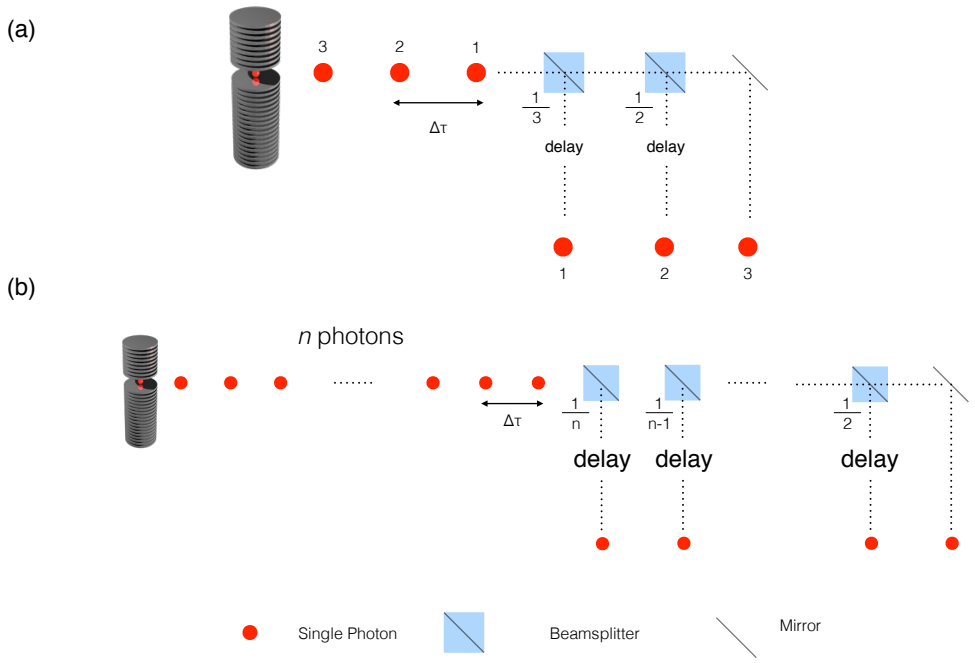

Figure 2.5: Passive Demultiplexing. (a) Example to demultiplex 3 single photons. (b) Generalization to n single photons. The number near each beamsplitter is its reflectivity. The scaling factor is proportional to $\frac{1}{n^n}$.

2.4 Active Demultiplexing using Pockels cell or Electro-Optic Modulator (EOM)

In active demultiplexing, one explores dynamical elements to select a spatial mode for a particular single photon. One such element is the Pockels Cell [18], which can be understood as a Half-Wave Plate (HWP) where one can rotate its optical axis by applying a certain voltage. Therefore, it acts as a "tunable HWP". A Pockels cell explores the Pockels effect, a linear eletro-optical effect. In this effect,

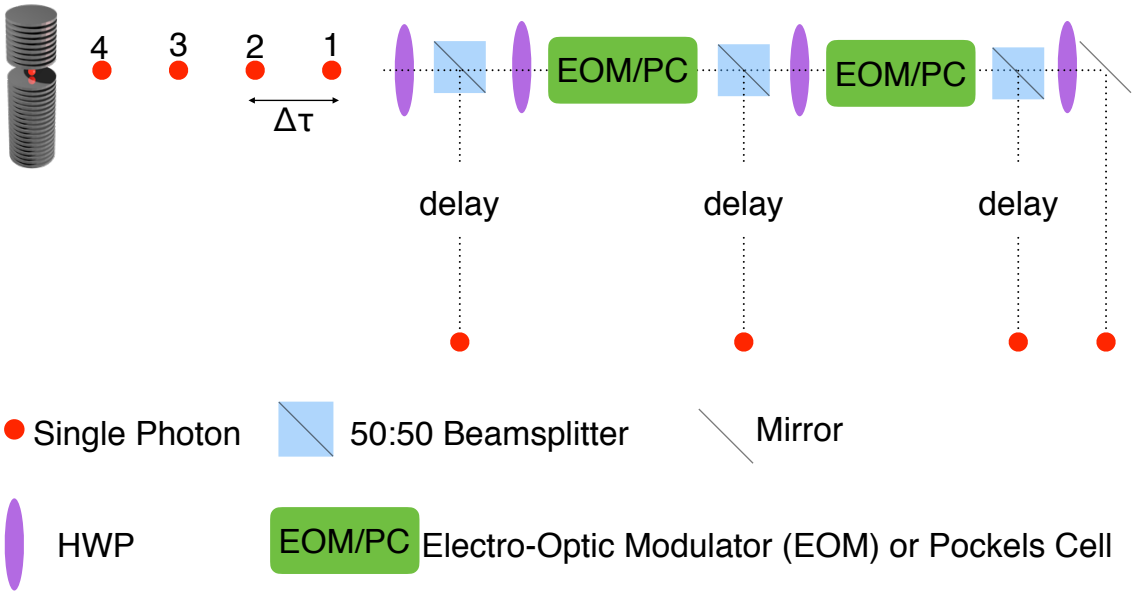

Figure 2.6: Active demultiplexing using an Electro-Optic Modulator (EOM) or Pockels cells (PC). The ideal case of no photon losses leads to 100% efficiency in demultiplexing. Thus, the final count rate will be multiplied by a factor $\frac{1}{n}$, which corresponds to the waiting for n input single photons. In practice, photon losses decrease the final counts. Also, in this scheme, one is limited by the switching rate of the EOMs or PCs, and additional work must be employed to synchronize them.

a DC electric field changes the optical properties of the material, in particular, its refractive index. Then, by controlling the applied DC electric field, one controls the refractive index, and consequently, the speed of the propagation of the electromagnetic wave, and thus the optical phase. It follows then, one is effectively controlling the retardation of the wave propagation, up to the point is can be work as a Half-Wave Plate (HWP) [16]. Pockels cells are one example of a more general class of Electro-Optic Modulators (EOM). Pockels cells or other kinds of EOM are widely available commercial products. One of their most important aspects is how fast either a Pockels cell or a EOM can switch, and this is one of the bottlenecks of most operations.

In Fig. 2.6, we show how Pockels cells or EOMs can be used in a demultiplexing optical circuit. The scaling factor is proportional to $\frac{1}{n}$, a tremendous advantage compared to the $\frac{1}{n^n}$ scaling factor of passive demultiplexing. Fig. 2.7 shows a real use of 6 Pockels cells to demultiplex single photons from a quantum dot source [83]. This was part of a Boson Sampling experiment with 7 input single photons.

2.5 Active Demultiplexing with Integrated Photonics

Here we will present a photonic chip capable of demultiplexing single photons from a quantum dot source. The particular source used was the QD2013 introduced on Chapter 1 and manufactured by our French partners [44]. Our chip was named **Mutiple Channel Optical Switcher (MuChOS)**[1]. It

[1] In Spanish, *muchos* means many.

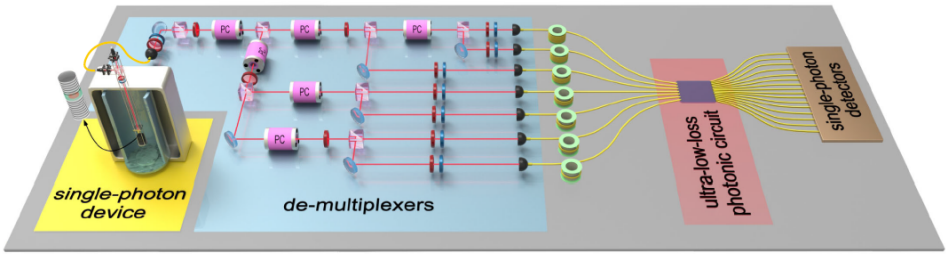

Figure 2.7: Example of demultiplexing using Pockels cells (PC). Six Pockels cells are used to demultiplex single photons from a quantum dot source into 7 spatial modes. This setup was used on a Boson Sampling experiment. Credit of Image: [83].

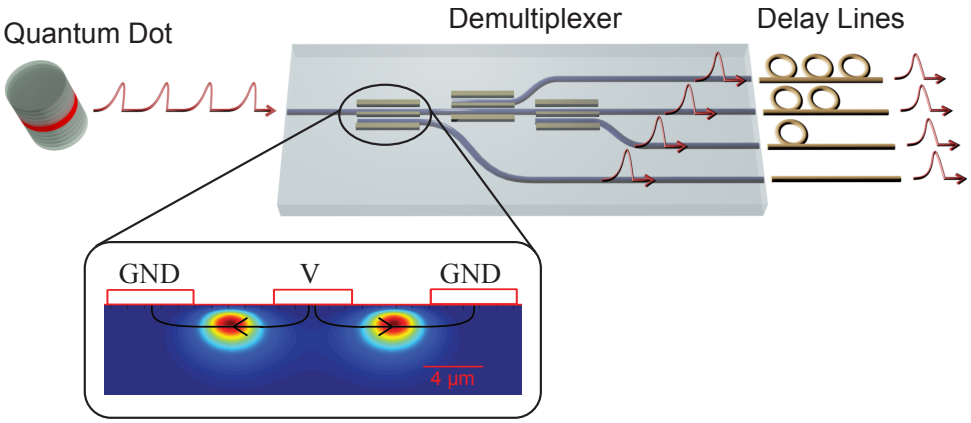

Figure 2.8: Scheme for an ideal active spatial-temporal demultiplexing. A stream of single photons emitted at successive time intervals from a quantum dot coupled to a micropillar cavity are actively routed into different spatial channels by an optical demultiplexer. A set of delay lines at the output can be used to match the arrival times of the single photons. The optical demultiplexer consists of a network of reconfigurable directional couplers with electro-optically tunable splitting ratio. The inset shows the configuration of the electrodes in each directional coupler. The colormap (a.u.) represents the waveguides intensity mode profiles at 932 nm and the black arrows show the direction of the applied electric field.

demultiplexed 4 single photons on a 5 cm integrated chip.

In this work, we implement two important advances towards the realisation of a scalable multifold single-photon source. We first demonstrate the active temporal-to-spatial demultiplexing of a stream of photons to create multi-photon sources with small resource overhead. Secondly, we introduce an integrated zero-buffer active spatial and temporal photonic demultiplexing device, suitable for use with high brightness solid-state sources operating at 932 nm.

Figure 2.8 schematically depicts our proposed demultiplexing protocol. A temporal stream of single photons emitted from a quantum dot-micropillar system is actively routed into different spatial channels by an optical demultiplexer. The demultiplexer is an integrated waveguide device with one input and four output channels made of a network of electro-optically reconfigurable directional couplers fabricated on an X-cut lithium niobate substrate by the annealed proton exchange technique [84].

Electrodes are patterned on top of the waveguides as shown in the inset of Fig. 2.8, and can be used to tune the splitting ratio in the full 0 – 100% range by changing the phase mismatch $\Delta\beta$ between interacting modes [85]. Monolithic integration of the directional coupler network on a single chip is necessary for reduced insertion losses, and with our technology it allows for up to 10 output channels in a 5 cm long device. The material properties of lithium niobate are discussed in detail in References [86, 87].

In a nutshell, the operation of the directional coupler can be explaining as follows: an electrical signal changes the refractive index of the material locally and temporally in such a way that the coupling between two neighboring waveguides is affected. In the ideal case, light can then totally vanishes in one waveguide, as it is fully transmitted to the other waveguide.

2.5.1 Scaling of single-photon demultiplexing using MuChOS

The n-photon count rate $c_{DM}(n)$ measured at the output of an n-channel demultiplexer can be expressed as

$$c_{DM}(n) = R[\eta_{SD}\eta_{det}]^n S_{DM}(n), \tag{2.1}$$

where $\eta_{SD} = \eta_{QD}T$ is the product of the source brightness η_{QD}, defined as the probability of emitting one photon at the input of the demultiplexer for each excitation pulse, times the total transmission of the device T. R is the pump laser repetition rate of the source and η_{det} is the detectors efficiency. $S_{DM}(n)$ is a parameter which accounts for how the efficiency of the demultiplexing scheme scales with increasing number of photons and it represents the limit of what can be achieved by the demultiplexer with a lossless and deterministic source. Note that the term $[\eta_{SD}\eta_{det}]^n$ is intrinsically probabilistic, and will unavoidably result in an exponential decay with photon number. In a probabilistic scheme [88]–made of a network of passive beamsplitters–the demultiplexing parameter scales as $S_{DM}(n) = (\frac{1}{n})^n$, super-exponentially decreasing with n, a non-scalable approach. In contrast, in an active demultiplexing scheme the scaling is

$$S_{DM}(n) = \frac{1}{n}\Big[\eta_{DM}^n + (n-1)\Big(\frac{1-\eta_{DM}}{n-1}\Big)^n\Big], \tag{2.2}$$

where η_{DM} is the "switching efficiency", defined as the average probability of routing a single photon in the desired channel in each time bin. In the limit of deterministic demultiplexing, i.e. $\eta_{DM} \to 1$, the scaling becomes polynomial in n, and thus constituting a scalable approach.

2.5.2 Fabrication of MuChOS

The fabrication of the MuChOS chip was done by our partners at Griffith University led by Prof. Mirko Lobino. The waveguides were fabricated with a 6 μm channel width and a proton exchange depth of 0.47 μm followed by annealing in air at 328°C for 15 h. These parameters are chosen in order to ensure good overlap with single-mode fiber and single-mode operation at $\sim$ 930 nm, the emission wavelength of our InGaAs QD. Each directional coupler has a distance between waveguide centres of 8.8 μm and a 4.5 mm length (equal to three coupling lengths), resulting in complete transmission of

light into the coupled waveguide when no voltage to the corresponding switching electrodes is applied. Difference from this ideal behaviour is due to non-uniform waveguide channel widths, caused by the resolution of the photolithography.

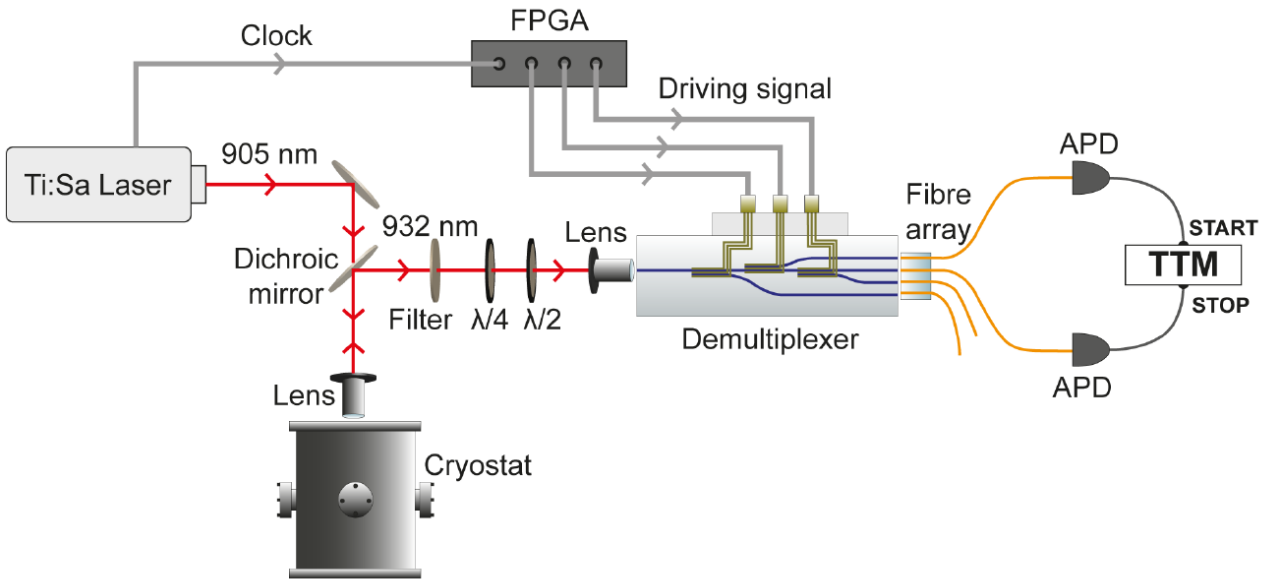

Figure 2.9: Conceptual setup for MuChOS characterization. A 905 nm pulsed Ti:Sapphire laser pumps the quantum dot (QD2013) [44] producing single photon with 932 nm wavelength. The same laser is used to synchronize the field programmable gate array (FPGA). An optical system was build to collect the produced single photons and guide them to the Multiple Channel Optical Switcher (MuChOS), labelled as Demultiplexer in the picture. The MuChOS chips is also connect to the FPGA which provides the electronic signal for each directional coupler. After the chip, light is coupled into fiber optics, and then detected using avalanche photodiodes (APD) single-photon detectors, which are connected to a time-tagging module for the purpose of recording coincidence counts.

(a)

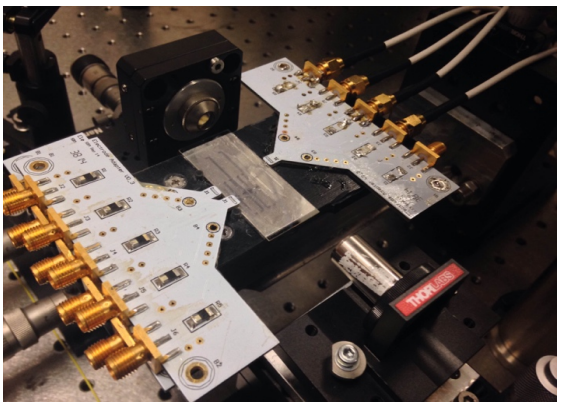

(b)

Figure 2.10: (a) Image of a one of the MuChOS chips tested for this experiment. (b) The output of one of the MuChOS chip is imaged using laser light and an infrared card. The particular chip used in this picture had 5 channels, as one can see 5 spots. All the data in the article and in this chapter was taken using a single MuChOS chip, which we tested and presented the best performance of all.

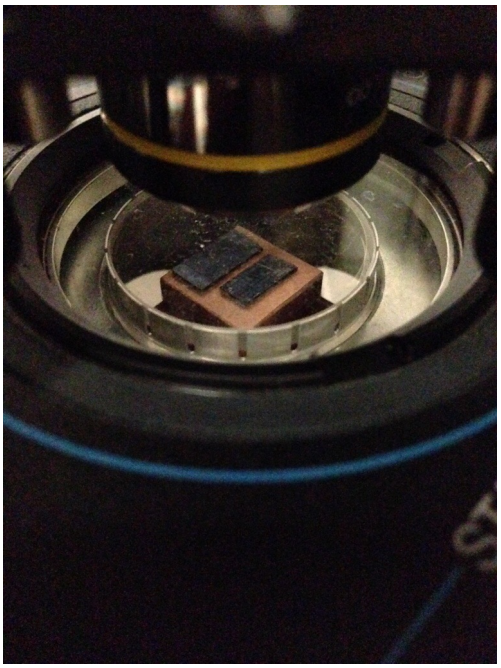

Figure 2.11: Quantum dot chamber. The principles of operation of our QD system (QD2013) was explained in Chapter 1. This is the same kind of QD as in Reference [44]. The two visible chips in the picture contain a few quantum dots. After their single-photon emission properties were studied, one of the quantum dots was selected for this experiment.

2.5.3 Performance of MuChOS

The tests of the MuChOS chip were executed in the QT Lab at the University of Queensland. The experimental setup is schematically shown in Fig. 2.9: the QD is quasi-resonantly pumped via p-shell excitation with a 905 nm, 80 MHz, 5 ps pulsed Ti:Sapphire laser. The single photons have a 932 nm emission wavelength and are separated from the pump beam via a dichroic mirror and a 0.85 nm FWHM bandpass filter. Quarter- and half-wave plates are used at the input for polarisation alignment as the waveguides within the demultiplexer guide one (horizontal) polarisation. In our case, this reduces the available photon flux at the input of the demultiplexer by $\sim 50\%$ since the source is only weakly polarised [44], an issue absent if operated with sources engineered to exhibit a large degree of polarization. Photons are injected at the input of the device with a lens of NA = 0.55 and all four outputs are collected with a fibre V-Groove array. For a photo of the quantum dot chamber see Fig. 2.11, and for a photo of one of the fabricated MuChOS chips, refer to Fig. 2.10 (a). The output of the MuChOS chip was imaged using laser light and a infrared-viewer card, as depicted in Fig. 2.10 (b).

Photon-coincidences between the output channels are measured using avalanche photodiodes with approximately 30% average quantum efficiency, and a time-tagging module (TTM). The electrodes of the demultiplexer are driven with a custom-made pulse generator based on a field programmable gate array (FPGA) [89]. The FPGA produces a preset sequence of pulses with varying voltages that are used to tune the splitting ratio of the directional couplers between on and off values. The driving pulses are synchronized with the clock signal of the Ti:Sapphire laser using internal phase-locked loops (PLL) of the FPGA which provide an adjustable time delay with a low time jitter (300 ps) [89].

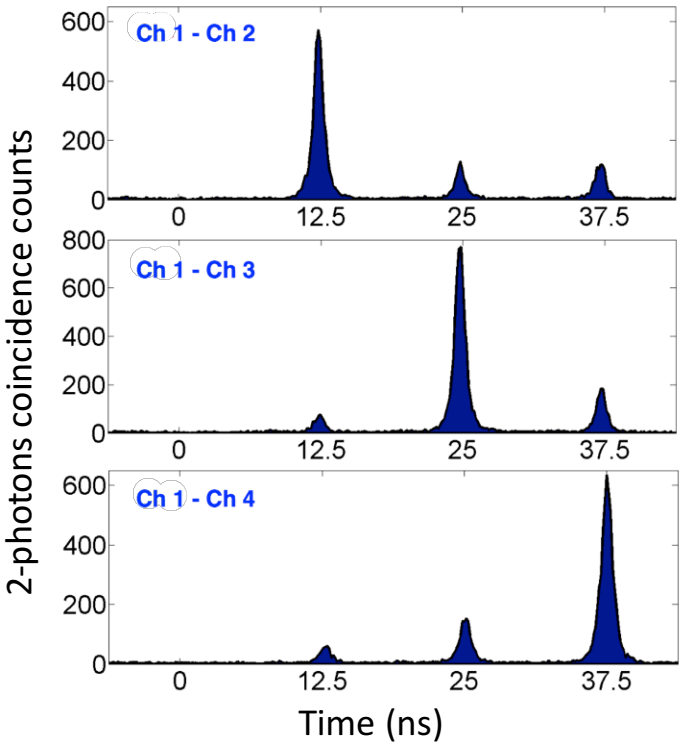

Figure 2.12: Two-photon coincidence counts after demultiplexing with the MuChOS chip. In the top, it is shown the two-photon coincidence counts from the outputs Channel 1 and 2. Likewise, the middle picture for channels 1 and 3, and the bottom picture for channels 1 and 4. The shift of the main peak by 12.5 ns corresponds to the 80 MHz frequency of the pulsed pump laser. The smaller peaks are due to imperfections in the fabrication of the device.

The demultiplexer can be actively driven into any configuration by changing the programming of the pulse generator, however as the clocking is derived from the pump laser and not the single photon emission, it is not an event-ready reconfiguration. Driving voltages were optimized by maximizing the coincidence counts between the different channels.

To verify the correct operation of the switches, as well as their synchronization with the master laser, we first reconstruct the time histograms of two-photon coincidences counts between the first output of the demultiplexer and all other channels. The device is cyclically operated such that the first photon is sent to output one, the second to output two, and so on, and coincidences are measured between all four outputs simultaneously. Figure 2.12 shows three time histograms (from a total of six pairwise combinations) of the coincidences measured by all four detectors. We observe enhanced peaks in coincidences at the corresponding delays of our demultiplexer, together with suppressed counts at different delays, thus showing the correct functioning of our device. The non-vanishing coincidence counts (smaller peaks) in the histograms arise from imperfect fabrication of the modulated couplers. As one expects, the first main peak (coincidences between Channel 1 and Channel 2) is delayed by 12.5 ns (equivalent of the 80 MHz of the master laser pulses). The second main peak (coincidences between Channel 1 and Channel 3) is delayed by an additional 12.5 ns, therefore centering it on the mark of 25 ns. Likewise, an additional 12.5 ns delay for the third main peak (coincidences between

switch	1	2	3
on	0.87±0.06	0.94±0.05	0.90±0.06
off	0.06±0.02	0.13±0.03	0.13±0.05

Table 2.1: Splitting ratios of the switches calculated from the data in Fig. 2.12., with uncertainty from the fit confidence. Non-zero off values are caused by incorrect driving voltages, and non-unity *on* values by waveguide imperfections.

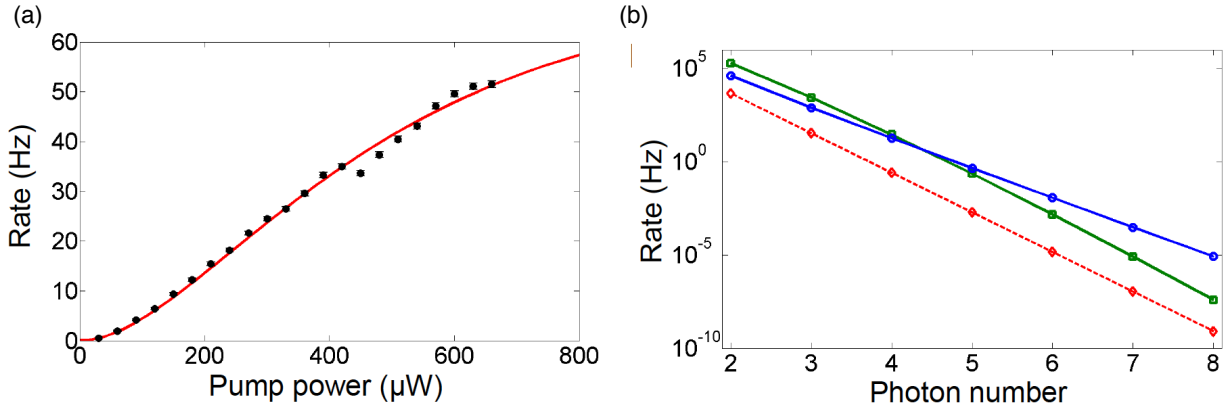

Figure 2.13: (a) Saturation curve showing the two-photon coincidences $c_{DM}(2)$ at Channel 1 and Channel 2 of our demultiplexer and the measured excitation power (black dots). Error bars were included, but are too small to be easily visible. The red curve shows the best fit to our data. We measured the saturation power as $P_0 = 348 \pm 16$ μW. The little disturbance near 400 μW was due to mechanical drift and realignment of the QD in reference to the pump laser to fix this issue. (b) Comparison between the estimated photon rates at the output of the demultiplexer of an active (blue ○) and probabilistic (green □) demultiplexing schemes for an improved QD pumped under resonant excitation, QD2016 [37]. The graph (red ◊, dotted line) shows the rate of n heralded single photon sources with brightness of 0.75%, based on data from [37].

Channel 1 and Channel 4). The height of the main peak is affected by the transmission through the waveguide. The two smaller peaks are affect by the transmission through the waveguide, but primarily by undesirable cross-talk between channels.

From the data depicted in Fig. 2.12, we calculated the splitting ratios of the three switches for both settings using a least-squares fitting procedure, and the result is presented in Table 2.1. The presence of non-zero off values and non-unity on values reveals the non-ideal operation of the device. The absence of counts at zero time delay (at the same level of accidental counts) is due to the low $g^{(2)}(0)$ value of the source, measured separately as $g^{(2)}(0) = 0.029 \pm 0.001$ at $P = 3P_0$ in Reference [90], where P_0 stands for the saturation power.

The measured power-dependent rate of two-photon coincidences $c_{DM}(2)$ at outputs 1 and 2 of our demultiplexer is shown in 2.13 (a). As expected for a QD pumped under quasi-resonant excitation, it follows a saturation function $c_{DM}(2) = c_{max}(2)[1 - exp(P/P_0)]^2$, quadratic in the P-dependence of the single-photon brightness. A fit to the data results in $c_{max}(2) = 70.9 \pm 3.0$ Hz, the maximum detected 2-photon rate, and $P_0 = 348 \pm 16$ μW the saturation power. We measured two-fold and three-fold

photon coincidence rates of 65 ± 10 s^{-1} and 0.11 ± 0.02 s^{-1}, respectively, at the output for a pump power P = 660 μW. The switching efficiency η_{DM} is finally estimated by fitting all ten combinations of two and three photon coincidence rates with Eq. 2.1, with $R = 80$ MHz, $\eta_{det} = 30\%$, and $\eta_{SD} = 0.76\%$ is calculated from the total number of counts measured with the four detectors. We find an average switching efficiency $\eta_{DM} = 78 \pm 6\%$, in good agreement with the value $\eta_{DM} = 80 \pm 9\%$ predicted from the measured splitting ratios. Four-fold coincidences were predicted to be 0.18 ± 0.06 ms^{-1} due to the low value of T in the current system, producing insufficient statistics in the acquisition time of 87 min. Dark counts of our detectors were ~ 300 s^{-1} per detector, giving no significant contribution to coincidence measurements.

To investigate the potential of our technology for the realisation of a multiphoton source with larger numbers, we calculate the expected photon rates at the output of the demultiplexer for a QD with 15% polarised brightness pumped under resonant-excitation, the QD2016 also introduced in Chapter 1 [37]. The total transmission of our demultiplexer is tested by coupling the waveguide with a Gaussian mode from an single-mode optical fibre and is found to be $T = 30\%$. This value is compatible with an overlap with the waveguide mode $\simeq 85\%$, as measured from mode imaging at the output of the waveguide, 14% Fresnel losses at the input and output facets, and propagation losses $\simeq 0.65$ dB/cm, and is the same value measured from a straight waveguide fabricated on the same chip, meaning that the couplers and electrodes did not introduce extra losses. In Fig. 2.13(b) we report the expected photon rates for increasing photon numbers calculated for a pump rate $R = 80$ MHz, $\eta_{DM} = 78\%$, and a transmission $T = 0.3/(0.86 \times 0.86)$ corrected for Fresnel losses, that can be eliminated with an anti-reflection coating at the input and output facets. The QD brightness is corrected for an additional loss factor of 65% that takes into account the coupling efficiency of the QD emission mode to a single-mode fibre [90]. The proposed system with these parameters is expected to outperform a probabilistic demultiplexing scheme, made of a network of passive beamsplitters with zero propagation losses, for a number of photons $n > 4$ and would enable a 6-photon rate $\simeq$ 0.01 s^{-1}. The same calculation for a resonantly-excited QD with 14% brightness measured at the ouptut of a single-mode fibre [91], would enable, instead, a 6-photon rate $\simeq 0.1$ s^{-1}. This technology offers great potential for further improvement, in particular by the use of the Reverse Proton exchange technique [84] for an improved coupling with optical fibres and reduced surface-scattering losses we estimate that we can achieve insertion losses lower than 3 dB. Furthermore the switching efficiency of the couplers can be increased with an optimized driving voltage and waveguide fabrication process. Such upgrades will enable the scaling of this platform to a larger number of photons.

2.6 Conclusion

We proposed and experimentally implemented active demultiplexing with a single integrated device using single photons from a solid-state source, the first demultiplexer of its kind. The performance of the demultiplexer was analyzed in conjunction with a QD pumped under quasi-resonant excitation and we have discussed the potential of our technology for an improved quantum dot. The proposed

demultiplexing device is of general interest for any bright temporally distributed single-photon source and provides a scalable approach for the realisation of multiphoton sources of larger photon numbers. Our platform thus constitutes a very promising approach for scalable quantum photonics.

The reader might be interested in other works [92–94] on demultiplexing single photons published after our work. Additionally, studies on the scalable performance of quantum dots sources can be found in References [90, 95].

Parts of the following publication have been incorporated as Chapter 3.

[3] **Raphael A. Abrahao** and Austin P. Lund, Continuous-Variables Boson Sampling: Scaling and Verification, *arXiv:1812.08978*, 2018.

Contributions to article [3]:

Raphael A. Abrahao and Austin P. Lund equally contributed to this project.

Chapter 3

Continuous-Variables Boson Sampling: Scaling and Verification

This Chapter is based on the article **Continuous-Variables Boson Sampling: Scaling and Verification** available on *arXiv:1812.08978*, which I am the first author [3]. Parts of this publication are incorporated here.

3.1 Introduction

What are the limits of computation? Are there physical systems that are impossible to simulate on classical computers? Does quantum computation provide any advantage over classical computation? Can we probe the hierarchy of computational complexity classes or the Extended Church-Turing Thesis using quantum computing? Over the last years, some of the above questions—explained in more detail in following discussion—have been started to be addressed. Although definitive answers to all these questions are not known yet, crucial steps have already been made and others are nearby.

3.2 A glimpse into Computational Complexity

Algorithms can be classified according to their computational complexity. This means the hardness of the execution of an algorithm is compared to the amount of time it would take and the required memory resources it uses. The complexity class tells how the resources requirements (time and memory) for a certain calculation scale as the problem becomes larger. These classes allow us to know the limits of feasible computation. Consider here an example where n measures the "size", the number of operations required to complete the computation, each operation taking, for the sake of exemplification, 1 μs. Algorithms with polynomial time complexity remain feasible even for large n values, whereas algorithms with exponential or even worse (factorial) scaling quickly become infeasible for large inputs. See Fig. 3.1. In practice, the computational complexity class to which a certain algorithm belongs poses the limit of the feasibility of the computational task.

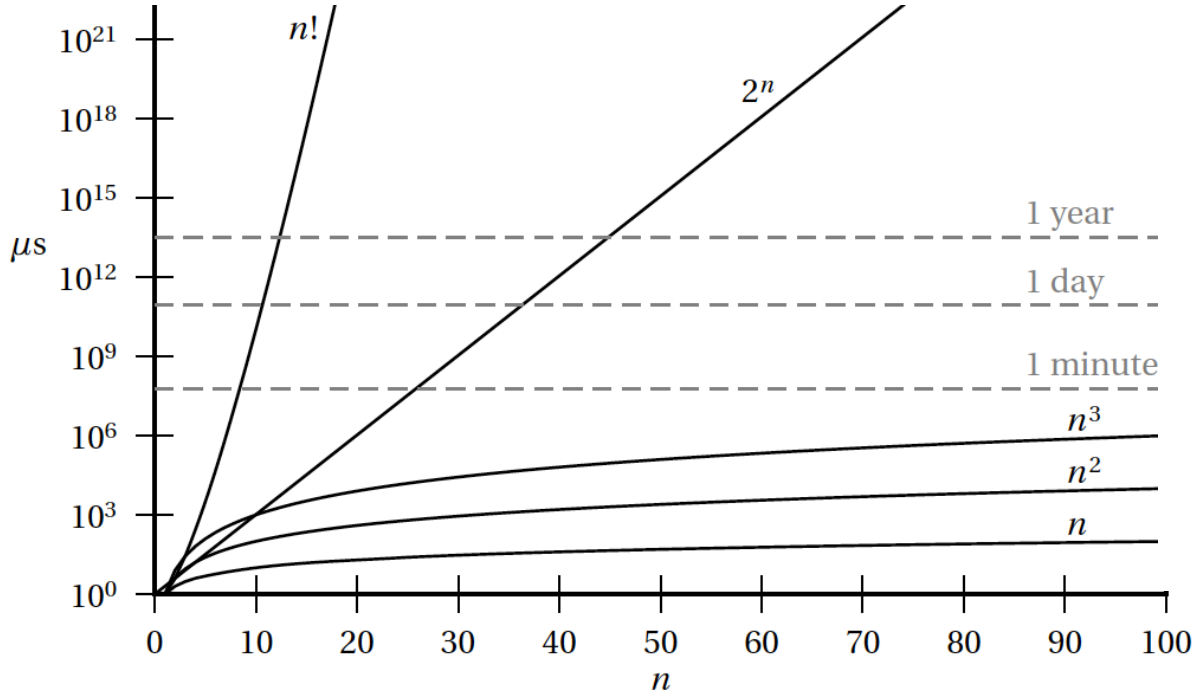

Figure 3.1: Runtime of algorithms with different computational complexities. In this picture, n measures the number of operations required to complete the computation, each operation taking, for the sake of exemplification, 1 μs. This picture plots some polynomial curves (n, n^2, n^3), an exponential curve (2^n), and a factorial curve ($n!$), each associated with the asymptotic behaviour of an algorithm. Note the vertical axis is in logarithm scale. Dotted lines are insert to indicate 1 minute, 1 day, and 1 year. In practice, the computational complexity class to which a certain algorithm belongs poses the limit of the feasibility of the computational task. Credit of image: [96] (adapted).

3.2.1 Computational Complexity Classes

In order to compare different algorithms and to provide a general framework, computational problems are classified into computational complexity classes. Here we introduce some of these classes and their definitions. A diagram of some of these classes is presented in Fig. 3.2.

- **P - Polynomial-Time**: "The class of decision problems solvable in polynomial time by a Turing machine[1]" [98].
  Some very important problems are in the P class such as linear programming, "finding a maximum matching in a general graph" and "the problem of testing whether an integer is prime" [98–101].

- **NP - Nondeterministic Polynomial-Time**: The class of decision problems solvable by a "non-deterministic polynomial-time Turing machine" [98].

[1]The definition of a Turing machine is discussed in References [96, 97]. We can assume without loss of generality that a Turing machine is what is called a classical computer.

- **NP-complete**: "A decision problem is NP-complete if (1) it is in NP, and (2) any problem in NP can be reduced to it (under some notion of reduction)" [98]. A well-known example of an NP-complete problem is the travelling salesman problem, which can be defined as: "given a set of n cities, and the distance between each pair of cities, is there a route that visits each city exactly once before returning to the starting city, and has length at most T?" [98].

- **coNP**[2]: "a decision problem X is a member of co-NP if and only if its complement $\bar{X}$ is in the complexity class NP. In simple terms, co-NP is the class of problems for which there is a polynomial-time algorithm that can verify 'no' instances (sometimes called counterexamples) given the appropriate certificate. Equivalently, co-NP is the set of decision problems where the 'no' instances can be accepted in polynomial time by a non-deterministic Turing machine." [102]

- **#P**: "The class of function problems of the form 'compute *f(x)*', where *f(x)* is the number of accepting paths of an NP machine" [98]. The calculation of the permanent of a matrix is in #P [103].

- **BPP - Bounded-Error Probabilistic Polynomial-Time**: "The class of decision problems solvable by an NP machine such that: if the answer is 'yes' then at least 2/3 of the computation paths accept; if the answer is 'no' then at most 1/3 of the computation paths accept" [98].

- **BQP - Bounded-Error Quantum Polynomial-Time**: "the class of decision problems solvable in polynomial time by a quantum Turing machine[3], with at most 1/3 probability of error. One can equivalently define BQP as the class of decision problems solvable by a uniform family of polynomial-size quantum circuits, with at most 1/3 probability of error" [98, 104]. In practice, "BQP is often identified as the class of feasible problems for quantum computers" [98].

An important result to highlight is that if one has a candidate solution for an NP problem, this can be checked in P, i.e., polynomial time. For example, the Sudoku game is an NP problem, however, if one gets a proposed solution, one can quickly check if this answer is correct. From here, we can build an intuition that for such problems, to check an answer is much easier than to find the correct answer. From arguments like that, and the computational feasibility of P problems (see Fig. 3.1), one can see why so much effort is dedicated to find algorithms that fall into the P class. This leads to the motivation for one of the most important open problems in Mathematics[4], simply referred as $\mathrm{P} \stackrel{?}{=} \mathrm{NP}$.

3.2.2 Polynomial Hierarchy

The Polynomial Hierarchy was introduced by Stockmeyer [105] and was eloquently summarized, together with its consequence, as following:

[2]Do not confuse coNP with the complement of the class NP. Note that $\mathrm{coNP} \cap \mathrm{NP} \neq \emptyset$.

[3]We can assume without loss of generality that a quantum Turing machine is what is called a quantum computer.

[4]This is one of the Millennium Problems from the Clay Mathematics Institute, which offers 1 million US dollars for the person who solves it.

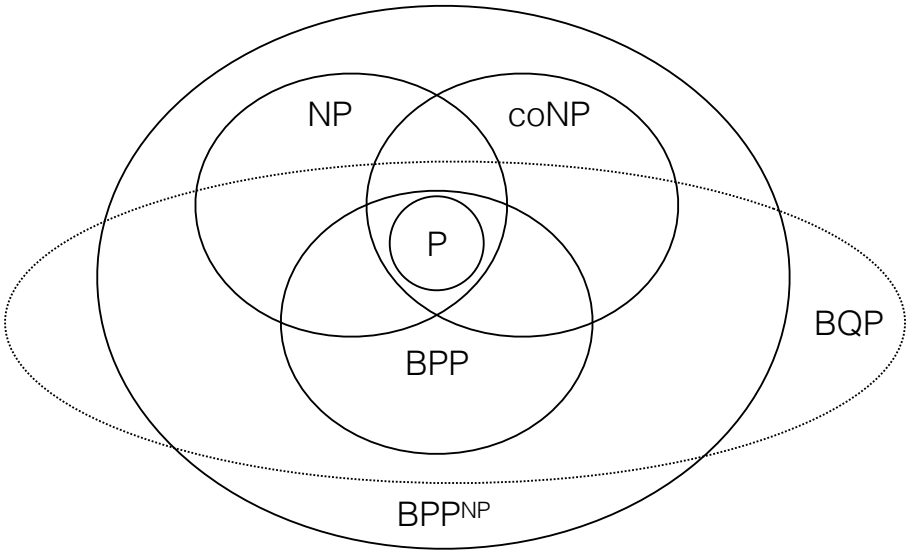

Figure 3.2: Computational complexity diagram. The different computational classes are discussed in the text. Note the dotted line for BQP, which indicates that the border of BQP might change as we better understand quantum computation and its full potential.

"A commonly used technique in complexity theory is to prove statements relative to an 'oracle'. This is basically an assumption of access to a machine that solves a particular problem instantly. Using this concept one can define a nested structure of oracles called the 'polynomial hierarchy' [105] of complexity classes. At the bottom of the hierarchy are the classes P and NP which are inside levels zero and one, respectively. Then there is the second level which contains the class NP^{NP} which means problems solvable in NP with access to an oracle for problems in NP. If P $\neq$ NP then this second level is at least as powerful as the first level and possibly more powerful due to the ability to access the oracle. Then the third level contains $NP^{NP^{NP}}$, and so on. Higher levels are defined by continuing this nesting. Each level of the hierarchy contains the levels below it. Though not proven, it is widely believed that every level is strictly larger than the next. This belief is primarily due to the relationships of this construction to similar hierarchies such as the arithmetic hierarchy for which higher levels are always strictly larger. If it turns out that two levels are equal, then one can show that higher levels do not increase and this situation is called a polynomial hierarchy collapse. A polynomial hierarchy collapse to the first level would mean that P = NP. A collapse at a higher level is a similar statement but relative to an oracle. It is the belief that there is no collapse of the polynomial hierarchy at any level that is used in demonstrating the supremacy of quantum sampling algorithms. Effectively one is forced into a choice between believing that the polynomial hierarchy of classical complexity classes collapses or that quantum algorithms are more powerful than

classical ones." (Reference [106]).

3.3 Introduction to Boson Sampling

Boson Sampling is a model of intermediate—as opposed to universal—quantum computation initially proposed to confront the limits of classical computation compared to quantum computation [107]. An efficient classical computation of the Boson Sampling protocol would support the Extended Church-Turing Thesis (ECT) "which asserts that classical computers can simulate any physical process with polynomial overhead" [108], i.e., polynomial time and memory requirements. But an efficient classical algorithm for Boson Sampling would also imply that the Polynomial Hierarchy (PH) of complexity classes, which is believed to have an infinite number of discrete levels, would reduce (or "collapse") to just three levels. Consequently, a computer scientist cannot simultaneously support the Extended Church-Turing Thesis and an infinite structure of the PH. Hence one is cornered into a position that either a fundamental change in computational complexity is needed or quantum enabled algorithms must be able to perform some tasks efficiently that cannot be performed efficiently on a classical computer. An example of such a task is the quantum Shor's algorithm [109] for factorization which is an extremely important result due to the role that factoring prime numbers has in cryptography[5]. Even in the absence of a full-scale quantum computer, a physically constructed Boson Sampling device could outperform a classical device sampling from the same distribution, and therefore, it is one of the leading candidates in the quest for a quantum optical demonstration of quantum computational advantage [106, 108, 111, 112]. The first experimental demonstration of quantum computational advantage was published in October 2019 for a sampling problem using 53 superconducting qubits [113].

An important step on the formulation of the Extended Church-Turing Thesis (ECT) was done by D. Deutsch in 1985 [114] stressing its formulation in a more physical context. The conflict between the Extended Church-Turing Thesis and quantum computation was firstly argued, to the best of my knowledge, by Ethan Bernstein and Umesh Vazirani [115] [6]. In an attempt to disprove the the Extended Church-Turing Thesis, one searches for a way to experimentally falsify it, usually employing a quantum computing protocol. Regarding that, even in the seminal paper of Boson Sampling [107], the authors argue that no finite experiment, i.e. an experiment with finite number of input single photons, could conclusively refute the Extended Church-Turing Thesis given the fact that Boson Sampling relates to ECT Thesis in the asymptotic limit when the number of input photons tends to infinity, yet strong evidence against the ECT Thesis could still be provided with a finite experiment. Following on that, Rohde *et al.* [116] stressed the difficulty of disproving the ECT Thesis when considering the asymptotic behaviour of their error model.

Shor's factoring quantum algorithm [109] not only provides a practical application of quantum computing, but also leads to important consequence in computational complexity classes. The factoring

[5] Another example is the problem of forrelation, in which "one needs to decide whether one Boolean function is highly correlated with the Fourier transform of a second function" [110].

[6] Reference [115] dates back to 1997, however a preliminary abstract dates back to 1993.

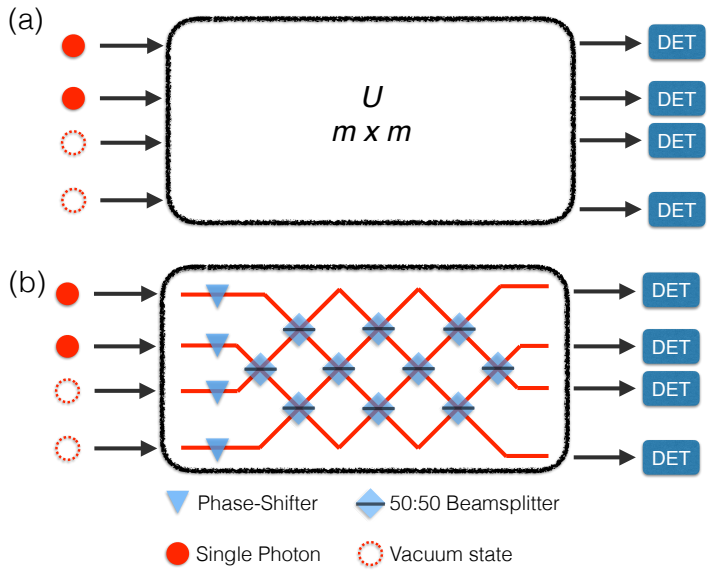

Figure 3.3: (a) Conceptual schematics for the Boson Sampling protocol: n photons, here $n = 2$, enter a linear optical network whose action is represented by a m x m unitary matrix (U), here $m = 4$, which relates the input amplitudes to the output amplitudes. The $m - n$ remaining inputs are considered to be in a vacuum state. The outputs are recorded using single-photon detectors (DET). (b) Conceptual implementation of Boson Sampling. Here the unitary U is implemented in spatial modes using phase-shifters and 50:50 beamsplitters.

problem consists of finding the prime factors for a given number Λ, different than 1 and Λ itself. Shor's quantum algorithm [109] can compute the prime factors of a given number Λ in polynomial time, that is, polynomial in the number of digits of Λ [65]. At the present moment, there is no known classical algorithm capable of computing the prime factors of a given number in polynomial time. The consequence of Shor's algorithm for computational complexity is state by [107], summarised here as: if classical computers can simulate quantum mechanical program efficiently (i.e. polynomial time), then, classical computers must also efficiently (polynomial time) solve the factoring problem.

Linear optical circuits with post-selection are known to be able to perform universal quantum computation [117]. In particular the Knill-Laflamme-Milburn (KLM) [118] protocol shows how this can be implemented using "beam splitters, phase shifters, single photon sources, photo-detectors and quantum memory" by exploiting post-selection and error correction to achieve arbitrarily high probabilities of success. Boson Sampling is a restricted model of quantum computation, which means that not all state transformations can be achieved and hence it is not universal. The original proposal for Boson Sampling by Aaronson and Arkhipov [107] is based on the manipulation of single photons using linear optics and is sometimes referred to as a discrete variable approach. Consider n indistinguishable single photons injected on a network of linear optics with m modes, where $m \gg n$, at least $m = n^2$. The Boson Sampling protocol assumes that the linear network is described by a large unitary matrix U. But one can take advantage of a decomposition where any unitary network in linear optics can be decomposed in a network of beamsplitters and phase-shifters whose number is quadratically related to the unitary matrix dimension (Fig. 3.3). The most commonly used decomposition of

this form is the Reck decomposition [119], while a recent symmetric and optimized version can be found in Reference [120]. The output of a Boson Sampling device is not deterministic and hence is mathematically represented by a probability distribution over the outputs of detecting the photons. What a Boson Sampling device does is not to compute the output probability distribution but to output *samples* from this distribution. The form of the underlying probability distribution for Boson Sampling is used to argue about the computational hardness of this sampling problem. The distribution can be expressed in terms of matrix permanents of the submatrices of the unitary describing the linear optical network. The matrix permanent is a quantity computed similarly to the matrix determinant, but without the alternations of "+" and "–" signs. Permanents[7,8] are in the complexity class #P, and thus computationally hard to calculate [103].

In a simplified view, an implementation of the Boson Sampling protocol can be summarized as follows: n indistinguishable single photons are inputs into the ports of a m modes linear optical network, represented by a unitary matrix U, and at the output ports single-photon detection is performed (Fig. 3.3). Any alleged Boson Sampling device must give samples from this output distribution for any given U.

3.4 Implementations of Boson Sampling

The early experiments of Boson Sampling provided proof-of-principle demonstrations, limited to 2 to 4 input photons in 5 to 6 modes [127–130]. All these demonstrations used single photons produced by Spontaneous Parametric Down Conversion (SPDC), discussed in Chapter 1, a nonlinear and intrinsically probabilistic process. In SPDC, a pump laser is directed through a nonlinear crystal, and when the phase-matching and energy conservation conditions are fulfilled, a pair of single photons in the down-conversion output modes can be probabilistically produced. As the process is coherent, the photon number (Fock basis $|n\rangle$) representation is given by:

$$\sqrt{1-\chi^2}\sum_{n=0}^{\infty}\chi^n\,|n_1 n_2\rangle\,, \tag{3.1}$$

where n_i is the photon number on the i^{th} mode and $0 \leq \chi < 1$ is a parameter representing the strength of the SPDC. The higher order terms with $n > 1$ are generally undesirable and can generate errors in most quantum information processing protocols [131]. Therefore, SPDC sources are not typically run at high power to decrease the probability of producing the higher order terms. This state is also a Gaussian state with covariance matrix

$$\begin{pmatrix} \cosh 2r & 0 & \sinh 2r & 0 \\ 0 & \cosh 2r & 0 & -\sinh 2r \\ \sinh 2r & 0 & \cosh 2r & 0 \\ 0 & -\sinh 2r & 0 & \cosh 2r \end{pmatrix}, \tag{3.2}$$

[7] In a series of lectures [121–124], Scott Aaronson provides two intuitive arguments for the computational hardness of permanents. Contrary to the matrix determinants, permanents: (i) do not present any symmetry (in general, symmetries provide shortcuts in calculations); (ii) do no have a geometrical interpretation.

[8] The early discussions of permanents in the context of linear optical networks can be found in References [125, 126].

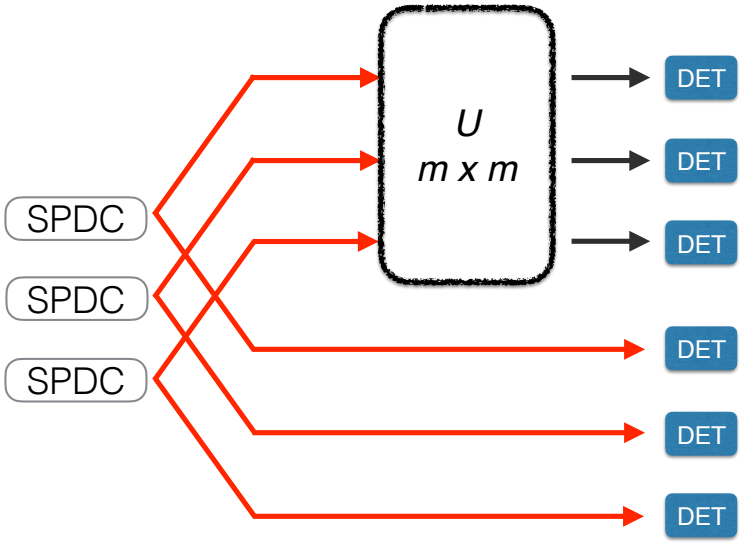

Figure 3.4: An example of Boson Sampling using the "scattershot" method [132]. The setup uses three Spontaneous Parametric Down Conversion sources and a linear optical network depicted here as the Unitary U. Detection is recorded by single-photon detectors (DET). This protocol takes advantage of the vast multitude of combinations from multiple independent SPDC sources.

(using scaled X and P to vacuum noise) where we have written the squeeze parameter r such that $\chi = \tanh(r)$. Another way to write this is in terms of squeezing relative to the vacuum state in decibels. This is computed by comparing the smallest covariance eigenvalue, which is e^{-2r}, to the vacuum and computing the logarithmic decibel quantity,

$$dB = 20r\log_{10}(e) = 10\log_{10}\left(\frac{1+\chi}{1-\chi}\right). \tag{3.3}$$

An important step towards scalability is a variant of the Boson Sampling protocol called "Boson Sampling from a Gaussian State" [132] (a.k.a. scattershot) (Fig. 3.4), a protocol already demonstrated at small scales [133]. In this alternative version Lund *et al.* [132] proved that Gaussian states can be injected as inputs while the outputs are projected on the number basis by using single-photon detectors such as Avalanche Photodiodes (APDs) or Superconducting Nanowire Detectors (SNDs). Note that, in general, APDs and SNDs[9] are not number-resolving single-photon detectors, i.e., they operate on a "click/no-click" basis, and a "click" event means that at least one photon was detected. However, as explained before, the probability of producing the high order terms in the SPDC is minimized by reducing the input power that drives the SPDC process. Therefore, APDs and SNDs have been commonly used on Boson Sampling experiments. The scattershot Boson Sampling takes advantage of the vast multitude of combinations from multiple independent SPDC sources generating a particular total number of photons in the output modes as Eq. 3.4, irrespective of which mode each pair is probabilistically generated in.

Alternatively, solid-state single-photon sources based on Quantum Dots (QD) [46, 135], discussed in Chapter 1, have achieved good rates of single-photon production. Demonstrations of Boson

[9] Superconducting Nanowire Detectors (SND) can present photon-number resolution limited to low Fock states [134].

Sampling using QD started in 2017 [136, 137] and achieved the current world record with 20 photons in a 60-mode photonic circuit [138].

More recently, a new variant of Boson Sampling was proposed in which the Boson Sampling protocol is formulated in terms of the Hafnian of a matrix, a more general function, and also belonging to the #P class. This protocol is called Gaussian Boson Sampling [139, 140]. However, it must be remembered that the use of Gaussian input states for Boson Sampling was previously known from the scattershot Boson Sampling [132]. A demonstration of scattershot, Gaussian, and standard Boson Sampling using integrated optics and single photons from Spontaneous Four Wave Mixing (SFWM) sources can be found in Reference [141].

From the experimental point of view, it is imperative to establish how tolerant Boson Sampling is to photons losses. This question is commonly rephrased as determining the scaling of the rate of photon loss that permits an efficient classical simulation of Boson Sampling, hence nullifying any computational advantage [142–150]. In particular, let us revisit three results on photon loss: (i) Arkhipov [142] demonstrated the tolerance in error of each element of the optical network should scale as $O(1/(n^2 \log m))$ for the requirements of the Boson Sampling protocol to remain valid; (ii) Oszmaniec *et al.* [147] argue "the output statistics can be well approximated by an efficient classical simulation, provided that the number of photons that is left grows slower than $\sqrt{n}$"; (iii) García-Patrón *et al.* [148] argue "all current architectures that suffer from an exponential decay of the transmission with the depth of the circuit [...] can be efficiently simulated classically" and "either the depth of the circuit is large enough that it can be simulated by thermal noise with an algorithm running in polynomial time, or it is short enough that a tensor network simulation runs in quasipolynomial time", and explicitly state that a new paradigm for implementation of Boson Sampling is needed in order to reach quantum computational advantage. One implementation demonstrated tolerance for few photons losses [83].

3.5 Applications of Boson Sampling

It is noteworthy that the current search for applications of Boson Sampling goes beyond the scope of computational complexity. For instance, Boson Sampling has been adapted to simulate molecular vibrational spectra [151, 152] and may be used as a tool for quantum simulation [153, 154]. Other Boson Sampling-inspired applications are the verification of NP-complete problems [155], quantum metrology sensitivity improvements [156], and a quantum cryptography protocol [157]. Moreover, other platforms, specially superconducting qubits, are being employed for reaching the quantum computational advantage [113, 158, 159].

3.6 The problem: the current status of Boson Sampling

Proof-of-principle implementations of Boson Sampling have been successfully demonstrated, initially using single photons from Spontaneous Parametric Down Conversion (SPDC) and later using

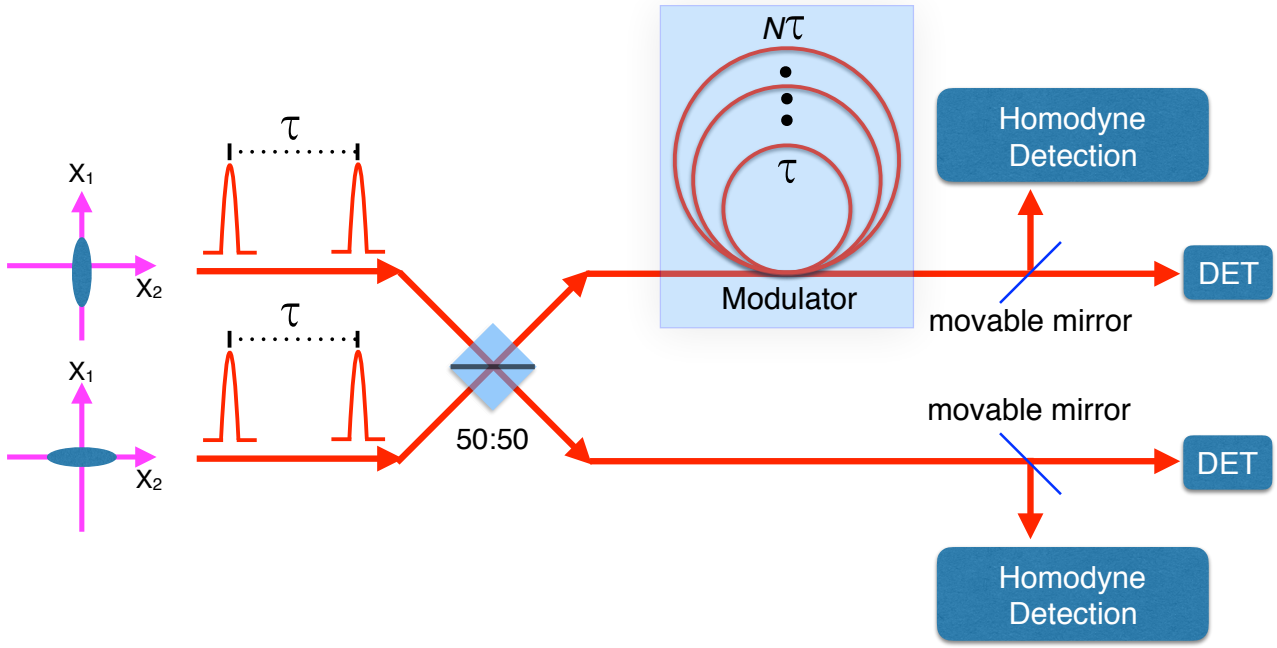

Figure 3.5: Schematics for continuous-variable Boson Sampling using temporal encoding. Input states are pulsed-Gaussian-squeezed states on orthogonal basis, whose temporal difference is given by τ. Those 2 inputs interfere on a 50:50 beamsplitter. The photons in the upper arm enter a "Modulator", while photons in the bottom arm propagate freely. In each arm, movable mirrors are placed to direct light to a characterization stage using Homodyne Detection. After the characterization, the movable mirrors must be removed and let light go to the corresponding single-photon detectors (DET) to generate the output (samples) for the Boson Sampling protocol, this last stage similarly to the scattershot case [132].

Quantum Dots (QD) [83, 127–130, 133, 136–138, 160]. However, even the current world record of 20 photons in 60 modes [138] is well below any threshold of quantum computational advantage. Three factors are currently contributing against quantum demonstrations of Boson Sampling: (a) better classical algorithms which move the threshold of quantum computational advantage to greater number of input single photons [161, 162], e.g. the classical algorithm of Neville *et al.* [161] solved the Boson Sampling problem with 30 photons in a standard computer efficiently; (b) difficulties on the scaling of the preparation of manifold single photons ($n|1\rangle$); and (c) scaling of photon losses in the linear optical network [147–149]. Therefore, at this point in time Boson Sampling faces an unclear future with difficult perspectives. Motivated by these constraints, we present a new method to scale Boson Sampling experiments using continuous-variable quantum information and time-bin encoding. Our proposal also takes into account finite squeezing and given some reasonable assumptions hold, operational performance can be characterized efficiently.

3.7 The proposed solution: combining continuous-variables Boson Sampling with temporal encoding

Here we present an alternative way to scale Boson Sampling experiments based on continuous variables (CV) and temporal encoding. In the CV case, the information is encoded on the quantum modes of light, specifically, on the eigenstates of operators with continuum spectrum [16]. Continuous-variables quantum information has achieved impressive results. An initial report of 10,000 entangled modes in a continuous-variable cluster mode [163] was later upgraded to one million modes [164]. Some of these systems were conceived to perform Measurement-Based Quantum Computation (MBQC), and here we show they can be adapted to Boson Sampling. Moreover, while some of the theoretical works for MBQC assume unrealistically infinite squeezing, here we require only finite squeezing. The world record for detected squeezed light is 15 db [165], while it is estimated a 20.5 db threshold of squeezing is needed for fault-tolerant quantum computation using Gottesman-Kitaev-Preskill (GKP) encoding [166, 167].

The work of Lund *et al.* [132] (a.k.a. Scattershot Boson Sampling) demonstrated that Gaussian states can be used as inputs in Boson Sampling experiments and only bounded squeezing is necessary, provided each output is projected in the number basis by single-photon detection. It is important at this point to emphasise that the specific task of Scattershot Boson Sampling requires the generation of a different distribution than the standard Boson Sampling. One result presented in [132] was to show that sampling from this distribution is also a hard problem when employing classical computing resources. The single photon Boson Sampling distribution is contained within the Scattershot Boson Sampling distribution, but this is merely used as part of the proof for computational hardness. The requisite task is the efficient generation of samples from a Gaussian state measured in the Fock basis without any further processing.

A detailed discussion of how much squeezing is necessary for Scattershot Boson Sampling[10] experiments can be found on [132]. Interestingly, the authors [132] showed that for a two-mode squeezer, like SPDC, there is a trade-off between the strength of the SPDC (linked to χ) and the most likely number of photons detected represented by the variable n. This indicates that Scattershot Boson Sampling experiments that are done with fewer photons require higher χ levels:

$$P(n) = \underbrace{\binom{m}{n} \underbrace{\chi^{2n}(1-\chi^2)^m}_{\text{standard Boson Sampling}}}_{\text{scattershot Boson Sampling}}, \tag{3.4}$$

where this probability is locally maximised when

$$\chi = \sqrt{\frac{n}{m+n}} \tag{3.5}$$

[10] In the case of Scattershot Boson Sampling [132], m refers to the number of two-mode squeezers, i.e., the number of SPDC single-photon sources. In that paper, the condition $m = n^2$ was imposed. In the present work, we use a more general definition: m is simply the number of modes in the linear optical network represented by a m x m Unitary matrix (U).

and this maximum probability is lower bounded by $1/\sqrt{n}$ if $m \geq n^2$ and $n > 1$. In this regime, χ decreases as n increases and when taking $m = n^2$ at $n = 8$ only 3 dB of squeezing is required to achieve this optimal probability.

Now, we will introduce a new approach to scale Boson Sampling experiments. Consider two pulsed-squeezed-light sources, with time interval τ between subsequent pulses, where these two states interfere on a 50:50 beamsplitter, followed by a controllable delay, where a pulse can be delayed by $N\tau$ before being released, see Fig. 3.5. This may be a loop architecture [168] or a quantum memory. The modulator should implement the desired unitary U operation by interfering delayed pulses. At the end of each spatial path, there are two possible measurement schemes that can be performed. Either, the light can be sent to a single-photon detector to record the samples (output) for Boson Sampling, or the light is directed towards a homodyne detection [13, 169] setup that is used to characterize the output state from the optical network.

A significant benefit of this approach is that, under some reasonable assumptions, the operation of the sampling device can be characterized using the sampling state itself without the need for other probe input states. To achieve this, the following assumptions are needed: (i) the output state received by the single-photon detection is the same as that received by the homodyne detection, which is achievable by movable mirrors, for example as in the procedure given by [170]; (ii) the two squeezed input states are Gaussian and that the modulation network changes the states but leaves the output still in a Gaussian form, a standard Gaussian optics property; (iii) the output is fully characterized by a multi-mode covariance matrix, and finally (iv) the choice of when to make a sampling run and when to make a characterization run is irrelevant. In other words, the experimental setup is assumed stable and the output will not change over the time as one changes between the two different measurement schemes.

A Gaussian output state can be fully characterized by the mean vector (which we will assume zero) and covariance matrix. For a m mode state and n detected photons, the number of possible photon number detection events scales as m^n. However, to describe a Gaussian state before the detection has occurred, only the number of entries in a covariance matrix for a m modes state is required and this scales as $4m^2$. For the case of Gaussian input Boson Sampling (a.k.a. scattershot) where there are two groups of m modes and n photon detections, the size of the Fock basis detection sample space is m^{2n}, but the full covariance matrix for the state prior to detection will require $16m^2$ entries.

Performing the characterization involves reconstructing the covariance matrix from the CV measurement samples. The measurements chosen must be sufficient in number to estimate all elements of the covariance matrix, including terms involving the correlations between X and P in the same mode. To avoid repeated changes of measurement settings, we propose to perform this by means of dual homodyne. In a dual-homodyne arrangement, the signal mode is split at a 50:50 beamsplitter and both modes undergo a CV homodyne detection, one measured in X and the other in P. This permits a simultaneous measurement of the X and P quadratures at the cost of adding $1/2$ a unit of vacuum noise to the diagonal elements of the state covariance matrix. So, if Σ is the state covariance matrix, then the dual homodyne modes will present Gaussian statistics with a covariance matrix of $(\Sigma + I)/2$ (under

units where the variance of vacuum noise is unity), where I is the identity operator. This covariance matrix can then be estimated by constructing matrix-valued samples from each sampling run. Let

$$s_i = (x_{1,i}, p_{1,i}, x_{2,i}, p_{2,i}, \ldots, x_{m,i}, p_{m,i})^T \tag{3.6}$$

be a $2m$-dimensional real vector representing the i^{th} data sample from the dual-homodyne measurement with the first subscript representing the mode to which the corresponding homodyne detector is attached. From this sample vector, a sample matrix can be formed from the outer product of the s_i

$$\xi_i = s_i s_i^T. \tag{3.7}$$

This sample matrix is then a positive semi-definite matrix for all i. The expectation value for each sample ξ_i over the incoming Gaussian distribution is then

$$\langle \xi_i \rangle = (\Sigma + I)/2 \tag{3.8}$$

and so a sample average over K samples

$$\bar{\xi} = \frac{1}{K} \sum_{i=1}^{K} \xi_i \tag{3.9}$$

will be an unbiased estimator for $(\Sigma + I)/2$.

To see how close the sample average is to the true average, we apply the operator Chernoff bound [171, 172] (following the notation of Wilde [171], Section 16.3). This gives the probability that the sample average deviates significantly from the expected value. Let K be the number of sample matrices and $\bar{\xi}$ the sample average of K samples as defined in Eq. 3.9. The input state covariance matrix Σ is positive definite, and we have

$$(\Sigma + I)/2 \geq I/2 \tag{3.10}$$

which is the expectation of each operator forming the sum in Eq. 3.9. For this situation, the operator Chernoff bound for any $0 < \eta < 1/2$ is given by

$$Pr\{(1-\eta)(\Sigma + I)/2 \leq \bar{\xi} \leq (1+\eta)(\Sigma + I)/2\} \geq 1 - 8me^{-K\eta^2/(8\ln 2)}. \tag{3.11}$$

To then bound the probability for making a multiplicative estimate of Σ, the spectrum of Σ needs to be bounded away from zero.

Let the parameter b represent the variance of the quadrature for the maximum possible squeezing for the state being estimated. This means that

$$\Sigma \geq bI. \tag{3.12}$$

The Chernoff bound for the estimator $\bar{\xi}$ can be rewritten as

$$Pr\{(1-\eta)\Sigma - \eta I \leq 2\bar{\xi} - I \leq (1+\eta)\Sigma + \eta I\} \geq 1 - 8me^{-K\eta^2/(8\ln 2)}. \tag{3.13}$$

Then using the inequality in Eq. 3.12, this can be written as

$$Pr\{(1-\eta(1+b^{-1})\Sigma) \leq 2\bar{\xi} - I \leq (1+\eta(1+b^{-1})\Sigma)\} \geq 1 - 8me^{-K\eta^2/(8\ln 2)}. \tag{3.14}$$

This means the rewritten estimate $2\bar{\xi} - I$ gives a multiplicative estimate of the covariance matrix Σ.

The interpretation of Equation 3.14 is that the chance that the finite sample estimate of the covariance matrix deviates from the true value decays exponentially in the number of covariance matrix samples K and the square of deviation permitted η, but depends linearly on m, the number of modes. In our application of Gaussian input Boson Sampling, the value of b is fixed as too much squeezing can actually degrade performance. So for fixed η, as the number of modes m increases, the number of samples K required to achieve the same probability bound in the operator Chernoff bound only grows logarithmically $\mathcal{O}(\ln m)$.

3.8 Continuous-Variables Boson Sampling: Verification

One would like to verify if the generated state is sufficient to perform the task at hand, that is Boson Sampling. For approximate Boson Sampling, one does not need to generate the state ideally but within some trace distance bound ε. Using the Fuchs-van de Graff inequality, the trace distance is upper bounded by the fidelity by $1 - F < \varepsilon$. A robust certification strategy is given by Aolita *et al.* [173], which tests if a fidelity lower bound (or equivalently maximum trace distance) holds between a pure Gaussian target state and a potentially mixed preparation state. In order to perform the verification, the Gaussian covariance matrix elements need to be estimated and manipulated with knowledge of the target pure state. This produces a bound of the fidelity which can be used to test for appropriateness of the apparatus to perform Gaussian input Boson Sampling. The samples needed to achieve a fixed fidelity bound (or fixed trace distance) is higher than the Chernoff bound and scales as $\mathcal{O}(m^4)$ times, where m is the number of modes in the state being verified. This verification process can require considerable amounts of data to scale, but the scaling with system size is polynomial, making the process feasible. This is as opposed to the verification in the discrete variables model as addressed in the same paper [173] which requires $\mathcal{O}(nm^n)$ samples to approach the target state when verifying a process with n photons in m modes.

3.9 Continuous-Variables Boson Sampling: Sampling

After the stage of verification is finished, the movable mirrors must be removed to direct the light toward the single-photon detectors. Doing so, one is projecting the Gaussian states into a Fock basis, and thus obtaining the output of the Boson Sampling experiment, as in the Gaussian input Boson Sampling (a.k.a. scattershot) [132]. Our proposed method greatly simplifies the numbers of required resources for scaling Boson Sampling experiments. Here we benefit from having well verified states, with verification growing polynomially as discussed above, and from having only two squeezed light sources, and thus simplifying the preparation of input states. Our method also requires less

detectors. For instance, if one wishes to implement a 20 input single photons Boson Sampling, then it requires a 400 x 400 linear optical network, and therefore 400 single-photon detectors. Not obeying $m \gg n$, at least $m = n^2$, violates the mathematical assumptions upon which the approximate Boson Sampling problem is currently formulated, and therefore can only be interpreted as an experimental proof-of-principle. In our proposal, due to the time-bin implementation of the linear optical network, only 2 single-photon detectors are required.

3.10 The role of imperfections

An important consideration for the performance of any sampling device is the role that imperfections, originating from any process, have on the ability to draw conclusions about the classical easiness or hardness of computing random samples. Crucially, the dominant imperfection using current technology is photon loss. The effects of photon loss are included within the approximate sampling requirements, i.e., how much one can deviate from the perfect sampling. Unfortunately, this does not mean that losses can be neglected, as they will in many cases give rise to exponential scaling in the total variation distance between the lossless distribution and lossy distribution. For example, a constant loss rate for each mode will induce an exponential scaling in the total variation distance as a function of the number of photons to be detected. It would seem that this implies that any level of loss would render classically hard Boson Sampling impossible, but this is not the case. The goal to demonstrate the quantum computational advantage only requires producing samples that are close to some distribution, given some ε tolerance, that is hard for a classical computer to reproduce. Aaronson and Brod [144] showed that the distribution generated from losing a fixed number of photons (i.e. not scaling with the number of photons) is hard for a classical computer to sample. A lossy Boson Sampling device will be close to this distribution at some scale. Unfortunately, the total variation distance for constant loss per mode will still asymptotically scale exponentially against this distribution with a fixed number of lost photons. Oszmaniec and Brod [147] showed that if the total number of photons that remained after loss scaled as $\sqrt{n}$ of the number input photons n, then a simple distribution from sampling distinguishable bosons would satisfy the total variation distance requirement for approximate sampling. Hence an efficient classical computation could reproduce samples close to the required Boson sampling distribution, nullifying the quantum computational advantage. In a later article, Brod and Oszmaniec studied the case of nonuniform losses. [150]. Despite advances in understanding the effect of losses [142–150], there remains a gap between the necessary and sufficient criterion for the hardness of approximate sampling with lossy Boson Sampling devices, which makes this an important open question. All implementations will be subject to imperfections, including the proposed implementation presented here. However, in this present work, we are primarily concerned with the experimental implications of scaling and verifying continuous-variables Boson Sampling. We expect that future results on the hardness of lossy Boson Sampling would be able to be incorporated into the proposal we present.

3.11 Conclusion

Continuous-variables (CV) quantum information, particularly in the context of optical Gaussian states [174], has been put forward as an alternative for quantum computation. Due to the scaling factors discussed in the previous sections, we point out that Boson Sampling can greatly benefit from the current optical CV technology [163–165, 175–177]. In this sense, all the building blocks for this proposal have been successfully demonstrated and have good performance for scaling. The threshold for quantum computational advantage in the CV regime is currently uncertain and the subject of further investigation, but our Boson Sampling proposal certainly does not suffer from the scaling issues of discrete Boson Sampling, in particular the issue of preparing a large number of indistinguishable single photons.

In summary, we revisited the motivation behind Boson Sampling and the experimental challenges currently faced. Despite impressive improvements towards demonstrating a quantum computational advantage using Boson Sampling, the current number of input single photons and modes are considerably below what is necessary. Photon losses and scaling of many input single photons are factors working against quantum implementations of Boson Sampling. These facts pose great challenges and make evident a new scalable approach is necessary. Here we presented a new method to do so based on continuous variables and temporal encoding. Our method assumes finite squeezing and also provides a feasible way to perform the characterization of the input states and the verification of the Boson Sampling protocol, providing viable scaling as the system size increases. With this approach, the quest for a quantum optical demonstration of quantum computational advantage moves closer to experimental reality.

Parts of the following publication have been incorporated as Chapter 4.

[2] L. A. Howard, G. G. Gillett, M. E. Pearce, **R. A. Abrahao**, T. J. Weinhold, P. Kok, A. G. White, Optimal imaging of remote bodies using quantum detectors, *Physical Review Letters* 123, 143604, 2019.

Contributions to article [2]:

The theory for this article was developed by P. Kok and M. E. Pearce. The design and construction of experiment was done by L. A. Howard, G. G. Gillet, R. A. Abrahao, and T. Weinhold. Data acquisition was conducted by L. A. Howard and R. A. Abrahao. The codes for running the number-resolving detectors were developed by G. G. Gillett. The simulation was developed by L. A. Howard. The manuscript writing was done by L. A. Howard, P. Kok, R. A. Abrahao and A. G. White. This project was supervised by P. Kok and A. G. White.

Chapter 4

Optimal Imaging of Remote Bodies using Quantum Detectors

This Chapter is based on the article **Optimal Imaging of Remote Bodies using Quantum Detectors** available on [2], which I am an author. Parts of this publication are incorporated here. In the experiment reported in this chapter, we used Transition Edge Sensors (TES) as our photon detectors. They have the ability to resolve the number of impinging photons. The reader may find more details about our TES system on Appendix A.

4.1 Introduction

Quantum metrology aims to explore quantum mechanical properties in order to make more precise measurements [178–180]. One problem where quantum metrology can provide a significant benefit is in imaging, where one wants to access the information contained in the spatial characteristics of a object or light source. In particular, quantum metrology can help with estimating parameters without an associated quantum observable, like phase or time. Moreover, quantum metrology can help with multi-parameter estimation, especially when two or more parameters are not co-measurable, i.e., in mathematical terms, they do not commute [181]. Additionally, quantum metrology can provide bounds on the precision to which some parameters can be experimentally determined.

In Classical Optics, we already face the problem of the limit up which one can spatially resolve objects. The Rayleigh, Abbe, and Sparrow limits state that the size of the smallest resolvable features is determined by the ratio of the wavelength and the numerical aperture. The smallest distance $\mathscr{D}$ such that two objects can still be distinguished from each other is given by

$$\mathscr{D} = \frac{k}{2}\frac{\lambda}{n\sin(\theta)} = \frac{k}{2}\frac{\lambda}{NA}, \tag{4.1}$$

where λ is the wavelength of light, n is the refractive index, NA is the numerical aperture, and k is a constant for the different criteria on the diffraction limits, see Fig. 4.1.

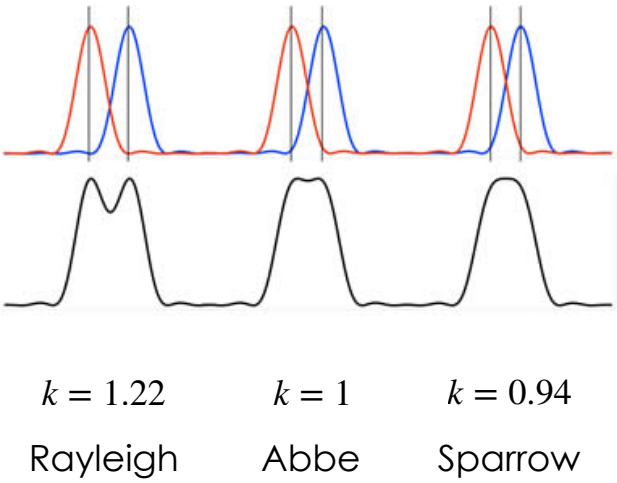

Figure 4.1: Diffraction limits for the Rayleigh, Abbe, and Sparrow criteria. For each curve, it is implicitly assumed and intensity *vs* lateral spatial distance plot. Credit of image: [192].

To circumvent the limitation imposed by diffraction, several techniques may be employed, and these can be classified in two main groups: super-resolution techniques [182–184] and entanglement-assisted techniques where the object of interested is illuminated using entangled states of light [185–191]. However, one open problem remains: what if the object of interest is inaccessible and all one has access to is the state of the emitted light from this object? This is very similar to the situation astronomers face.

In this chapter, we use quantum metrology techniques to address one specific problem: given a finite size imaging system in the far field—i.e., systems with a finite effective numerical aperture—what is the best way to estimate the transverse spatial distribution of the light source?

Recently Tsang *et al.* [193] showed that the far field quantum state of light retains a significant amount of information about the separation of two identical incoherent point sources, even when their angular separation approaches zero. Moreover, this information can be extracted with a suitable measurement [194], for example using spatial-mode demultiplexing [195]. Additionally, a series of experiments demonstrated sub-Rayleigh resolution for two incoherent point sources, using image inversion interferometry [196], digital holography [197], and TEM_{01} heterodyne detection [198]. However, the retention of the spatial information seems to be restricted to highly symmetric sources [199], and it is an open question how one can optimally extract the spatial characteristics of arbitrary sources. Possible candidates include conventional telescopes, Hanbury Brown-Twiss interferometry[1] [19–22, 200], or estimating higher-order correlations in the far field [201–203].

[1] A quantum version of the Hanbury Brown-Twiss interferometer was discussed in Chapter 1.

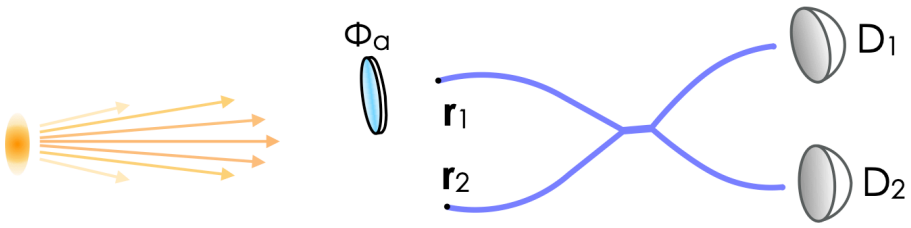

Figure 4.2: Schematic for the Count, Traditional, and Click schemes for estimating the complex degree of coherence (CDC) of the light field at positions $\mathbf{r}_1$ and $\mathbf{r}_2$. This arrangement provides a general imaging procedure since the CDC is directly related to the Fourier transformation of the source distribution via the van Cittert-Zernike theorem. The incoming light fields at $\mathbf{r}_1$ and $\mathbf{r}_2$ are interfered at a fibre beamsplitter, the output of which is sent to detectors D_1 and D_2. In the Count scheme the detectors are photon-number resolving and the phase shift ϕ_a is random; the Traditional scheme is similar except the phase is fixed. In the Click scheme the phase is random but the detectors act as not photon-number resolving, instead recording events if one or more photons are present.

4.2 Optimal Imaging of Remote Bodies: Methods

In this project, we consider the important practical case where we do not know the light source distribution, and therefore do not have a simple theoretical model whose parameters we can estimate. This requires that we measure quantities with a special relation to the source distribution, such as the complex degree of coherence (CDC). The van Cittert-Zernike theorem relates the CDC to the source distribution via a two-dimensional Fourier transform [204]. Pearce *et al.* [205] showed that the CDC, $\gamma(\mathbf{r}_1,\mathbf{r}_2)=|\gamma|e^{i\phi}$, between two points $\mathbf{r}_1$ and $\mathbf{r}_2$ in the imaging plane can be measured nearly optimally using the setup in Fig. 4.2. The two main features are application of a varying phase ϕ_a to one mode of the incoming light and measurement using number-resolving photon detectors, which we call the Count scheme.

We experimentally implement the Count scheme, and compare it to two other methods, called Traditional and Click schemes. The Traditional scheme is the two-mode analog to a traditional lensing and intensity measurement setup where the variable phase is replaced by a fixed phase. The Click scheme uses a variable phase but disregards the number resolution. In this Click scheme the detectors merely record an event whenever one or more photons are detected, similar to avalanche photodiode detectors (APD) or Superconducting Nanowire Detectors (SND) without number resolution. Note that, Superconducting Nanowire Detectors (SND) can present limited photon-number resolution [134].

The optimality of the Count scheme is claimed under the theoretical model developed in Reference [205] using the quantum Cramér-Rao bound and the quantum Fisher information. The quantum Fisher information $F(\xi)$, say for estimating a parameter ξ, tell us the maximum information one could extract with an optimal measurement. The quantum Cramér-Rao bound states the minimum error achievable on estimating ξ. Mathematically [16],

$$\langle(\Delta\xi)^2\rangle \geq \frac{1}{NF(\xi)}, \tag{4.2}$$

where ξ is a parameter to be estimated, N is the number of experimental runs, and $F(\xi)$ is the quantum Fisher information for ξ.

In our experiment, the quantum Cramér-Rao bound relates the mean squared error (MSE) matrix for these parameters to the quantum Fisher information matrix determined by the light field captured in the detectors [205, 206]. The quantum Fisher information depends on the state of light and the Positive-Operator Valued Measure (POVM) of detection. The quantum Fisher information in turn determines the optimal measurement observables, leading to the setup in Fig. 4.2. While the parameters of interest $|\gamma|$ and ϕ have non-commuting measurement observables, they turn out to be jointly measurable [205]. The relation between the quantum Cramér-Rao bound and the quantum Fisher information is discussed in greater detail in Reference [16].

The complex degree of coherence (CDC) is determined directly from interference fringes between two spatially separated optical modes in the far field. Light at positions $\mathbf{r}_1$ and $\mathbf{r}_2$ acquires a relative applied phase shift ϕ_a (using the phase shifter in Fig. 4.2), then interferes on a 50:50 beam splitter, and is finally detected by photon-number-resolving detectors D_1 and D_2, with x being the number of photons in detector D_1 and y the number of photons in D_2. Post-selecting on different photon-number coincidence events $[x,y]$ gives rise to different interference fringes. The results will be discussed in Section 4.4 (Data Analysis) where we show these photon-number resolved interference fringes (Fig. 4.7). Note that these calibration fringes are not used for the experimental estimates (Figures 4.8 and 4.9).

The phase ϕ of the CDC contains the information about the position of the source relative to the optical axis connecting the source and the imaging plane. To see this, we note that a transversal shift of the source in the direction parallel to $\mathbf{r}_1-\mathbf{r}_2$ produces a relative phase shift in the optical modes at $\mathbf{r}_1$ and $\mathbf{r}_2$. This results in a translation of the interference fringes. The phase ϕ of the CDC is equal to the applied phase ϕ_a at the point where the fringes are all at extremal values. For example, we can infer from Fig. 4.7 (top right) that ϕ is slightly less than π for the calibration dataset.

The magnitude $|\gamma|$ of the CDC contains the information about the spatial extent of the source, and is equal to the visibility of the fringes,

$$|\gamma| = \frac{I_{max}^{[x,y]} - I_{min}^{[x,y]}}{I_{max}^{[x,y]} + I_{min}^{[x,y]}}, \tag{4.3}$$

where $I_{max}^{[x,y]}$ and $I_{min}^{[x,y]}$ are respectively the maximum and minimum intensity of the interference fringe for detector coincidence events $[x,y]$. To see this, we note that each single point at the source creates an interference fringe with perfect visibility and $|\gamma|$=1. Incoherent extended sources at different positions then create an incoherent superposition of horizontally translated interference fringes. As the spatial extent of the source increases, the visibility—and hence $|\gamma|$—of the resulting interference fringe decreases. These relationships are formally expressed in the van Cittert-Zernike theorem.

4.2.1 Source size and angle estimation

Our determination of the beam diameter from the visibility calculations used the expression

$$|\gamma|(d) = \exp[-d^2/(2\sigma_d^2)], \tag{4.4}$$

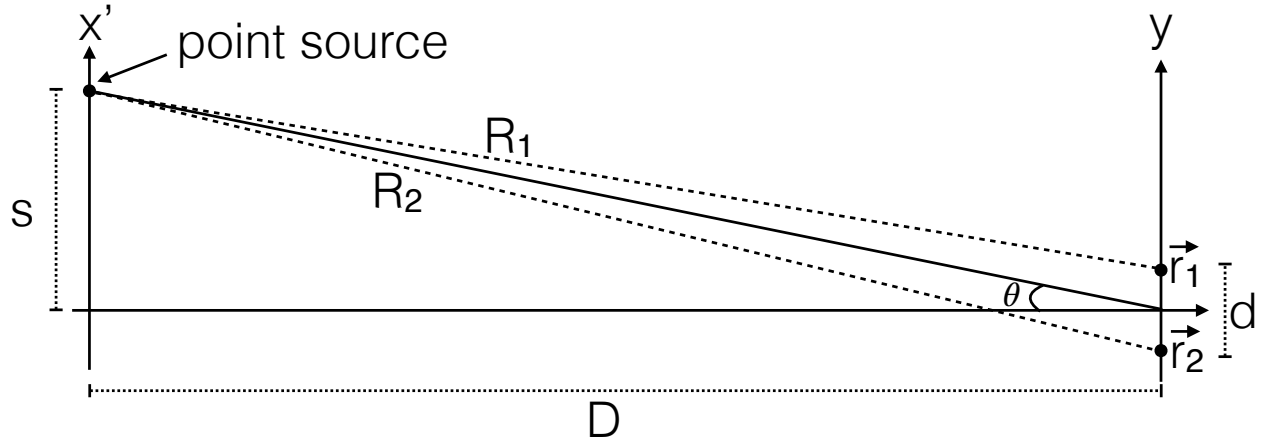

Figure 4.3: Geometry of the source distribution. Two detectors at $\mathbf{r}_1$ and $\mathbf{r}_2$ are placed along the y-axis perpendicular to the optical axis. The incoherent point source makes an angle θ with the optical axis at a distance D from the detector plane. The relationship between the phase ϕ of the CDC and the angle θ is given by Eq. 4.10.

where λ is the wavelength, $|\gamma|$ is the visibility of the fringes, L is the distance from the source to the detectors, d is the distance between the detectors, $\sigma_d{=}\lambda L/(2\pi\sigma_y)$ is the spatial frequency characteristic, and σ_y is the standard deviation of a Gaussian source.

To define the relationship between the estimated parameter ϕ and the angle to the source, we first consider an incoherent point source distribution in the object plane in one dimension, given by the intensity distribution $I_s{=}I_0\delta(x'{-}s)$, with I_0 being the total intensity of the source and $\delta(x'{-}s)$ the Dirac delta function. Up to a constant factor, the complex degree of coherence is then given by [25]

$$\gamma \propto \int_S I_s(\vec{r'}) e^{ik(R_2-R_1)} d\vec{r'}\,, \tag{4.5}$$

where k is the wave number of the light emitted by the point source. The distances R_1 and R_2 are shown in Fig. 4.3, and are given by

$$R_1^2 = D^2 + \left(s - \frac{d}{2}\right)^2 \quad \text{and} \quad R_2^2 = D^2 + \left(s + \frac{d}{2}\right)^2 . \tag{4.6}$$

Using the approximation $\sqrt{1+x} \approx 1 + \frac{1}{2}x$ for $x \ll 1$ and $\frac{s\pm\frac{d}{2}}{D} \ll 1$, we find that for a point source at an arbitrary position x' along the vertical source axis

$$R_2 - R_1 = \frac{x'd}{D}\,. \tag{4.7}$$

This allows us to calculate the phase of the CDC from

$$\gamma \propto \int_{-\infty}^{\infty} \delta(x'-s) e^{ikx'd/D} dx' = e^{\frac{iksd}{D}} = e^{i\phi}\,, \tag{4.8}$$

with ϕ the phase of $\gamma = |\gamma| e^{i\phi}$. This immediately yields $\phi = ksd/D$. The physical angle θ is given by

$$\theta = \arctan\left(\frac{s}{D}\right) \approx \frac{s}{D}, \tag{4.9}$$

which leads to the relationship

$$\phi = kd\theta. \tag{4.10}$$

The phase of the CDC is therefore directly proportional to the angle of the source position, modified by a factor kd that depends on the wavelength $\lambda = 2\pi/k$ of the light and the distance d between the detectors. As expected, shorter wavelengths and larger detector separation will lead to an increased sensitivity in the position angle θ when measuring the phase of the CDC.

For a uniform source extending from $x' = s - a/2$ to $x' = s + a/2$ with integrated intensity I_0, the complex degree of coherence is proportional to

$$\gamma(d) \propto \int_{s-\frac{a}{2}}^{s+\frac{a}{2}} e^{ikx'd/D} dx' = \left(\frac{kd\,a}{2D}\right) e^{iksd/D}. \tag{4.11}$$

For known values of I_0, k, d, and D, as the size of the source a grows, the magnitude $|\gamma|$ is reduced, and $|\gamma|$ therefore gives a direct measure for a.

Next, we show that this information can be extracted from the visibility of the fringes. Consider the intensity I in the far field due to two points, 1 and 2, in the source plane. According to standard coherence theory (see Section 4.3.1 in Mandel and Wolf [25]) this is given by

$$I = I_1 + I_2 + 2\sqrt{I_1 I_2}\,|\gamma|\cos\phi\,, \tag{4.12}$$

where I_1 and I_2 are the average intensities in the far field due to the two points, respectively. The visibility of the fringes in the far field can then be calculated as

$$V = \frac{I_{max} - I_{min}}{I_{max} + I_{min}} = \frac{2\sqrt{I_1 I_2}}{I_1 + I_2}\,|\gamma|\,, \tag{4.13}$$

where I_{max} and I_{min} are the maximum and minimum intensities in the far field corresponding to $\cos\phi = +1$ and $\cos\phi = -1$, respectively. Assuming a uniform intensity distribution $I_1 = I_2$, we can immediately identify the visibility of the fringes with the magnitude of the CDC.

4.2.2 Maximum Likelihood Estimator (MLE)

To extract the values of $|\gamma|$ and ϕ from a measured interference fringe we use the maximum likelihood estimator (MLE), which is asymptotically efficient. This means that the variance of the MLE asymptotically approaches the Cramér-Rao bound for large datasets. The MLE optimises $|\gamma|$ and ϕ to fit the experimental data to the probability distribution $\Pr(x,y) = f_{x,y}(\gamma, \bar{n}, \phi_a)$ for detecting a coincidence event $[x,y]$. This distribution is a function of $|\gamma|$, ϕ, the average photon-number $\bar{n}$, and the applied phase ϕ_a. The probability function $P_r(x,y)$ used to calculate the maximum likelihood estimator (MLE) is given by [23]:

$$P_r(x,y) = \sum_{n_1=0}^{x+y} \frac{p_{in}(n_1, x+y-n_1)}{n_1!(x+y-n_1)!} \frac{x!y!}{4^{x+y}} \left| \sum_{j=0}^{x} (-1)^j \binom{n_1}{j} \binom{x+y-n_1}{x-j} (1-e^{-i\phi})^{x+n_1-2j} (1+e^{-i\phi})^{x-n_1+2j} \right|^2, \tag{4.14}$$

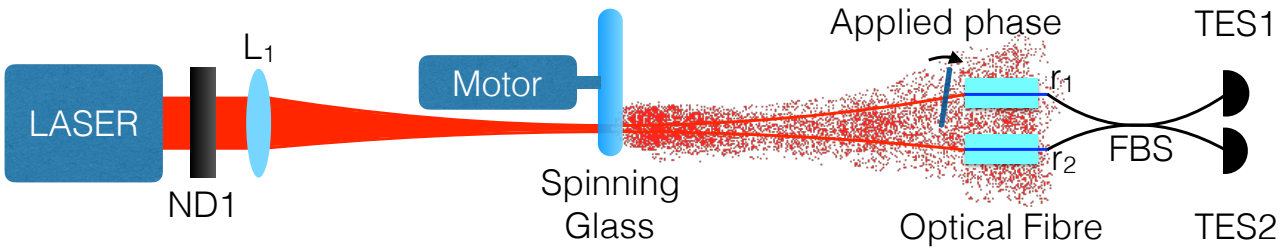

Figure 4.4: Setup for the optimal imaging experiment. A 10 kHz pulsed 820 nm laser is attenuated with a neutral density filter (ND1) and focused on a ground glass plate spinning at 5 Hz. This rotation turns spatially coherent light into spatially incoherent (thermal) light. In the far field, the light is collected into two optical fibres $\mathbf{r_1}$ and $\mathbf{r_2}$ with a glass plate located in front of $\mathbf{r_1}$ such that as it tilts, a relative phase shift ϕ_a is being applied to the light collected in $\mathbf{r_1}$. Both fibres are connected to a 50:50 fibre beamsplitter (FBS). The outputs are connected to two Transition Edge Sensors, TES1 and TES2, which are detectors with high detection efficiency and photon-number resolution. The operation of TES detectors is discussed in Appendix A. Additional discussions on pseudothermal light sources can be found in References [207–210].

where

$$p_{in}(n_1,n_2) = \frac{z_1^{n_1}}{(1+z_1)^{n_1+1}} \frac{z_2^{n_2}}{(1+z_2)^{n_2+1}}, \tag{4.15}$$

and $z_1 = \bar{n}(1-|\gamma|)$, $z_2 = \bar{n}(1+|\gamma|)$ and x and y are the number of photons in detectors D_1 and D_2 respectively.

4.3 Experimental setup

From the experimental point of view, the first task is to construct an incoherent (thermal) source of light. The obvious candidates are to collect light directly from stars or radiation from other blackbody source. For practical reasons, one can use pseudothermal light sources. We started with coherent light from a 10 kHz pulsed laser diode with wavelength of 820 nm. The light is coupled to a single-mode optical fibre, what provides a spatial filter. Out of the fibre, we have a Gaussian laser profile and this is attenuate through a neutral density filter to the low intensity regime of few photons. The light is then focused on a 5 Hz spinning glass with rough surface. The emerging light is then converted from a coherent state into an spatially incoherent state. In this way, we obtain a pseudothermal light source [207–210]. Figure 4.4 presents the experimental setup.

Light is collected using 2 single-mode optical fibres 48 mm apart from each other and at positions $\mathbf{r}_1$ and $\mathbf{r}_2$. In front of one of the optical fibres, a optical flat is placed in such a way that as it tilts, a controllable phase ϕ_a is being applied to the light. This optical flat, whose rotation axis is perpendicular to the page, creates a different optical path length. For the case of coherent light (diode laser), light from both fibres interferes, and due to the applied phase, interference fringes can be resolved. We use a 50:50 fibre beamsplitter (FBS) and fibre polarization controllers to ensure that both inputs in the FBS interference are of equal intensity. This is achieved using fibre polarization controllers with 1-2-1 loops, what has the net effect of QWP-HWP-QWP, see Fig. 4.5.

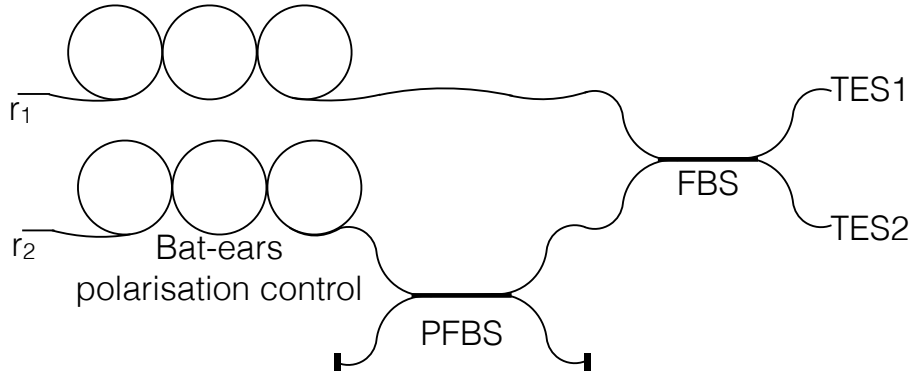

Figure 4.5: Polarization and intensity control. The fibre polarization controllers with 1-2-1 loops have the net effect of a conjunction of QWP-HWP-QWP. PFBS stands for polarization fibre beamsplitter. The fibre polarization controllers are adjusted in such a way that light of the same polarization and equal intensity enters the two inputs of the fibre beamsplitter (FBS) where interference happens. The outputs of the FBS are connected to TES1 and TES2 via fibre optics.

The outputs of the 50:50 fibre beamsplitter (FBS) are connected to our number-resolving photon detector systems, the Transition Edge Sensors (TES) [211]. They act as calorimeters measuring photon energy and provide true photon-number resolution when detecting monochromatic light. TES present high detection efficiency and no intrinsic dark counts. The TES output signal is amplified using low-noise electronics such as superconducting quantum interference device (SQUIDS). The TES provide a time stamp of the detection event and also record the number of photons in each detection. The operation of TES is discussed in more detail in Appendix A.

4.3.1 Phase calibration

Using electronic control, we tilt the optical flat in front of $\mathbf{r}_1$ in order to applied a phase shift ϕ_a, as indicated in Fig. 4.4. For the purpose of phase calibration, we electronically remove the spinning glass of the light path and send a coherent light (diode laser) into the experimental setup. As the applied phase ϕ_a varies, inference fringes can be observed from our data. From our number-resolving detectors we choose the [1,1] fringe for our phase calibration, in other words, fringe with 1 photon detected in TES1 and 1 photon detected in TES2. This choice was made due to high counts of [1,1] events and good signal to noise ratio. Number-resolved fringes are presented in Fig. 4.7. We arbitrarily assign to the rotation position of the first [1,1] extremum an applied phase of zero. The rotation position of the second [1,1] extremum will occur when the applied phase has increased to $\pi/2$. By the third extremum the applied phase has increased to π, and so on. These extrema are defined as the minimum and maximum points of a polynomial fitted to the fringe; the fringe, corresponding fitted polynomial and extrema points are shown in the left plot of Fig. 4.6. A final function giving the relationship between the optical flat rotation position α and applied phase of light entering r_1 ϕ_a is given by fitting a curve to the extrema points. This curve and extrema points are plotted on the right side of Fig. 4.6.

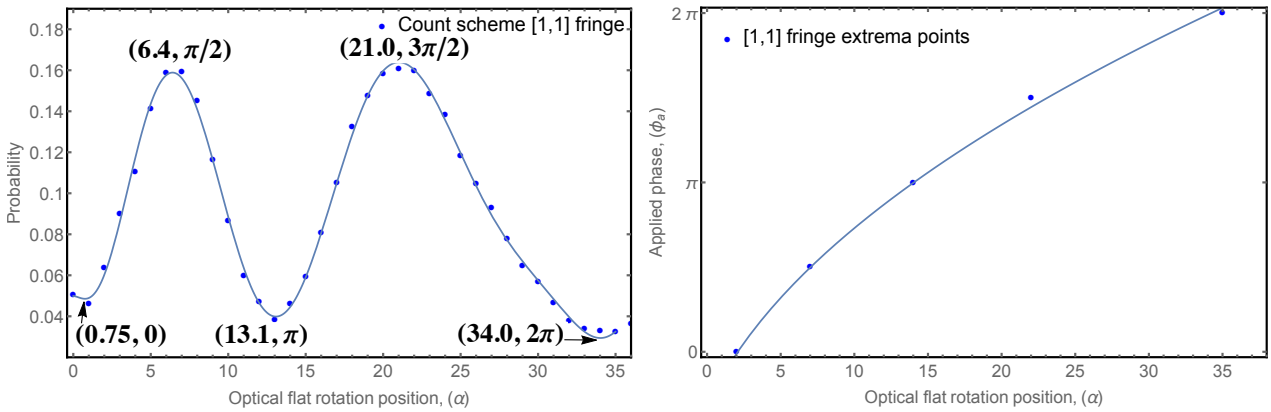

Figure 4.6: Left: An [1,1] interference fringe. The horizontal axis displays different rotational position of the optical flat, which acts to apply a varying phase to the light entering $\mathbf{r}_1$. The various rotation positions are dimensionless. The optical flat rotational positions corresponding to extrema and the applied phase at that extrema are also labelled. Right: A curve fitted to the labelled extrema points shown in the left plot provides a relationship between optical flat rotation position and applied phase. Using this relationship, the phase entering $\mathbf{r}_1$ can be determined at any rotational position of the optical flat. The equation of the fitted curve is $\phi_a = -2.6 + 1.5\sqrt{1.0+\alpha}$, where α is the optical flat mechanical rotation position.

The equation of the fitted curve is $\phi_a = -2.6 + 1.5\sqrt{1.0+\alpha}$, where α is the optical flat mechanical rotation position.

After the phase characterization is concluded, a pseudothermal state is inserted in the setup of our experiment by using the spinning glass technique, as discussed previously. With this pseudothermal state, data was collected and used for the calculations in schemes Count, Click, and Traditional. Our work uses the assumption that the applied phase ϕ_a varies with optical flat rotation in the same way as during the phase characterization. After the experimental data was taken, coherent light (diode laser without the spinning glass technique) is inserted again in the setup and phase characterization is performed again. This procedure is used to identify if substantial drift of optical apparatus occurred. Potential causes of such drift are temperature changes near the setup causing expansion or contraction of the parts, pressure gradients, and external mechanical vibrations. Based of the amount of drift present and the duration of the measurement, a decision is then made whether to keep the dataset. Typically, a drift of more than 10° per hour resulted in discarding the dataset.

4.4 Data Analysis

Measurements of coincidences in the number basis were taken using 35 different phases between zero and 2π radians. A maximum likelihood estimator (MLE) algorithm was then used to estimate $|\gamma|$ and ϕ by fitting a probability function (see subsection 4.2.2) to the measured coincidences as the applied phase was varied. For comparison of the Count and Traditional schemes, the MLE calculations used different numbers of samples of coincidence counts from 1000 to 10,000 points. Similarly, for comparison of the Count and Click schemes, the number of samples varied from 1000 to 20,000. The discrepancy in the range of datasets between the two comparisons is due to the Traditional scheme

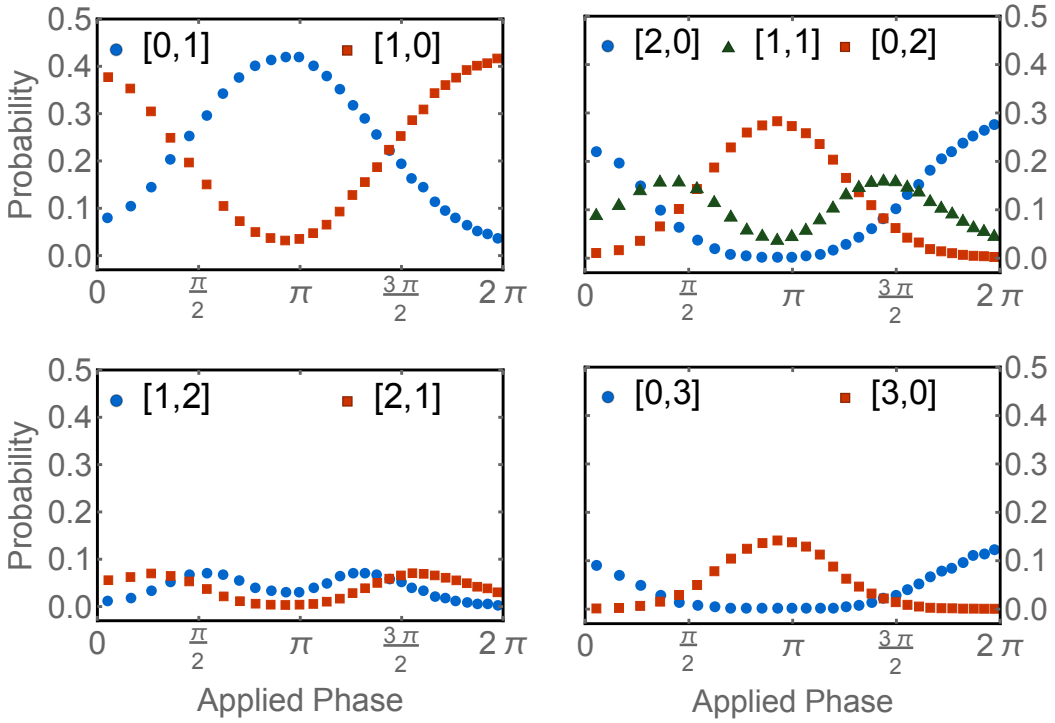

Figure 4.7: Number-resolved interference fringes. Light collectors at $\mathbf{r}_1$ and $\mathbf{r}_2$ from a weak coherent state light source. The plots show various photon-number coincidence events [x,y]—x photons in detector D_1, y photons in detector D_2—versus the applied phase ϕ_a. Significant visibility, and therefore information, remains as the total detected photon-number, x+y, increases.

measurements being a subset of the Count scheme data at one particular phase and hence containing less measurement data. A number of trials were taken at each dataset size, each using different samples from the total measurement dataset. Before any sample is taken from the total measurement set, the set is randomized and samples for each trial are selected such that no data point is used in more than one sample. The randomization ensures each sample contains a mixture of measurements with respect to the varied phase and time over which the measurements were taken. Due to the Traditional dataset being a subset of the Count dataset at one phase, the time over which its measurements were taken was approximately 1/35 the time over which the Count and Click schemes were taken. For this reason we can assume that the Traditional dataset is less affected by drift. All three methods, Count, Traditional and Click use the same one dataset, with the Traditional using a subset with one phase, Click ignoring photon-number information and Count using all phases and photon-number information. There were no outliers in the dataset and as such no points were removed at any time from the calculations.

Before comparing the precision of the Count scheme to the Traditional and Click schemes, we must discuss the accuracy of our estimates of $|\gamma|$ and ϕ. We determine this via two methods: (i) we compare the MLE values of $|\gamma|$ and ϕ to the values calculated directly from the fringes; (ii) we use the MLE for $|\gamma|$ and the van Cittert-Zernike theorem to estimate the diameter of the source, and compare it to a directly measured value of the source diameter. We calculated $|\gamma| = 0.096$ using Eq. 4.3 and we found $\phi = 4.11$ rad from averaging the applied phase ϕ_a at the extreme points for all fringes in the photon-number coincidence basis. For method (i), the visibility $|\gamma|$ was calculated from the average

Scheme	$\lvert\gamma\rvert = \lvert(kd\,a/2D)\rvert$	$\phi = kd\,\theta$
Count	0.096 ± 0.022	4.32 ± 0.25
Click	0.095 ± 0.025	4.29 ± 0.35
Traditional	0.20 ± 0.16	4.5 ± 1.0

Table 4.1: Complex degree of coherence magnitude, $|\gamma|$, and phase, ϕ, for the Count, Traditional and Click schemes. The size of the spot is a, the distance between $\mathbf{r}_1$ and $\mathbf{r}_2$ is d, the wave number is k, the distance from the source to the collection points is D, and the angle to the centre of the spot is θ. Values are the average for datasets of sizes 1000 to 10 000.

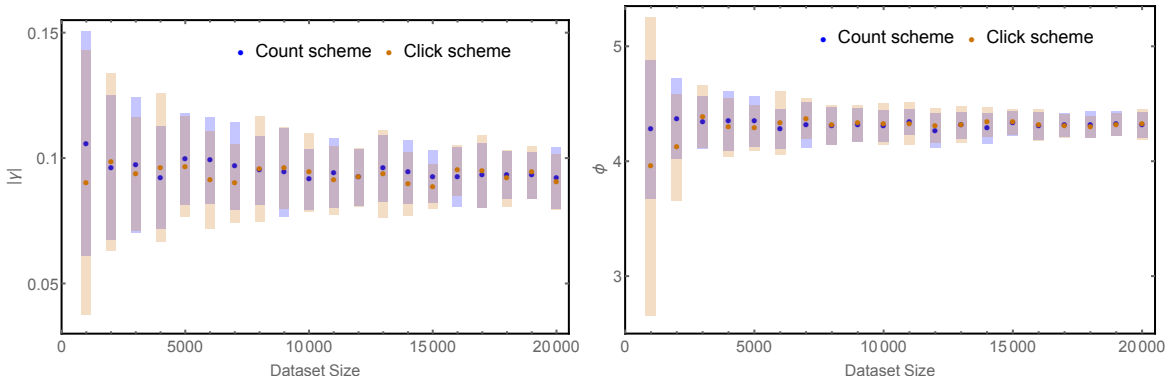

Figure 4.8: Comparison between Count and Click schemes for the complex degree of coherence for different dataset sizes. Left: magnitude $|\gamma|$. Right: phase ϕ. Each point is the mean of 50 trials with the shading representing the standard deviation of the 50 trials. Blue dots and shading are for the Count scheme and orange dots and shading are for the Click scheme. For small data sets, the Count scheme has a clear advantage over the Click scheme; both perform well at large dataset sizes.

of only the [0,1] and [1,0] fringes. The higher order fringes were not included due to the presence of increased noise. Outliers in the data would inflate their visibility. The MLE does not suffer from this drawback. The method (i) calculated values for both $|\gamma|$ and ϕ are consistent with the results of the MLEs for all three schemes.

For method (ii) we measured the source diameter, which is equal to the spot size of the beam incident on the ground glass plate, see Fig. 4.4. The ground-glass plate was placed within ± 0.25 mm of the beam waist. This uncertainty in position is due to a small amount of precession of the rotating plate. Using a beam profiler we measured the spot size at the waist to be 15.3 ± 0.1 µm and the spot size 0.25 mm from the waist to be 18.0 ± 0.1 µm. We therefore expect to estimate a source diameter in the range 15.3 -18.0 µm. Using the van Cittert-Zernike theorem and our estimated visibility we estimate the source diameter to be 16.5 ± 0.5 µm, agreeing well with the predicted range of diameters.

Table 4.1 summarises our estimates of the complex degree of coherence (CDC) magnitude $|\gamma|$ and phase ϕ using the Count, Traditional, and Click schemes, averaged over dataset sizes from 100 to 10000 points. For $|\gamma|$, the Count scheme is respectively 7.28 and 1.14 times more precise (smaller uncertainty) than the the Traditional and Click schemes; for ϕ, the Count scheme is respectively 4.0 and 1.4 times more precise (smaller uncertainty) than the the Traditional and Click schemes. Moving beyond these averages (not the values expressed in Table 4.1, but the last points in Fig. 4.9), for the

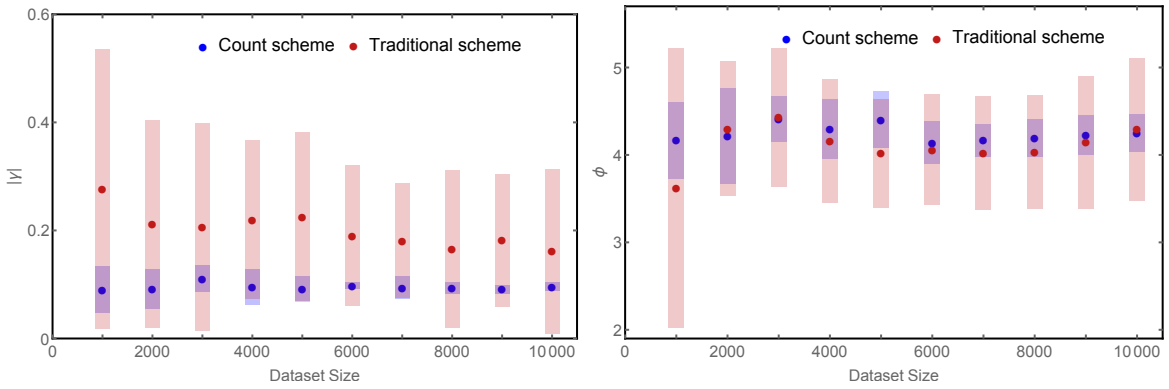

Figure 4.9: Comparison between Count and Traditional schemes for the complex degree of coherence for different dataset sizes. Left: magnitude $|\gamma|$. Right: phase ϕ. Each point is the mean of 20 trials with the shading representing the standard deviation of the 20 trials. Blue dots and shading are for the Count scheme and red dots and shading are for the Traditional scheme. The Count scheme clearly outperforms the Traditional scheme for all dataset sizes.

case with dataset of 10,000 points, the Count scheme is over an order of magnitude more precise (smaller uncertainty) for $|\gamma|$, and four times more precise for ϕ, than the Traditional scheme. These conclusions also apply to comparisons between the Click and Traditional schemes since Fig. 4.8 displays that the Count and Click schemes are of approximately equivalent precision for larger dataset sizes. These results demonstrate that the Count and Click schemes are significantly better than the Traditional scheme, corroborating the result by Pearce *et al.* [205] that the Count scheme is near optimal among non-collective measurements. Estimates for $|\gamma|$ and ϕ based on various dataset sizes are shown in Fig. 4.8 and Fig. 4.9. They reveal that the Count scheme converges more quickly around the true values of $|\gamma|$ and ϕ than the Traditional scheme. As we can see in Fig. 4.8, for large datasets, the non-number-resolving detection produces a small detrimental effect.

In the Traditional scheme we see a consistent bias in the $|\gamma|$ value estimates, relative to the Count or Click scheme, Fig. 4.9. This is due to the uncertainty in $|\gamma|$ for the Traditional scheme being greater than the difference between the $|\gamma| = 0.096$ value and the lower limit $|\gamma| = 0$. This results in truncation of some MLE estimates smaller than $|\gamma|$, causing inflation of the mean $|\gamma|$ estimation. Of the 3 schemes, the Traditional imaging has the worse performance.

4.5 Simulation

To benchmark our optimal imaging method, we present the results of simulating the Count and Traditional schemes. Firstly, we took a picture of Dory (Fig. 4.10 top left) as reference. For the propose of this simulation, we assumed $\lambda = 700$ nm (within the visible range), a detection array of 26×26 detectors, separation between pixels of 0.7 μm, and distance between the source and the detectors plane of 8.67 m. The van Cittert-Zernike theorem was then used to calculate the complex degree of coherence (CDC) for each pair of detectors. Then a two-dimensional Fourier transform reconstructs the image (intensity distribution) in the plane of the source image. Fig. 4.10 (top right)

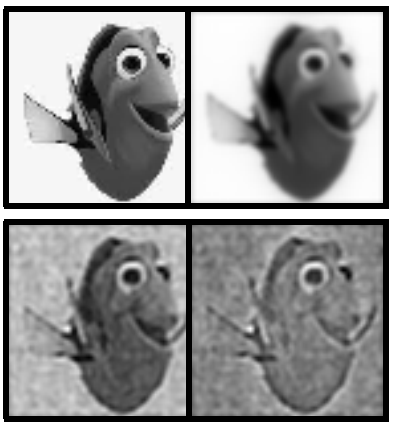

Figure 4.10: Simulated comparison of images reconstructed using the Count and Traditional schemes for a 26×26 array of detectors. The Click scheme is not shown due to the fact it visually looks very similar to the Count scheme. Top left: the original image. Top right: reconstructed image in a noiseless regime, revealing the theoretical limits of the method. Bottom left: reconstructed image based on our Count scheme (addition of noise). Bottom right: reconstructed image based on the Traditional scheme.

shows the reconstructed image using the Click scheme, no noise added in this simulation. This provides the theoretical limit we can reach. To make the simulation more realistic, random Gaussian noise was later introduced such that the magnitude of noise matches the uncertainties obtained in the experiment (Table 4.1). Fig. 4.10 (bottom left) shows the simulated imaged with the addition of noise. Lastly, Fig. 4.10 (bottom right) shows the simulated image using the Traditional Scheme. Our Click method improves both image clarity and contrast. As discussed in the previous section, the absence of number resolution only produced a modest different between the final results in the Count and Click schemes. For this reason, the simulations of the Click is not shown as it is very similar to the Count scheme reconstructed pictures.

In order to study the effect of the number of detectors in our array, we simulated the noiseless Click scheme for an increasing number of detectors. These results are presented in Fig. 4.11 for different arrays of detectors: first 5×5, then 10×10, 15×15, and 26×26. In the right end, we repeat the original Dory picture for comparison.

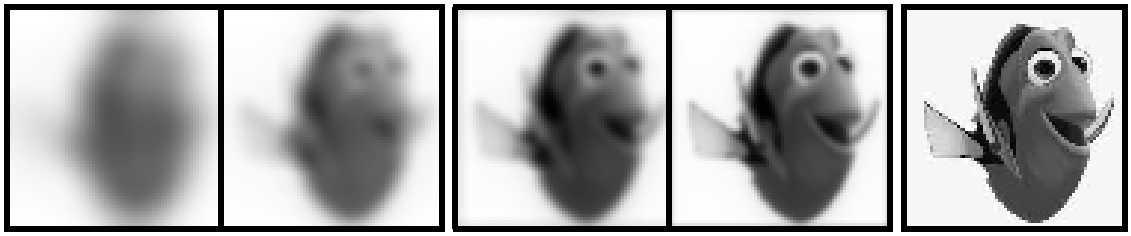

Figure 4.11: Simulated comparison of images reconstructed using arrays of detectors with increasing size. Left: image reconstruction using a 5×5 detector array. Second from left: image reconstruction using a 10×10 detector array. Middle: image reconstruction using a 15×15 detector array. Second from right: image reconstruction using a 26×26 detector array. Right: original image.

4.6 Conclusion

We experimentally demonstrated an optimal imaging method using Transition Edge Sensors, a state-of-the-art photon detector capable of high detection efficiency and accurate number resolution. Our method outperforms the traditional imaging method by an order of magnitude in precision, and the lack of photon-number resolution does not pose a great detrimental effect on measurement precision. Our method improves both image clarity and contrast as shown in the Simulation section.

Our optimal imaging method may find applications in other areas. For example, Astronomy can greatly benefit from this method, in particular, due to the fast convergence to the final value and its optimality in terms of the quantum limits of parameter estimation. This project also highlights the use of Transition Edge Sensors, a kind of photon detector that has a lot more to be explored. The ability to number-resolve the detection of photons can certainly advance quantum metrology [212].

Parts of the following publication (in preparation) have been incorporated as Chapter 5.
R. A. Abrahao, Farid Shahandeh, Martin Ringbauer, Geoff Gillett, L. A. Howard, Till Weinhold, Marcelo P. de Almeida, Timothy C. Ralph and Andrew G. White. *Quantum Correlations beyond Entanglement and Discord*, in preparation, 2020.

Contributions to article *Quantum Correlations beyond Entanglement and Discord* (in preparation): This project was conceived by F. Shahandeh, M. Ringbauer and R. A. Abrahao. The design and construction of experiment was done by R. A. Abrahao with assistance from T. Weinhold and M. P. de Almeida. Data acquisition was conducted by R. A. Abrahao. The codes for running the number-resolving detectors were developed by G. G. Gillett and L. A. Howard. The theory for this article was developed by F. Shahandeh and T. C. Ralph. Data analysis was performed by M. Ringbauer and R. A. Abrahao. This project was supervised by M. Ringbauer and A. G. White.

Chapter 5

Demonstration of a new kind of quantum correlation: quantum JP

The work presented in this chapter is not published in the form of a journal article or pre-print yet. However, I have been the primary researcher in this project, and I will be the first author in the upcoming article. Parts of this work were presented in the Australian and New Zealand Conference on Optics and Photonics (ANZCOP) 2017 in Queenstown, New Zealand, and in the proceedings of Frontiers in Optics 2018 Washington, DC, United States of America [4].

5.1 A new kind of quantum correlation: a quick introduction

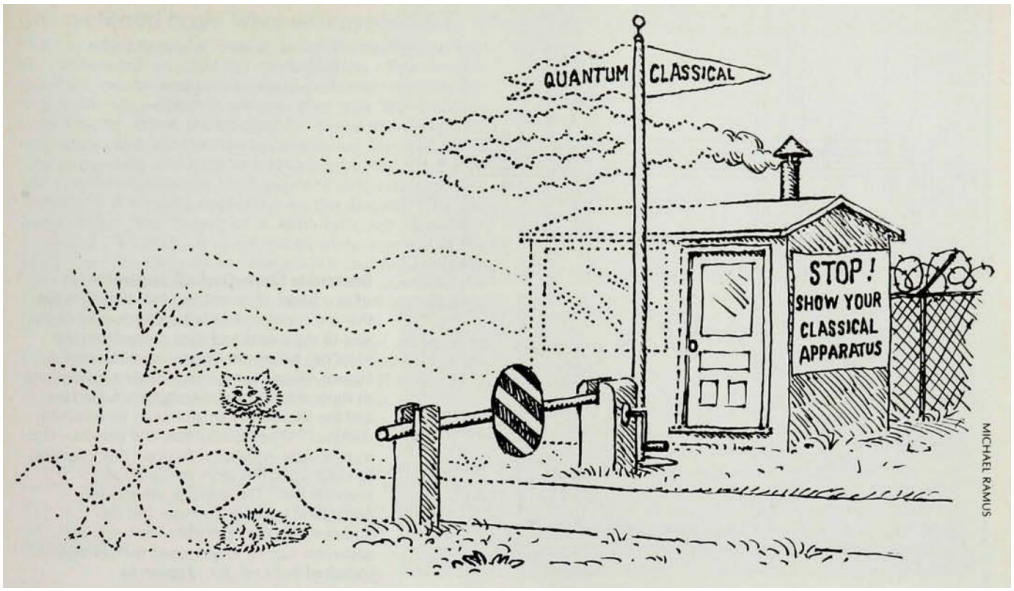

Figure 5.1: The Classical-Quantum Border. Where does classical physics end? And where does quantum physics start? Credit of Image: [213].

Correlation between observed results, either spacelike or timelike separated, are ways to confront classical and quantum theory, and possibly investigate new physics beyond the quantum mechanical

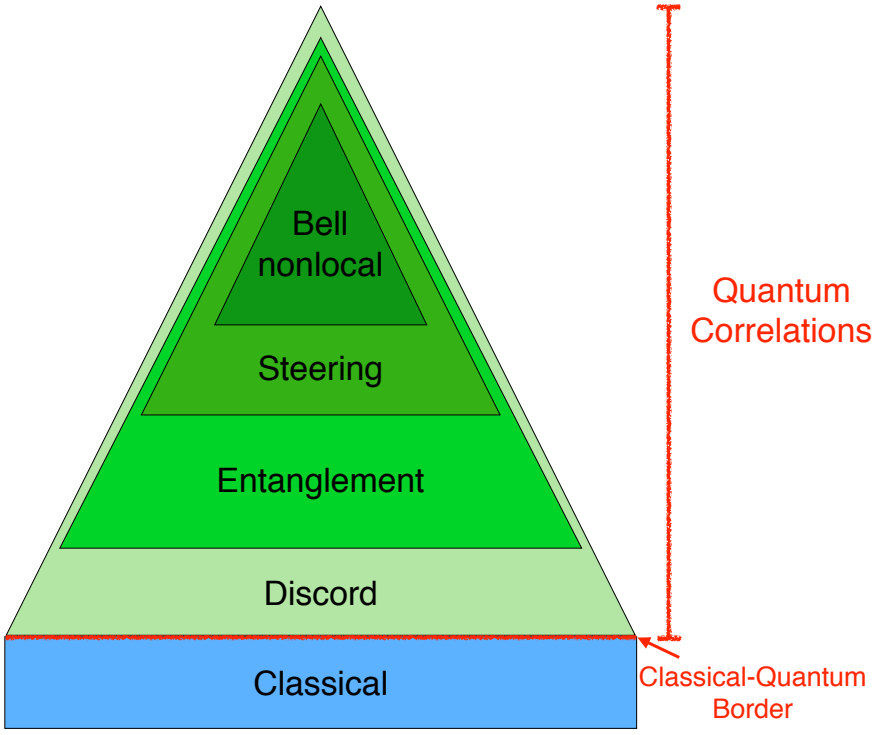

Figure 5.2: Quantum Correlations schematics: the well established status, adapted from [220]. Quantum entanglement is discussed in Section 5.4, Bell nonlocality in Section 5.5, and quantum discord in Section 5.6.

description as well as the boundary between the classical and quantum theories. For instance, quantum correlations of entangled quantum systems are stronger than any classical correlations and found applications in quantum computing, communication and cryptography. Entangled states, i.e. non-separable states, were thought to be the border between classical and quantum physics, however the discovery of quantum discord showed separability is an insufficient criterion [214, 215]. Quantum discord is an information-theoretical approach to the disturbance caused by measurement and also found its applications, especially in simplifying quantum information processing protocols [216]. Quantum discord was thought to capture all nonclassical correlations, then, interestingly, one finds that there is still nonclassical correlation beyond discord. It has been predicted that nonclassical correlations can be observed in the absence of entanglement and of quantum discord [217–219]. Here we aim to demonstrate this new kind of quantum correlation using number-correlated states shared between two agents, named Alice and Bob, which locally look classical, but globally contain correlations beyond classical description. We will discuss our experimental progress.

5.2 Background: Correlations

Correlated systems contain more information globally than just their constituent (individual) parts. For example, the sides of a coin are correlated. If one flips a coin and obtain the result *heads* up, then necessarily the *tails* faces down. So, if one obtains the information about the face up, one can be assured of what is the face down. This is an example of classically correlated results.

5.3 Introduction to Quantum Correlations

Quantum correlations refer to the concept that results measured in quantum systems can be correlated. Considering the well established correlations, we currently understand quantum correlations as schematized in Figure 5.2. Note that Fig. 5.2 depicts the hierarchy of quantum correlations. For a review on the topic of quantum correlations, refer to G. Adesso *et al.* [220].

In the next sections, Bell nonlocality, entanglement, and discord will be discussed in further details. Steering is a kind of quantum correlation outside the scope of this chapter. However, the interested reader may find a vast literature on steering, a subset of them listed here [221–225]. The aim of the present work is to demonstrated a new kind of quantum correlation, named quantum JP, in the absence of entanglement and discord. Thus, the aim of this work is depicted in Figure 5.3.

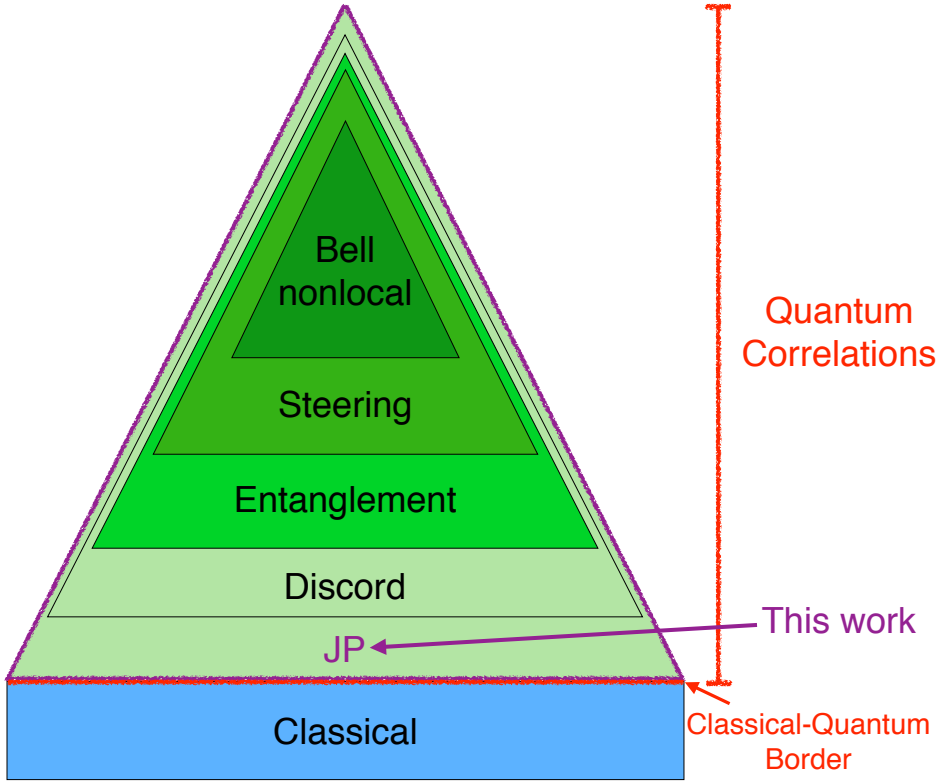

Figure 5.3: Quantum correlations schematics: this work. Here we introduce the quantum JP correlation, which is discussed in Section 5.7.

5.4 Quantum Entanglement

Quantum entanglement was briefly introduced in Chapter 1, in particular how to produce entangled photons from Spontaneous Parametric Down Conversion (SPDC) and quantum dots (QD). The study of quantum entanglement is a rich field, with many unfoldings. For a review on quantum entanglement refer to the work of R. Horodecki *et al.* [66].

As stated in Chapter 1, for pure bipartite states, entanglement can be mathematically formulated as following: $|\Psi_{AB}\rangle \in \mathscr{H}_{AB} = \mathscr{H}_A \otimes \mathscr{H}_B$, where $\mathscr{H}$ is the corresponding Hilbert space. If $|\Psi_{AB}\rangle$ can be

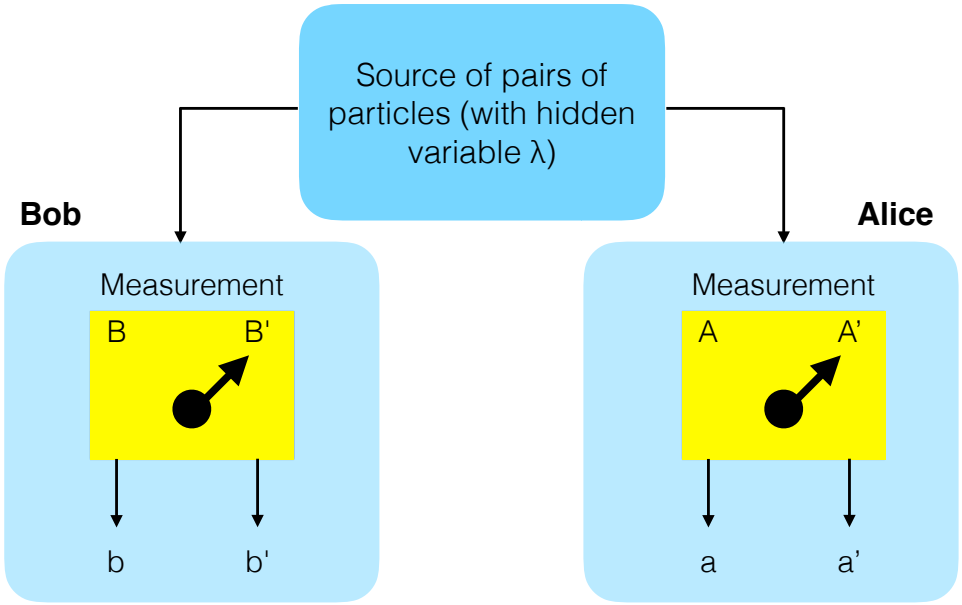

Figure 5.4: Bell's Test. Consider a source of pairs of particles such that one particle goes to Alice, the other goes to Bob. Alice can decide to measure one of two observables, A and A', that result in a and a'. Likewise, Bob can decide to measure one of two observables, B and B', that result in b and b'.

decomposed as the product of two vectors subsystems, then $|\Psi_{AB}\rangle$ is called a product state and there is no entanglement, $|\Psi_{AB}\rangle = |\phi_a\rangle\,|\psi_B\rangle$. On the other hand, $|\Psi_{AB}\rangle$ is entangled if it cannot be written as a separable state, i.e., a convex combination of product states. In our example, if $|\Psi_{AB}\rangle$ is an entangled state, then $|\Psi_{AB}\rangle \neq |\phi_a\rangle\,|\psi_B\rangle$. The key point to remember is that separability is the criterion used to mathematically define entanglement.

5.5 Bell's Test and the Clauser-Horne-Shimony-Holt (CSHS) Inequality

In this section, we introduce the Bell's Test [226, 227] through the CHSH Inequality [228]. This leads to the kind of quantum correlation labeled Bell nonlocal in Fig. 5.2 [229, 230]. In order to better understand Bell nonlocality, we will present the CHSH inequality, whose derivation presented here follows the steps of Y. Aharonov and D. Rohrlich [231].

Consider a source of pairs of particles such that one particle goes to Alice, the other goes to Bob, as in Fig 5.4. Alice can decide to measure one of two observables, A and A', that result in a and a'. Likewise, Bob can decide to measure one of two observables, B and B', that result in b and b'. Let λ be a local hidden variable accessible to each particle, and $p(\lambda)$ be the probability that the particle carries the information about the local hidden variable λ. One can interpret the local hidden variable λ as a local list of the properties of the particle pair. The probability normalization condition imposes:

$$\int_{\lambda} p(\lambda) d\lambda = 1. \tag{5.1}$$

Let us define:

- $P(a|A,\lambda)$: the probability that a measurement performed by Alice of the observable A results in the outcome a, for a given λ;
- $P(b|B,\lambda)$: the probability that a measurement performed by Bob of the observable B results in the outcome b, for a given λ;
- $P(a,b|A,B,\lambda)$: the probability that a measurement performed by Alice of the observable A results in the outcome a, and a measurement performed by Bob of the observable B results in the outcome b, for a given λ;

Classically, as a consequence of Bayes's Theorem and assuming that factorization is permitted, one expects:

$$P(a,b|A,B,\lambda) = P(a|A,\lambda)P(b|B,\lambda). \tag{5.2}$$

Equation 5.2 is based on a few assumptions: (i) free choice, i.e. Alice and Bob are free to choose which respective observable to measure; (ii) locality, i.e. local outcomes do not depend on remote actions; (iii) outcome independence, i.e. local outcomes do not depend on remote outcomes. Furthermore, weighting on $p(\lambda)$, the final probability that a measurement performed by Alice of the observable A results in the outcome a, and a measurement performed by Bob of the observable B results in the outcome b, is given by:

$$P(a,b|A,B) = \int_{\lambda} P(a,b|A,B,\lambda)d\lambda. \tag{5.3}$$

We will define a correlation function C such that:

$$C(A,B) = \sum_i \sum_j a_i b_j P(a_i,b_j|A,B), \tag{5.4}$$

where each a_i and b_j are the possible outcomes (results) of measurement on variables A and B. We will restrict ourselves to the case when the measurement outcome has two possibilities, say +1 and -1. This is a perfect map to the situation of H and V polarizations, or spin up and down. This allows us to write:

$$a_i \in \{+1,-1\}, \tag{5.5}$$

$$b_j \in \{+1,-1\}. \tag{5.6}$$

Now, let us introduce another correlation function in terms of the observables A, A', B and B', such that:

$$\sum_i \sum_j \Big[a_i b_j P(a_i|A,\lambda)P(b_j|B,\lambda) + a_i b'_j P(a_i|A,\lambda)P(b'_j|B',\lambda) + a'_i b_j P(a'_i|A',\lambda)P(b_j|B,\lambda) - a'_i b'_j P(a'_i|A',\lambda)P(b'_j|B',\lambda)\Big]. \tag{5.7}$$

Rewriting it, we obtain:

$$\sum_i \sum_j \Big[a_i P(a_i|A,\lambda)[b_j P(b_j|B,\lambda) + b'_j P(b'_j|B',\lambda)] + a'_i P(a'_i|A',\lambda)[b_j P(b_j|B,\lambda) - b'_j P(b'_j|B',\lambda)]\Big] \tag{5.8}$$

We will use Eq. 5.8 in a moment. Note one important property. Due to probability normalization, we have $\sum_i P(a_i|A,\lambda) = 1$. Combining it with the mathematical statements 5.5 and 5.6, we obtain:

$$\left|\sum_i a_i P(a_i|A,\lambda)\right| \leq 1. \tag{5.9}$$

Likewise,

$$\left|\sum_i a'_i P(a'_i|A',\lambda)\right| \leq 1 \tag{5.10}$$

$$\left|\sum_j b_j P(b_j|B,\lambda)\right| \leq 1 \tag{5.11}$$

$$\left|\sum_j b'_j P(b'_j|B',\lambda)\right| \leq 1. \tag{5.12}$$

Consequently,

$$\left|\sum_i\sum_j a_i b_j P(a_i|A,\lambda)P(b_j|B,\lambda)\right| = \left|\sum_i a_i P(a_i|A,\lambda)\right|\left|\sum_j b_j P(b_j|B,\lambda)\right| \leq 1. \tag{5.13}$$

Thus, the absolute value of each line of Equation 5.8 is upper bounded by 2. Interestingly, as pointed out by Aharonov and Rohrlich [231], the sum of the absolute value of each line of Equation 5.8 is also upper bounded by 2. One way to see this result is to consider the maximum case when:

$$\sum_j [b_j P(b_j|B,\lambda) + b'_j P(b'_j|B',\lambda)] = 2. \tag{5.14}$$

Then,

$$\sum_j [b_j P(b_j|B,\lambda) - b'_j P(b'_j|B',\lambda)] = 0. \tag{5.15}$$

This leads to the conclusion that the absolute value of of Equation 5.8 is upper bounded by 2. Since Eq. 5.8 is just a rewriting of Eq. 5.7, we obtain:

$$\begin{aligned} -2 \leq \sum_i\sum_j \Big[& a_i b_j P(a_i|A,\lambda)P(b_j|B,\lambda) + a_i b'_j P(a_i|A,\lambda)P(b'_j|B',\lambda) + \\ & a'_i b_j P(a'_i|A',\lambda)P(b_j|B,\lambda) - a'_i b'_j P(a'_i|A',\lambda)P(b'_j|B',\lambda)\Big] \leq 2. \end{aligned} \tag{5.16}$$

Now, we must multiply Eq. 5.16 by $p(\lambda)$ and integrate over λ:

$$\begin{aligned} -2 \leq \sum_i\sum_j \Big[& a_i b_j \int_\lambda P(a_i|A,\lambda)P(b_j|B,\lambda)p(\lambda)d\lambda \\ & + a_i b'_j \int_\lambda P(a_i|A,\lambda)P(b'_j|B',\lambda)p(\lambda)d\lambda \\ & + a'_i b_j \int_\lambda P(a'_i|A',\lambda)P(b_j|B,\lambda)p(\lambda)d\lambda \\ & - a'_i b'_j \int_\lambda P(a'_i|A',\lambda)P(b'_j|B',\lambda)p(\lambda)d\lambda\Big] \leq 2. \end{aligned} \tag{5.17}$$

Using Equations 5.3 and 5.4, we can recognise Eq. 5.17 as:

$$-2 \leq C(A,B) + C(A,B') + C(A',B) - C(A',B') \leq 2 \tag{5.18}$$

$$\left|C(A,B) + C(A,B') + C(A',B) - C(A',B')\right| \leq 2. \text{ (CHSH Inequality)} \tag{5.19}$$

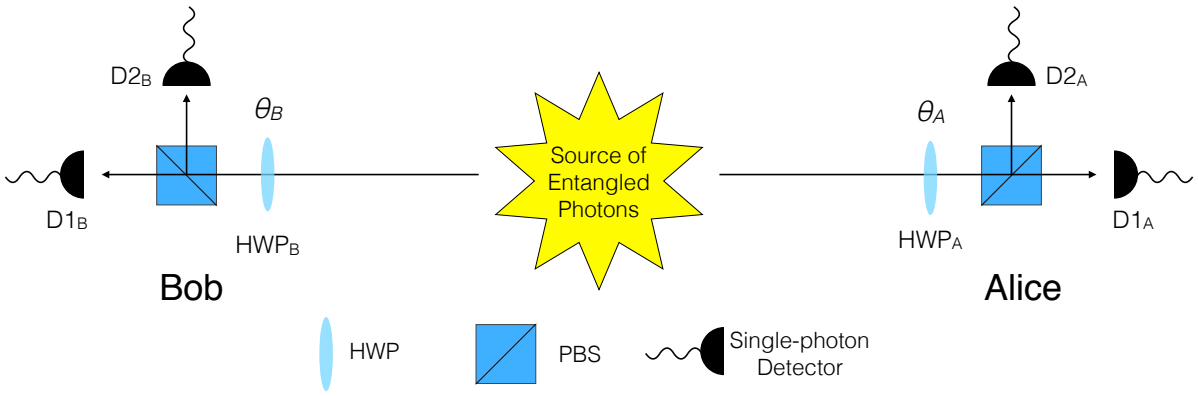

Figure 5.5: Bell's Test: a physical implementation. The Bell's Test start with a source of polarization-entangled photons, one photon going to Alice, the other one going to Bob. In Alice's optical path, there is a half-wave plate HWP θ_A, that realizes Alice's observables A and A' by defining the HWP axis, followed by a polarization beamsplitter (PBS). The detection procedure generates $a = +1$ if a photon is detected in one of the single-photon detectors, say $D1_A$, or $a = -1$ if a photon is detected on the other single-photon detector, $D2_A$. Bob has the same setup in his side.

Equation 5.19 is the Clauser-Horne-Shimony-Holt (CSHS) Inequality. This is also commonly written as:

$$S_{CHSH} = C(A,B) + C(A,B') + C(A',B) - C(A',B') \tag{5.20}$$

$$\left|S_{CHSH}\right| \leq 2. \tag{5.21}$$

The CHSH Inequality is derived from the laws of probability and the principles of classical physics. Therefore, $\left|S_{CHSH}\right| \leq 2$ imposes the upper bound that classical physics could allow under the Bell's Test scenario.

Let us now us turn to a quantum scenario. In Fig. 5.5, the source of pairs of particles is replaced by a source of polarization-entangled photons. In Alice's optical path, there is a half-wave plate HWP θ_A, that realizes Alice's observables A and A' by defining the HWP axis, followed by a polarization beamsplitter (PBS). The detection procedure generates $a = +1$ if a photon is detected in one of the single-photon detectors, say $D1_A$, or $a = -1$ if a photon is detected on the other single-photon detector, $D2_A$. Bob has the same setup in his side. Let us assume that the source produces polarization-entangled photons in the state:

$$|\psi\rangle = \frac{1}{\sqrt{2}}\left(|HH\rangle + |VV\rangle\right). \tag{5.22}$$

Next, we will map the classical expression in Eq. 5.4 to a quantum correlation expression:

$$C_Q(A,B) = \sum_i \sum_j a_i b_j P_Q(a_i, b_j|A,B), \tag{5.23}$$

where $P_Q(a_i, b_j|A,B)$ implies the calculation of probability according to the principles of Quantum Mechanics. Calculating $P_Q(+1,+1|A,B)$, i.e. the probability that Alice and Bob will detect their photons in $D1_A$ and $D1_B$ respectively, and using Malus's Law from Optics, we obtain:

$$P_Q(+1,+1|A,B) = \frac{1}{2}\cos^2(\theta_{AB}), \tag{5.24}$$

where $\theta_{AB} = \theta_A - \theta_B$. Similarly,

$$P_Q(-1,-1|A,B) = \frac{1}{2}\cos^2(\theta_{AB}). \tag{5.25}$$

Using the same reasoning, we also obtain:

$$P_Q(+1,-1|A,B) = P_Q(-1,+1|A,B) = \frac{1}{2}\sin^2(\theta_{AB}). \tag{5.26}$$

Combining these results, the calculation of Eq. 5.23 leads to:

$$\begin{aligned} C_Q(A,B) = (+1)(+1)P_Q(+1,+1|A,B) + (+1)(-1)P_Q(+1,-1|A,B) + \\ (-1)(+1)P_Q(-1,+1|A,B) + (-1)(-1)P_Q(-1,-1|A,B) \end{aligned} \tag{5.27}$$

$$C_Q(A,B) = P_Q(+1,+1|A,B) - P_Q(+1,-1|A,B) - P_Q(-1,+1|A,B) + P_Q(1,-1|A,B) \tag{5.28}$$

$$C_Q(A,B) = \frac{1}{2}\cos^2(\theta_{AB}) - \frac{1}{2}\sin^2(\theta_{AB}) - \frac{1}{2}\sin^2(\theta_{AB})\frac{1}{2} + \frac{1}{2}\cos^2(\theta_{AB}) \tag{5.29}$$

$$C_Q(A,B) = \cos^2(\theta_{AB}) - \sin^2(\theta_{AB}) \tag{5.30}$$

$$C_Q(A,B) = \cos(2\theta_{AB}). \tag{5.31}$$

Similar procedure allow us to calculate $C_Q(A,B')$, $C_Q(A',B)$, and $C_Q(A',B')$.

Consider the particular case where the axis of the half-wave plates (HWP) are set as shown in Fig. 5.6. For this configuration, we come to the following results:

$$C_Q(A,B) = C_Q(A',B) = C_Q(A,B') = \cos\left(2\frac{\pi}{8}\right) = \frac{\sqrt{2}}{2}, \tag{5.32}$$

and

$$C_Q(A',B') = \cos\left(2\frac{3\pi}{8}\right) = -\frac{\sqrt{2}}{2}. \tag{5.33}$$

Thus,

$$S_Q = C_Q(A,B) + C_Q(A,B') + C_Q(A',B) - C_Q(A',B') \tag{5.34}$$

$$S_Q = 2\sqrt{2}\,, \tag{5.35}$$

where once again the subindex Q denotes quantum.

The classical upper bound is $S_{CHSH} = 2$, while Quantum Mechanics allows us to obtain a greater upper bound $S_Q = 2\sqrt{2}$, which is significantly different and measurable. Values of S greater than 2 are called violations of Bell's inequality. The quantum mechanical upper bound $S_Q = 2\sqrt{2}$ is named Tsirelson's bound [232].

What makes it so interesting is that Bell's Test provides a clear way to test quantum nonlocality. This leads to the consequence that no local hidden variable model can explain the result of a Bell's violation. To be assured of the nonlocality, the Bell's Test must be performed such that Alice and Bob are spacelike separated [233].

Bell's Test and the CHSH Inequality have been experimentally tested extensively: from the seminal test by Freedman and Clauser [234], through the series of experiments by A. Aspect and

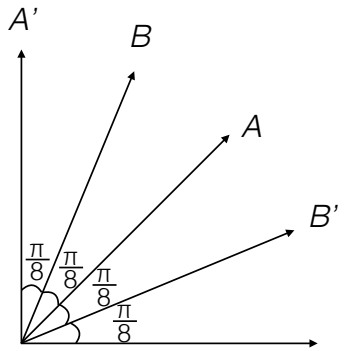

Figure 5.6: Half-wave plates (HWP) settings for a maximum violation of a Bell's Test using the CHSH inequality.

colleagues [235–237], to the loophole-free Bell's Tests [238–240]. Yet, the Bell's Tests cited here are just a subset of the rich list of experimental works on this topic.

Additionally, let us highlight two particular Bell's Tests of interest. One is, to the best of my knowledge, the closest ever recorded to the Tsirelson's bound [241], achieving $S_Q = 2.82759 \pm 0.00051$. The value of $2\sqrt{2}$ truncated to 5 decimal places is 2.82842. Second, one could attempt to explain the violation of a Bell's Test by allowing some kind of superluminal communication between Alice and Bob, not mentioning the nature of this communication. Experiments were performed to put bounds on the speed of this superluminal communication. The work of Salart *et al.* [242] found that "the speed of the influence would have to exceed that of light by at least four orders of magnitude".

The concepts of quantum correlations found many applications in a wide range of areas. To cite a few examples: quantum computation [243, 244], quantum cryptography [245, 246], quantum metrology [191], and quantum teleportation [247].

5.6 Quantum Discord

There is a kind of correlation that is neither entanglement, nor classical and this is quantum discord. That was the understanding of the Quantum Physics community prior to the work of E. Agudelo *et al.* [217]. Quantum discord is defined in terms of mutual information, a concept from Information Theory. Before we delve into its definition, let us briefly introduce some key concepts of Information Theory [248].

5.6.1 Classical Information Theory: Entropy and Mutual Information

In this subsection we will use the notation of Cover *et. al* [248].

Entropy

Consider X a discrete random variable with an alphabet of $\mathbb{X}$. The probability density function for the random variable X to assume the particular value x is given $p(x) = Pr\{X = x\}$ for $x \in \mathbb{X}$. The **entropy**

$H(X)$ of a random variable X is defined as:

$$H(X) = -\sum_{x\in\mathbb{X}} p(x)\log_2 p(x) \text{ (Entropy)}, \tag{5.36}$$

where the base 2 of the logarithm sets the unit of $H(X)$ to bits. The entropy $H(X)$ "measures the uncertainty of a random variable" [248]. In other words, the entropy measures the information content of a random variable. For example, consider the case of a coin. If it is a fair coin, one cannot predict the outcome of a coin toss, with each possible outcome (heads or tails) having 50% chance. In this case, each coin toss reveals 1 bit of information, therefore $H(X) = 1$ bit. However, if the coin is totally unfair, such that a coin toss always gives the same result, then a coin toss would reveal no information as one could always predict the outcome in advance, and therefore, $H(X) = 0$ bits. The non-negativity of probability distributions, i.e. $0 < p(x) \leq 1$, implies that $H(X) \geq 0$ for all X. Equation 5.36 is commonly referred as Shannon Entropy [249].

Joint Entropy and Conditional Entropy

Now consider two discrete random variables X and Y with respective alphabets $\mathbb{X}$ and $\mathbb{Y}$. From Eq. 5.36, one can defined the joint entropy $H(X,Y)$ for the joint probability density function $p(x,y)$ as:

$$H(X,Y) = -\sum_{x\in\mathbb{X}}\sum_{y\in\mathbb{Y}} p(x,y)\log_2 p(x,y) \text{ (Joint Entropy)}. \tag{5.37}$$

As commented by Desurvire [97]: "joint entropy represents the average information derived from joint events occurring from two sources X and Y".

One can define the conditional entropy $H(X|Y)$ such that:

$$H(X|Y) = -\sum_{y\in\mathbb{Y}} p(y)H(x|y) \text{ (Conditional Entropy)}. \tag{5.38}$$

Thus,

$$H(X|Y) = -\sum_{y\in\mathbb{Y}} p(y)\sum_{x\in\mathbb{X}} p(x|y)\log_2 p(x|y). \tag{5.39}$$

Using Bayes's Theorem, $p(x,y) = p(x|y)p(y) = p(y|x)p(x)$. Then,

$$H(X|Y) = -\sum_{y\in\mathbb{Y}}\sum_{x\in\mathbb{X}} p(x,y)\log_2 p(x|y). \tag{5.40}$$

Desurvire [97] comments on the meaning of conditional entropy: "$H(X|Y)$ represents the information we learn from source X, given the information we have from source Y".

Relative Entropy

Consider two $p(x)$ and $q(x)$ probability density functions for the same discrete random variable X with alphabet of $\mathbb{X}$. The **relative entropy** $H(X)$ for the two $p(x)$ and $q(x)$ probability density functions is defined as:

$$D(p||q) = -\sum_{x\in\mathbb{X}} p(x)\log_2\frac{p(x)}{q(x)} \text{ (Relative Entropy)}. \tag{5.41}$$

Note that: (i) If $p(x) = q(x)$, then $D(p||q) = 0$; (ii) If either $p(x)$ or $q(x)$ approaches zero, then $D(p||q) \to \infty$. Therefore the relative entropy evokes a weak sense of distance, and is also called Kullback–Leibler distance.

Mutual Information

Now consider two discrete random variables X and Y with respective alphabets $\mathbb{X}$ and $\mathbb{Y}$. Also consider their joint probability density function $p(x,y)$ and the marginal probability density functions $p(x)$ and $p(y)$. The mutual information is defined as the relative entropy between the joint probability density function $p(x,y)$ and the product of the marginal probability density functions $p(x)$ and $p(y)$. Mathematically:

$$I(X;Y) = D(p(x,y)||p(x)p(y)) = \sum_{x\in\mathbb{X}}\sum_{y\in\mathbb{Y}} p(x,y)\log_2\frac{p(x,y)}{p(x)p(y)} \text{ (Mutual Information).} \tag{5.42}$$

Therefore,

$$I(X;Y) = \sum_{x\in\mathbb{X}}\sum_{y\in\mathbb{Y}} p(x,y)\log_2\frac{p(x|y)p(y)}{p(x)p(y)} \tag{5.43}$$

$$= \sum_{x\in\mathbb{X}}\sum_{y\in\mathbb{Y}} p(x,y)\log_2\frac{p(x|y)}{p(x)} \tag{5.44}$$

$$= \sum_{x\in\mathbb{X}}\sum_{y\in\mathbb{Y}} p(x,y)\log_2 p(x|y) - \sum_{x\in\mathbb{X}}\sum_{y\in\mathbb{Y}} p(x,y)\log_2 p(x) \tag{5.45}$$

$$= -\sum_{x\in\mathbb{X}}\sum_{y\in\mathbb{Y}} p(x,y)\log_2 p(x) - \left(-\sum_{x\in\mathbb{X}}\sum_{y\in\mathbb{Y}} p(x,y)\log_2 p(x|y)\right) \tag{5.46}$$

$$= -\sum_{x\in\mathbb{X}} p(x)\log_2 p(x) - \left(-\sum_{x\in\mathbb{X}}\sum_{y\in\mathbb{Y}} p(x,y)\log_2 p(x|y)\right) \tag{5.47}$$

$$= H(X) - H(X|Y). \tag{5.48}$$

Once again, Desuvire explains the meaning: "mutual information is the reduction of uncertainty in X that we get from the knowledge of Y".

From the above definitions, we have the following properties:

$$I(X;Y) = H(X) - H(X|Y) \tag{5.49}$$

$$I(X;Y) = H(Y) - H(Y|X) \tag{5.50}$$

$$I(X;Y) = H(X) + H(Y) - H(X,Y) \tag{5.51}$$

$$I(X;Y) = I(Y;X) \tag{5.52}$$

Note that these properties are all based on classical information theory and equivalent. In other words, the subtraction between any two of Equations 5.49, 5.50, and 5.51 necessarily results in zero. Additionally, these properties can be visualised with the aid of a Venn Diagram, Fig. 5.7.

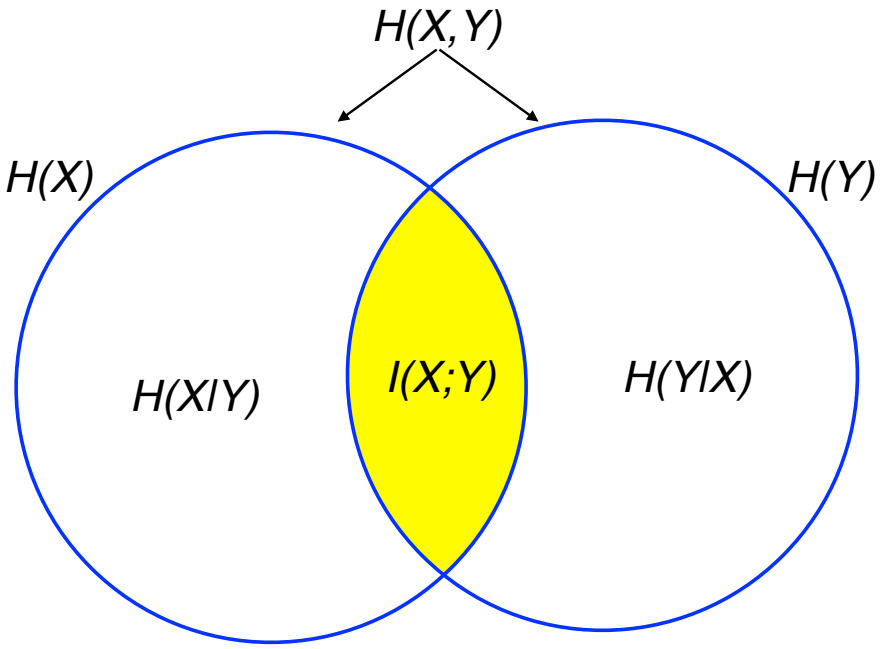

Figure 5.7: Venn diagram for Mutual Information. The properties of mutual information, mathematically Equations 5.49, 5.50, and 5.51, can be visualised in this Venn Diagram. The yellow region represents the mutual information $I(X,Y)$. Credit of Imagine: [248].

5.6.2 The quantum counterpart: quantum mutual information

Taking a closer look at the equations of mutual information in terms of entropy (Equations 5.49, 5.50, and 5.51), one may ask what are the quantum counterparts of these equations. This will lead us to the concept of quantum discord, as discovered independently by H. Ollivier and W. H. Zurek [214] and L. Henderson and V. Vedral [215]. In this subsection, we will introduce discord as originally presented by Ollivier and Zurek [214] and use their notation for the equations involving the quantum elements.

Consider a bipartite quantum system S, described by a density matrix ρ. Information about the system S is obtained through apparatus $\mathcal{A}$[1]. In Quantum Information Theory, the Shannon Entropy (Eq. 5.36) is mapped into the von Neumann entropy.

$$H(S) = H(\rho_S) = -\mathrm{Tr}_S \rho_S \log_2 \rho_S \text{ (von Neumann Entropy).} \tag{5.53}$$

Next, we focus on Eq. 5.51. The classical random variables X and Y are replaced by variables representing the quantum system S and the apparatus $\mathcal{A}$. Thus,

$$I_Q(S;A) = H(S) + H(\mathcal{A}) - H(S,\mathcal{A}), \tag{5.54}$$

where the subindex Q is inserted to remind the reader that this is the quantum version of mutual information.

[1] Again, the text here describes quantum discord as originally presented by Ollivier and Zurek [214] in terms of quantum system S and apparatus $\mathcal{A}$. However, discord can also be present between two subsystems of S. In this case, we can look for discord between two subsystems of S, disregarding the apparatus $\mathcal{A}$.

Furthermore, the quantum counterpart of Eq. 5.49 must be derived. However, conditional entropy in quantum information gains a caveat. The conditional entropy $H(S|\mathcal{A})$ of the quantum system S given the state of apparatus $\mathcal{A}$ is not straightforward. As pointed out by Ollivier and Zurek [214]: "the conditional entropy $H(S|\mathcal{A})$ requires us to specify the state of S given the state of $\mathcal{A}$. Such statement in quantum theory is ambiguous until the to-be-measured set of states $\mathcal{A}$ is selected" [2]. To circumvent this problem, the same authors use perfect measurement of apparatus $\mathcal{A}$ by exploring a set of different projection operators $\{\Pi_j^{\mathcal{A}}\}$, where the subindex j represents different outcomes of the measurement process. If the outcome of the measurement is $\Pi_j^{\mathcal{A}}$, then the state of the system S is given by

$$\rho_{S|\Pi_j^{\mathcal{A}}} = \frac{\Pi_j^{\mathcal{A}} \rho_{S,\mathcal{A}} \Pi_j^{\mathcal{A}}}{\mathrm{Tr}_{S,\mathcal{A}} \Pi_j^{\mathcal{A}} \rho_{S,\mathcal{A}}}, \tag{5.55}$$

where the denominator is p_j, the probability of outcome $\Pi_j^{\mathcal{A}}$,

$$p_j = \mathrm{Tr}_{S,\mathcal{A}} \Pi_j^{\mathcal{A}} \rho_{S,\mathcal{A}}. \tag{5.56}$$

Ollivier and Zurek interpret the entropy $H(\rho_{S|\Pi_j^{\mathcal{A}}})$ as "the missing information about S". This leads to the expression of conditional entropy $H\left(S|\{\Pi_j^{\mathcal{A}}\}\right)$ dependent on the complete set of measurements $\{\Pi_j^{\mathcal{A}}\}$ as:

$$H\left(S|\{\Pi_j^{\mathcal{A}}\}\right) = \sum_j p_j H\left(\rho_{S|\Pi_j^{\mathcal{A}}}\right), \tag{5.57}$$

where the weighted probabilities p_j are explicit in Eq. 5.56.

Finally, we are in the position to write the quantum counterpart of Eq. 5.49. Doing so, the quantum mutual information is:

$$J_Q(S;\mathcal{A})_{\{\Pi_j^{\mathcal{A}}\}} = H(S) - H\left(S|\{\Pi_j^{\mathcal{A}}\}\right). \tag{5.58}$$

To avoid confusion, we used the letter J instead of I, and the subindex Q as a reminder that it refers to the quantum regime.

The difference between quantum mutual information defined as $I_Q(S;\mathcal{A})$ (Eq. 5.54) and as $J_Q(S;\mathcal{A})_{\{\Pi_j^{\mathcal{A}}\}}$ (Eq. 5.58) is the definition of *Quantum Discord*. Mathematically,

$$\delta(S;\mathcal{A})_{\{\Pi_j^{\mathcal{A}}\}} = I_Q(S;\mathcal{A}) - J_Q(S;\mathcal{A})_{\{\Pi_j^{\mathcal{A}}\}} \text{ (Quantum Discord)} \tag{5.59}$$

$$= H(\mathcal{A}) - H(S,\mathcal{A}) + H\left(S|\{\Pi_j^{\mathcal{A}}\}\right). \tag{5.60}$$

Note that $\delta(S;\mathcal{A})_{\{\Pi_j^{\mathcal{A}}\}}$ is not necessarily zero. This is a contrast when compared with the classical equations. For classical mutual information (Equations 5.49 and 5.51), one always obtains:

$$\Delta = \underbrace{I(X;Y)}_{\text{Eq. 5.51}} - \underbrace{I(X;Y)}_{\text{Eq. 5.49}} = 0. \tag{5.61}$$

For convenience, we will repeat the main mathematical results about quantum discord on Table 5.1.

[2] In general, discord can be understood purely as a measure of correlation, without the need to subscribe to any particular interpretation of Quantum Mechanics or quantum measurement theory. In this broader context, the conditional entropy would relate to two subsystem of S, say $H(S_1|S_2)$.

Classical	Quantum
$H(X) = -\sum_{x\in\mathbb{X}} p(x)\log_2 p(x)$	$H(S) = -\mathrm{Tr}_S \rho_S \log_2 \rho_S$
$I_1(X;Y) = H(X)+H(Y)-H(X,Y)$	$I_Q(S;\mathcal{A}) = H(S)+H(\mathcal{A})-H(S,\mathcal{A})$
$I_2(X;Y) = H(X)-H(X\|Y)$	$J_Q = H(S)-H\left(S\|\{\Pi_j^{\mathcal{A}}\}\right)$
$\Delta = I_1 - I_2 = 0$	$\delta(S;\mathcal{A})_{\{\Pi_j^{\mathcal{A}}\}}$ (Quantum Discord) $=I_Q(S;\mathcal{A}) - J_Q(S;\mathcal{A})_{\{\Pi_j^{\mathcal{A}}\}}$ $= H(\mathcal{A}) - H(S,\mathcal{A}) + H\left(S\|\{\Pi_j^{\mathcal{A}}\}\right) \neq 0$

Table 5.1: Equations for Quantum Discord.

Putting into words, quantum discord is a kind of quantum correlation based on an information theoretic approach to the disturbance caused by a measurement in a quantum scenario. In their seminal paper, Ollivier and Zurek [214] noted that it is possible to obtain quantum discord in a bipartite quantum system, even in the absence of quantum entanglement. This can be observed in an example. Consider a Werner state [250] such as:

$$W = \frac{1-z}{4}\mathbf{1} + z\left|\psi\right\rangle\left\langle\psi\right|, \tag{5.62}$$

where $\left|\psi\right\rangle$ is an entangled state

$$\left|\psi\right\rangle = \frac{\left|00\right\rangle + \left|11\right\rangle}{\sqrt{2}}. \tag{5.63}$$

As commented by Ollivier and Zurek [214]: "It can be seen that discord is greater than 0 in any basis when $z > 0$, which contrasts with the well-known separability of such states when $z < \frac{1}{3}$".

The consequence of quantum discord is that separability, the criterion used for defining quantum entanglement, cannot be used as the criterion for nonclassicality.

Since its first introduction [214, 215], the study of quantum discord expanded to other areas, such as quantum computation [251, 252]. It is noteworthy the works of M. Gu *et al.* [253] and Dakić *et al.* [216] providing operational significance of discord.

5.7 Quantum JP

In 2013, a new theoretical result expanded our knowledge of quantum correlations. Up to that moment, Bell nonlocality, steering, entanglement and discord were all known quantum correlations. From this list, discord was thought to contain every form of quantum correlation. That was changed with the work of E. Agudelo, J. Sperling, and W. Vogel [217]. The work of this thesis chapter aims to demonstrate this new kind of quantum correlation predicted by E. Agudelo *et al.* [217].

5.7.1 Quantum JP: Theory

In the article *Quasiprobabilities for multipartite quantum correlations of light* by E. Agudelo *et al.* [217], the authors use the formalism of quasiprobability distributions in Quantum Optics to study bipartite correlated systems.

Quasiprobability distributions

At this point, it is instructional to briefly discuss quasiprobability distributions, and so we will. More detailed discussions on quasiprobability distributions can be found in References [13, 14, 69, 169, 254].

Consider a phase space $W(q,p)$ distribution, for variables p momentum and q position, obeying the quantum mechanical commutation relation. $W(q,p)$ is called Wigner distribution. The $W(q,p)$ distribution correctly predicts the outcomes of measurements on a continuous-variable quantum system, and p and q are particular outcomes. The position p is given by the marginal distribution of $W(q,p)$ such that $p = \int_{-\infty}^{+\infty} W(q,p)dp$. In the same way, the momentum q is given by the marginal distribution $q = \int_{-\infty}^{+\infty} W(q,p)dq$. The Wigner $W(q,p)$ distribution for the density operator $\hat{\rho}$ is then:

$$W_\rho(q,p) = \frac{1}{\pi}\int_{-\infty}^{+\infty} \langle q-x|\,\rho\,|q+x\rangle\, e^{2ipx}dx \text{ (Wigner's distribution).} \tag{5.64}$$

When one considers some quantum mechanical states written as quantum superposition, such as Fock states or Schrödinger's cat states, one important distinction happens: the phase space $W(q,p)$ distribution can present regions where it is negative, thus it violates the axiom that probabilities are non-negative. This is a consequence of the quantum interference of the constituent quantum superposition. Due to this negative regions, $W(q,p)$ is called a quasipropability distribution. The negativity regions in $W(q,p)$ are a clear indication of nonclassical behavior [169].

Furthermore, the Wigner $W(q,p)$ distribution can be generalized to s-parameterized quasiprobability distributions, where s refers to the order of operators. For $s=0$, we obtain the Wigner $W(q,p)$ quasipropability as in Eq. 5.64. For $s=-1$, we obtain the Husimi Distribution (a.k.a Q distribution). For $s=+1$, we obtain the Glauber–Sudarshan distribution (a.k.a P distribution) [25, 255, 256].

The Husimi Distribution is particularly appealing as it is directly what one obtains from a homodyne detection. It is the convolution of the Wigner $W(q,p)$ distribution with a vacuum Gaussian distribution. Mathematically [169]:

$$Q(q,p) = \frac{1}{\pi}\int_{-\infty}^{+\infty}\int_{-\infty}^{+\infty} W(q',p')e^{-(q-q')^2-(p-p')^2}dq'dp'. \tag{5.65}$$

One important property of the Q distribution is that it obeys the axiom of non-negativity of probability. Therefore, Q distribution is a proper probability distribution.

The Glauber–Sudarshan (P) distribution comes from the normal ordering of operators. Mathematically [169]:

$$W(q,p) = \frac{1}{\pi}\int_{-\infty}^{+\infty}\int_{-\infty}^{+\infty} P(q_o,p_o)e^{-(q-q_o)^2-(p-p_o)^2}dq_o dp_o. \tag{5.66}$$

The P distribution "diogonalizes the density operator in terms of coherent states" [169]. So for a coherent state, in Fock basis, one obtains

$$|\alpha\rangle = e^{-\frac{1}{2}|\alpha|^2}\sum_{n=0}^{\infty}\frac{\alpha^n}{\sqrt{n!}}|n\rangle, \tag{5.67}$$

such that

$$\alpha = \frac{1}{\sqrt{2}}(q_o + ip_o). \tag{5.68}$$

Then, the density operator is given by [169]:

$$\hat{\rho} = \int_{-\infty}^{+\infty} \int_{-\infty}^{+\infty} P(q_o, p_o) \left|\alpha\right\rangle \left\langle\alpha\right| dq_o dp_o. \tag{5.69}$$

As commented by U. Leonhardt [169], Eq. 5.69 seems to suggest that we are representing a quantum state as a distribution of coherent states, equivalently as a statistical mixture of classical amplitudes. So, it then follows that, unless $|\psi\rangle$ is a coherent state, it is not possible to represent a pure state $|\psi\rangle$ simply as the statistical mixture of coherent states. Eq. 5.69 simply shows that states that conflict with it are nonclassical states, that is, their P distribution will have regions of negative value, what consequently leads it to be called a quasipropability distribution (violation of the axiom of non-negativity of probability).

Both P distribution and Wigner $W(q,p)$ distribution can present negative regions on the phase space. And the negativity regions on the phase space of the P distribution and Wigner $W(q,p)$ distribution are signatures of nonclassicality.

Let us make it clear that Eq. 5.66 and Eq. 5.69 do not suggest that the P distribution does not exists for the quantum states. Coherent states will present positive P distributions, while other pure quantum states will still have a P distribution, but it will present negative regions or singularity (in the sense of Dirac's delta).

The work of E. Agudelo *et al.* [217]

Let us now analyse the work of E. Agudelo *et al.* [217]. In attempting to generalize the P distribution for multimode light, E. Agudelo *et al.* [217] considered the case of equally squeezed states in orthogonal quadratures in the input ports of a 50:50 beamsplitter. In the output ports of the balanced beamsplitter, one obtains a two-mode squeezed-vacuum state. This output state presents quantum entanglement and quantum discord.

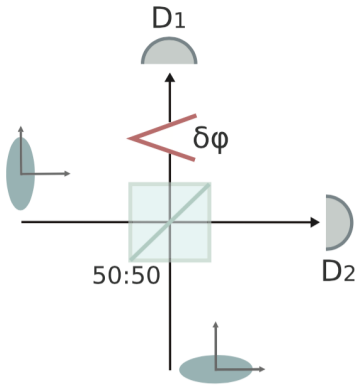

Figure 5.8: Consider the case of equally squeezed states in orthogonal quadratures in the input ports of a 50:50 beamsplitter. After phase-randomization in one of the outputs of the 50:50 beamsplitter, the output state is given by Eq. 5.70. Credit of Imagine: [217].

The authors then add a phase randomization in one of the outputs of the 50:50 beamsplitter, as depicted in Figure 5.8. This procedure leads to the state:

$$\hat{\rho} = \sum_{n=0}^{\infty} (1-\chi)\chi^2 \left|n\right\rangle \left\langle n\right| \otimes \left|n\right\rangle \left\langle n\right|, \tag{5.70}$$

where χ is the squeezing parameter of the initial fields, obeying $0 < \chi < 1$. Note that the state in Eq. 5.70 is a convex mixture of product states $\left|n\right\rangle \left\langle n\right| \otimes \left|n\right\rangle \left\langle n\right|$ what indicates absence of quantum entanglement. Based on the work of A. Datta [257], the authors use the criterion of orthogonality of the Fock states, i.e. $\langle n|n'\rangle = \delta_{Dirac}$, to argue that the state in Eq. 5.70 also presents no quantum discord.

The authors [217] then move to study the state in Eq. 5.70 using the formalism of quasiprobability distribution. For the Wigner distribution, the state obeys the non-negativity. However, when the authors turn to the P distribution, the situation changes significantly. The P distribution shows areas of negativity, indicating a clear nonclassical signature.

Simulating a homodyne detection scheme, the authors [217] plot the result for the P distribution. For this propose, one must consider a w width parameter, working as a filtering function, such that when $w \to \infty$, then $P(\alpha, w) \to P(\alpha)$. For the particular values of $\chi = 0.8$ and $w = 1.5$, the corresponding P function is shown in Figure 5.9.

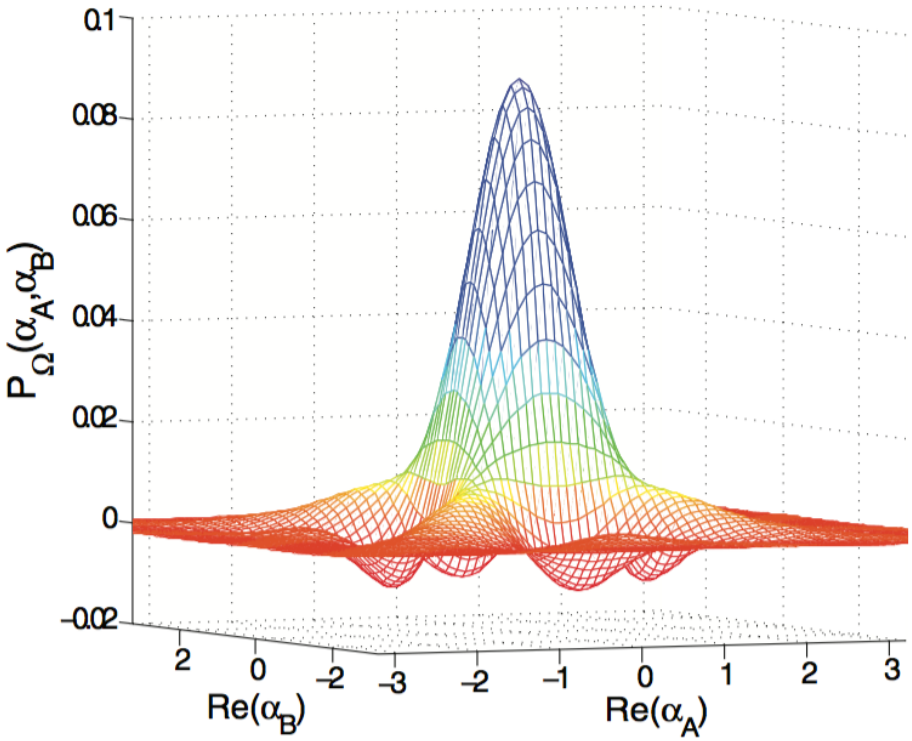

Figure 5.9: Theoretical joint P distribution obtained by simulating a homodyne detection with particular values of squeezing parameter $\chi = 0.8$ and width parameter $w = 1.5$. Credit of imagine: [217].

Agudelo *et al.* [217] summarise their work in the following way: "we have introduced an experimentally realizable quantum state with the following properties: (1) no entanglement; (2) zero

quantum discord; (3) classical reduced single-mode states; (4) non-negative Wigner function". Yet, this state presents clear quantum correlations effects.

Note that this quantum correlation is manifested in the *joint P distribution*, hence the name *quantum JP*[3]. In other words, for Alice and Bob individually the state looks classical. However, the joint P distribution for both Alice and Bob, present areas of negativities, indicating its quantum nature.

5.7.2 Quantum JP: Experiment

The next question is how to experimentally demonstrate the result uncovered by Agudelo *et al.* [217]. Taking a look on Eq. 5.70, this state can be experimentally produced from Spontaneous Parametric Down Conversion (SPDC) if the down-converted photons are not entangled and phase-randomised. For convenience, we will repeat the equation for the quantum state obtained from SPDC in Fock basis as introduced in Chapter 1 (Eq. 5.71).

$$|\psi\rangle_{SPDC} = \sqrt{1-\chi^2}\sum_{n=0}^{\infty}\chi^n|n_1n_2\rangle = c_0|00\rangle + c_1|11\rangle + c_2|22\rangle + c_3|33\rangle + \cdots, \tag{5.71}$$

The higher order terms in SPDC are usually perceived as a problem, as they introduce errors in most quantum information processing protocols, because the typical single-photon detector cannot number-resolve them. For the same reason, they cause a rise in the value of $g^{(2)}(0)$ and are avoided by decreasing the power of the pump laser in the SPDC process. Here, in this project, we do exactly the opposite: we want to produce the higher order terms in a SPDC process. We used Transition Edge Sensors, the same used in Chapter 4 and explained in Appendix A, to number-resolve the detection of the down-converted photons. For our project, we look at the higher order terms in SPDC not as villains, but as heroes.

Experimental Setup

The schematics for the experimental setup can be found in Fig 5.10. We will comment each part.

Laser

Our experiments starts with a Coherent Mira High Power Laser. This is a 150 fs Ti:Sapphire laser operating at $\lambda = 820$ nm, mode-locked, pulsing at 76 MHz.

Pulse Picking

The Pulse Picking System consists of a confocal lens system, a stage of polarization control, a Rubidium Titanyl Phosphate (RTP) Leysop Pockels Cell, and polarization-controlled pulse-rejection system achieved using a high-power polarization beamsplitter (PBS). The insertion of this Pulse Picking System is necessary due to the recovering time between consecutive detection events on the Transition

[3]This is the name used in this chapter. This new quantum correlation is also called "net global quantum coherence" or "global phase-space nonclassicality" [218, 219].

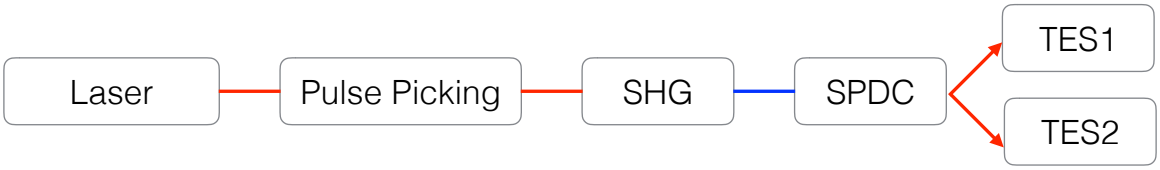

Figure 5.10: Experimental setup. The experiment starts with a $\lambda = 820$ nm mode-locked laser pulsing at 76 MHz. To decrease the pulsing repetition rate to provide a recovery time for the TES detectors, the laser light enters the pulse picking system and exits it at 99 kHz. After that, the light undergoes a Second Harmonic Generation (SHG) process with a BiBO crystal leaving at wavelength 410 nm. This laser light drives a BBO Spontaneous Parametric Down Conversion (SPDC) process whose two output modes are each connected to Transition Edge Sensors (TES1 and TES2).

Edges Sensors (TES1 and TES2). So, before the pulse picking system we have laser pulses at 76 MHz, Fig. 5.11 (a). Once the pulse picking is activated, its output is laser pulses at 99 kHz, Fig 5.11 (b).

Figure 5.11: Pulse Picking System. Fig. 5.11 (a) shows laser light when the Pockels Cell is off. This reveals the laser pulse repetition rate. From this oscilloscope screenshot, we see the 76.11 MHz reader (yellow box). Fig. 5.11 (b) shows laser light when the Pockels Cell is on, causing the laser light to leave the pulse picking system at the rate of 99.06566 kHz (yellow box) for this specific oscilloscope screenshot.

SHG

Next, the laser light enters a Second Harmonic Generation (SHG) process [55]. In this process, one incoming laser with frequency ω_1 is probabilistically converted in a laser with frequency $\omega_2 = 2\omega_1$. Since the frequency is doubled, then the wavelength is halved. So, for our case, the incoming laser with $\lambda = 820$ nm (near infrared) is converted into a laser with $\lambda = 410$ nm (violet). In our setup, we used a 2 mm Bismuth Borate (BiBO) crystal.

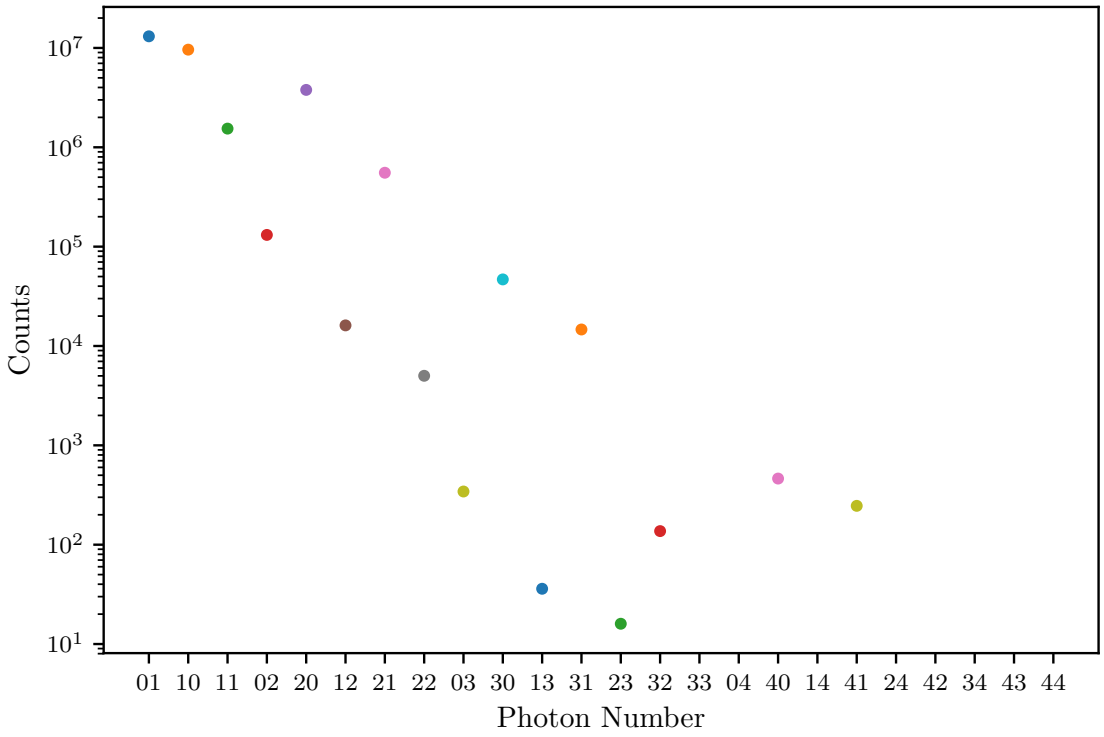

Figure 5.12: SPDC counts for 3 hours of detection. The horizontal axis corresponds to different Fock states. For example, when one reads 01, this means 0 photon in Alice's mode, and 1 photon in Bob's mode.

SPDC

The Spontaneous Parametric Down Conversion (SPDC) process for generation of single photons was already introduced in Chapter 1 and commented throughout this thesis. Here we used a 2 mm Beta-Barium Borate (BBO) crystal [63] in a type-I SPDC. Additionally, we used 5 nm FWHM frequency filters centered at 820 nm. The 2 output modes of the SPDC are collected to single-mode optical fibres and connected to the Transition Edge Sensors TES1 and TES2.

TES1 and TES2

The Transition Edge Sensors (TES1 and TES2) work as number-resolving photon detectors. The operation of Transition Edge Sensors is detailed in Appendix A.

5.7.3 Quantum JP: Data

The first result we will report is the number-resolved detection of the generate SPDC photons. We present of our photon statistics measurement, i.e., the result of our photon counting measurement. See Fig. 5.12. This was obtained directly from the number-resolving TES1 and TES2 detection system for 3 hours of data collection in a single data run. The data processing used for this picture was the photon-number assignment performed by the TES system as detailed in Appendix A.

Our initial intention was to make additional data runs, however the TES system has been unavailable since this data was taken. The asymmetry presented in Figure 5.12 could be explained by asymmetry in optical loss, i.e. Alice's and Bob's arms present different levels of photon loss, or by asymmetry in detection efficiency between TES1 and TES2.

Since the unavailability of the TES system due to a series of technical problems, we were limited to this single dataset. So, instead of making additional runs, we had to learn as much as we could from this dataset. Yet, this still allowed us to show the data analysis and to reach some interesting conclusions. The data presented here is preliminary, and we are working on the verification of this dataset and of the detectors calibration.

The next question is: from the data shown in Fig. 5.12, what can be said about quantum correlations, in special about quantum JP? For that we will introduce our quantum JP witnessing. The use of witnessing functions is a common technique to attest entanglement [258].

5.7.4 Quantum JP: Witnessing

Note: the derivation of our quantum JP witnessing was done by F. Shahandeh, who should receive the due credit for the text in this subsection (5.7.4). This is part of our article in preparation.

We restrict ourselves to the superposition with respect to the optical coherent states $\{|\beta\rangle : \beta \in \mathbb{C}\}$. Within the quantum optics literature, this corresponds to the nonclassicality of Glauber-Sudarshan P distribution. However, a similar approach can be elaborated for any other s-parameterized distribution [25, 169].

For any operator $\hat{A}$ of bosonic systems, an example of which is light, its P distribution is given by

$$P_{\hat{A}}(\alpha) = Tr\hat{T}(\alpha,1)\hat{A}, \tag{5.72}$$

in which, given the quadratures x and p, $\alpha = (x+ip)/\sqrt{2}$ is a point in the complex phase-space plane and $\hat{T}(\alpha,1)$, known as the normally-ordered Wigner operator, is obtained via Fourier transform of the normally ordered displacement operator $\hat{D}(\xi,1) = e^{|\xi|^2/2}\hat{D}(\xi)$. Here, $\hat{D}(\xi) = \exp\{\xi a^\dagger - \xi^* a\}$ in which a and $a^\dagger$ are the bosonic annihilation and creation operators, respectively, and $\xi \in \mathbb{C}$. It is easy to show that $P_\beta(\alpha) = Tr\hat{T}(\alpha,1)|\beta\rangle\langle\beta| = \pi\delta^{(2)}(\alpha-\beta)$ for a coherent state $|\beta\rangle$ with $\delta^{(2)}(\alpha-\beta)$ being the two-dimensional Dirac delta [25]. Thus, for an arbitrary operator $\hat{A}$ we can formally write

$$\hat{A} = \int \frac{d^2\alpha}{\pi} P_{\hat{A}}(\alpha)|\alpha\rangle\langle\alpha|. \tag{5.73}$$

Using Eq. 5.73, we can give the trace rule as

$$Tr\hat{A}\hat{B} = \int \frac{d^2\alpha}{\pi} P_{\hat{A}}(\alpha)Q_{\hat{B}}(\alpha), \tag{5.74}$$

in which $Q_{\hat{B}}(\alpha) = \langle\alpha|\hat{B}|\alpha\rangle$ is known as Husimi-Kano Q-distribution of $\hat{B}$. Clearly, the Husimi-Kano Q-distribution is positive for every positive operator (e.g., quantum states). Every other qusiprobability can attain negative values even for positive operators.

Let us denote the set of all quantum states for which the P-distribution can be interpreted as a proper classical probability density by $\mathscr{S}_{cl}$. From linearity of Eq. 5.72 it is clear that $\mathscr{S}_{cl}$ is a closed compact convex set with coherent states as its extremal (i.e. boundary) points. Any quantum state $\hat{\rho} \notin \mathscr{S}_{cl}$, called a phase-space nonclassicality (PSNC) state, cannot be decomposed as a probabilistic mixture of optical coherent states and thus, it must possess a negative P-distribution.

By Hahn-Banach theorem, for every point outside a convex set there exists a hyperplane, known as a witness, which separates the point from the set. Quantum mechanically, this implies that for any PSNC state $\hat{\rho} \notin \mathscr{S}_{cl}$, one can always find a Hermitian operator $\hat{W}$ such that (i) $Tr\hat{W}\hat{\rho} < 0$, while, (ii) $Tr\hat{W}\hat{\sigma} \geqslant 0$ for every $\hat{\sigma} \in \mathscr{S}_{cl}$. From condition (i) it follows that $\hat{W}$ is not a positive operator. We also conclude from (ii) that $\hat{W}$ must possesses a positive Q-distribution, otherwise there would exist some coherent state $|\beta\rangle$ for which $Tr\hat{W}|\beta\rangle\langle\beta| < 0$. Furthermore, since any quantum state has a positive Q-distribution, it follows from Eq. 5.74 that the P-distribution of the witness must have negativities to be able to satisfy condition (i) at least for some states. In summary, the witness operator $\hat{W}$ is a non-positive operator with a positive Q-distribution and a P-distribution which attains negative values.

Despite the subtleties regarding P- and Q-distributions of the witness operators, it is very easy to construct potential PSNC witnesses. First, we note that $\min_{\mathscr{S}_{cl}} Tr\hat{W}\hat{\sigma}$ is always achieved for one of the extremal points, that is, for some coherent state $\hat{\sigma} = \beta$. This simply means $\min_{\mathscr{S}_{cl}} Tr\hat{W}\hat{\sigma} = \min_{\alpha} Q_{\hat{W}}(\alpha)$. Now, choose an appropriate bounded positive Hermitian test operator $\hat{L}$ with finite support and define the following operator:

$$\hat{W} = g_0\hat{I} - \hat{L}, \tag{5.75}$$

where $g_0 = \max_{\alpha} Q_{\hat{L}}(\alpha)$. Then, $\min_{\alpha} Q_{\hat{W}}(\alpha) = 0$ and $\hat{W}$ is optimal. As long as $\hat{W}$ is not positive, there potentially exist PSNC quantum states for which $Tr\hat{W}\hat{\rho} < 0$. The set of all such witnesses are necessary and sufficient for detecting nonclassicality [259–261].

5.7.5 Quantum JP: Results and Data Analysis

Note: the text in this subsection (5.7.5) was written by M. Ringbauer and R. A. Abrahao based on the text for our article in preparation.

In the following, we are aiming to witness the quantum JP correlation using the theory presented in the previous subsection. As a remainder, this corresponds to a bipartite phase-randomized squeezed vacuum state, which features a negative joint P-distribution, while both local P-distribution appear thermal, such that:

$$\rho \propto \sum_n \varepsilon^n \left(|n\rangle\langle n| \otimes |n\rangle\langle n|\right). \tag{5.76}$$

Equation 5.76 suggests that the distinguishing signature of the desired state is found in the photon-number statistics between Alice and Bob. For any separable (i.e. classical) state, which is in general a product of coherent states of the form $\rho_{cl}^{\alpha,\beta} = |\alpha\rangle\langle\alpha| \otimes |\alpha\rangle\langle\beta|$, one finds that the probability of

	$\|0\rangle_A$	$\|1\rangle_A$	$\|2\rangle_A$	$\|3\rangle_A$	$\|4\rangle_A$	$\|5\rangle_A$
$\|0\rangle_B$	0.375311	0.183902	0.0450561	0.00735916	0.000901497	0.0000883467
$\|1\rangle_B$	0.183902	0.0901122	0.0220775	0.00360599	0.000441734	0.0000432899
$\|2\rangle_B$	0.0450561	0.0220775	0.00540898	0.000883467	0.000108225	0.000010606
$\|3\rangle_B$	0.00735916	0.00360599	0.000883467	0.0001443	0.0000176767	1.73232×10^{-6}
$\|4\rangle_B$	0.000901497	0.000441734	0.000108225	0.0000176767	2.1654×10^{-6}	2.12209×10^{-7}
$\|5\rangle_B$	0.0000883467	0.0000432899	0.000010606	1.73232×10^{-6}	2.12209×10^{-7}	2.07965×10^{-8}

Figure 5.13: Classical statistics for $\alpha = \beta = 0.7$.

	$\|0\rangle_A$	$\|1\rangle_A$	$\|2\rangle_A$	$\|3\rangle_A$	$\|4\rangle_A$
$\|0\rangle_B$	0.979814	0.00917786	0.0000919831	2.40445×10^{-7}	0.
$\|1\rangle_B$	0.00673709	0.00108067	0.0000113009	2.52362×10^{-8}	0.
$\|2\rangle_B$	0.00265097	0.000388636	3.51344×10^{-6}	1.12161×10^{-8}	0.
$\|3\rangle_B$	0.0000327986	0.000010276	9.60377×10^{-8}	0.	0.
$\|4\rangle_B$	3.24565×10^{-7}	1.72447×10^{-7}	0.	0.	0.

Figure 5.14: Experimental statistics.

obtaining n and m photon detections for Alice and Bob, respectively, is given by:

$$P(n,m|\rho_{cl}^{\alpha,\beta}) = Tr[|n\rangle\langle n||\alpha\rangle\langle\alpha|]Tr[|m\rangle\langle m||\beta\rangle\langle\beta|] \tag{5.77}$$

$$= Q_n(\alpha)Q_m(\beta). \tag{5.78}$$

Here $Q_n(\alpha)$ is the Q-distribution of an n-photon state evaluated at point α in phase-space, and $Q_n(\beta)$ is the Q-distribution of an m-photon state evaluated at point β in phase-space.

For very large values of $\varepsilon \sim 1$, a simple calculation reveals that the state of Eq. 5.76 attains expectation values for $Tr[\rho(|n\rangle\langle n|\otimes|n\rangle\langle n|)]$ that cannot be achieved by any classical state. On the other hand, for states with $\varepsilon \ll 1$, which are typical even for state-of-the-art experiments, the states are still non-classical, yet the above described approach does not work, because the single expectation value can be matched by uncorrelated coherent states.

In order to detect the nonclassicality of states for all non-zero values of ε, we use a more refined witnessing procedure based on the idea of ultrafine entanglement witnessing. Specifically, we note that the requirement for a classical state to attain a certain expectation value for one measurement will preclude the same classical state from matching certain other expectation values. This idea allows us to construct a whole family of ultrafine witnesses. One such witness could be given by the maximal value of $Tr[\rho(|2\rangle\langle\otimes||2\rangle\langle 2|)]$ obtainable by any classical state under the condition that the same state achieves a value of $Tr[\rho(|1\rangle\langle 1|\otimes|1\rangle\langle 1|)] = z$ for some constant z. We denote this witness by $W_{\langle 22\rangle|\langle 11\rangle=z}$. Similarly, one can consider witnesses with two constraints, such as $W_{\langle 22\rangle|\langle 11\rangle=z_1,\langle 00\rangle=z_0}$.

For the dataset in Fig. 5.14, we had to circumvent a few problems. Since no 33 events have been recorded, the analysis is restricted to the 3 expectation values $\langle 00\rangle$, $\langle 11\rangle$, and $\langle 22\rangle$.

Firstly, if one decides to avoid using the $\langle 00\rangle$, one is left with one choice of single-constraint witness, which is $W_{\langle 22\rangle|\langle 11\rangle=0.0010807(9)} = 0.00684(1)$, where the numbers in parenthesis correspond to 3-sigma statistical uncertainty. This witness is not violated by the measured value of $\langle 22\rangle = 3.5(1)\times10^{-6}$.

Hence, we have to resort to two-constraint witnesses, which means we have to condition on the 00 outcome. That should not be a limiting problem, as 00 terms were used to successfully reconstruct different coherent states from data during the phase of calibration of the detectors [211].

Thus, the witness $W_{\langle 22\rangle|\langle 11\rangle=0.0010807(9),\langle 00\rangle=0.97981(3)} = 2.65(4)\times 10^{-9}$ is indeed violated by the measured value of $\langle 22\rangle = 3.5(1)\times 10^{-6}$. Additionally, the single-constraint witness $W_{\langle 11\rangle|\langle 00\rangle=0.97981(3)} = 0.000102(1)$ is violated by the measured value of $\langle 11\rangle = 0.0010807(9)$.

Experimental uncertainties can be taken into account by adjusting the constraint values to the measured value plus 3 sigma experimental uncertainty.

5.8 Conclusion

We provided experimental evidence on quantum JP, a new kind of quantum correlation beyond discord. It was predicted in 2013 on the work of E. Agudelo, J. Sperling, and W. Vogel [217], and here, considering the assumptions presented in data analysis, we support their findings. Despite the many experimental challenges, we were able to reach an interesting conclusion. This new quantum correlation can find applications in quantum computing, as predicted in the theoretical works of F. Shahandeh, A. Lund, and T. Ralph [218,219]. The present work aims to contribute to better understand foundational questions in Quantum Mechanics, especially the role of quantum correlations.

Post scriptum: After the submission of this Thesis, I became aware of the work of Sperling *et al.* [262], which is similar to the work presented here, but also different. From the experimental point of view, Sperling *et al.* [262] use multiplexed Avalanche Photodiodes (APDs), while we use photon number-resolving Transition Edge Sensors. Additionally, we take a different method to analyse the data. In Sperling *et al.* [262], the authors aim to reconstruct a quantum state and conclude it matches the equation for Spontaneous Parametric Down Conversion (Equation 7 in their paper), and then they point out that this equation relates to the conclusions of the work of Agudelo *et al.* [217], and therefore they claim to certify the quantum correlation mentioned in Agudelo *et al.* [217]. Our approach is different. Here, we do not aim to reconstruct any quantum state. Instead, in our method we present a direct witness to certify the new correlation discussed by Agudelo *et al.* [217], and we also discuss it relating it to the other types of quantum correlations. For instance, the work Sperling *et al.* [262] makes no reference to quantum discord. The reader may also find more comments on Shahandeh *et al.* [218] based on Ferraro *et al.* [263].

Chapter 6

Conclusion and outlook

> All the efforts of the human mind cannot exhaust the essence of a single fly.
>
> St. Thomas Aquinas

The aim of this Thesis was to explore the frontiers of Quantum Optics in 4 fronts: (1) quantum photonics tools, (2) quantum computing and computational complexity, (3) quantum metrology, and (4) quantum correlations.

In Chapter 1, we presented the reader with a minimal introduction to single-photon sources and how to evaluate some of their basic properties.

Chapter 2 dealt directly with the task of advancing our quantum photonics tools. The MuChOS chip is a viable technology for experimentalists which can tremendously simplify the preparation of a large number of manifold single photons. It is the first of its kind. For the maturing of this technology, more work is necessary on the fabrication in order to reduce optical losses in the waveguide propagation. Additional improvements can come from better coupling to the waveguides and decreasing the optical losses in the air-chip interface by applying anti-reflection technology.

Chapter 3 presented a theoretical proposal for efficient implementation of a Boson Sampling experiment and efficient verification. The Extended Church-Turing Thesis (ECT) is facing growing challenges from the emerging quantum computation technology. Furthermore, a better understanding of the computational class of Bounded-Error Quantum Polynomial-Time (BQP), simply the class of quantum computation, is needed to apprehend the limits on classical and quantum computations, and consequently, the full potential of quantum computation.

Of course, these questions make one wonder what will be the prevailing platform for quantum computation: photons, ions, superconducting qubits, silicon qubits, and so on. At this point, for applications with 50-100 qubits, the race is being led by superconducting qubits. But that does not answer the daunting challenge of scalability. And for that, photons cannot be ruled out. As state by

one of the leaders in this field of optical quantum computing, Prof. Jeremy O'Brien[1]: "There is a million ways to make one qubit. There is one way to make a million qubits". And, up to present day, photons are the most viable path to reach the orders of millions of qubits.

One should also consider the possibility of multi-platform quantum computation, where processing nodes are interconnected by photons. The processing nodes may be of many different technologies, for example, ions or superconducting qubits. And for obvious reasons, photons are crucial for connecting the nodes of quantum networks.

Chapter 4 demonstrated a new protocol of quantum metrology. This improved method to estimate the spatial characteristics of distant light sources with no prior knowledge of their structure is specially appealing for applications in Astronomy. The demonstration of this new protocol was only made possible due to the use of number-resolving photon detectors. There is many possibilities to explore in Quantum Optics with the addition of number-resolved photon detection. Furthermore, quantum metrology offers a rich field of application of quantum technologies by taking measurements to their fundamental limits.

Chapter 5 brought the reader to the topic of quantum correlations. We reported our experimental progress in our aim to demonstrate a new kind of quantum correlation beyond quantum entanglement and quantum discord. For the scope of this thesis, this new correlation was named quantum JP. In fact, we were able to present experimental evidence of quantum JP. It would not surprise me if more applications are discovered where quantum JP is a key ingredient. This was the historical path taken by quantum entanglement and quantum discord. Noteworthy the crescent activities to test quantum correlations in other scenarios: more dimensions (beyond qubits), more parties (eg. quantum networks with multiple qubits), and different platforms (eg. quantum optomechanics).

Despite its maturity, the field of Quantum Optics remains invigorated and fertile. For those interested, welcome aboard and let's have a *bon voyage*!

[1] Statement heard in person in the public lecture at the 8th Workshop on Quantum Simulation and Quantum Walks (2018) in Perth, WA, Australia.

Bibliography

[1] F. Lenzini, B. Haylock, J. C. Loredo, R. A. Abrahão, N. A. Zakaria, S. Kasture, I. Sagnes, A. Lemaitre, H.-P. Phan, D. V. Dao, P. Senellart, M. P. Almeida, A. G. White, and M. Lobino, "Active demultiplexing of single photons from a solid-state source," *Laser & Photonics Reviews*, vol. 11, no. 3, p. 1600297, 2017.

[2] L. A. Howard, G. G. Gillett, M. E. Pearce, R. A. Abrahao, T. J. Weinhold, P. Kok, and A. G. White, "Optimal imaging of remote bodies using quantum detectors," *Phys. Rev. Lett.*, vol. 123, p. 143604, Sep 2019.

[3] R. A. Abrahao and A. P. Lund, "Continuous-Variables Boson Sampling: Scaling and Verification," *arXiv:1812.08978*, 2018.

[4] R. A. Abrahao, F. Shahandeh, G. Gillett, M. Ringbauer, T. Weinhold, M. P. Almeida, T. C. Ralph, and A. G. White, "The quest for nonclassicality using number-resolving single-photon detectors," in *Frontiers in Optics / Laser Science*, p. JTu2A.55, Optical Society of America, 2018.

[5] B. P. Abbott, R. Abbott, T. Abbott, M. Abernathy, F. Acernese, K. Ackley, C. Adams, T. Adams, P. Addesso, R. Adhikari, *et al.*, "Observation of gravitational waves from a binary black hole merger," *Physical Review Letters*, vol. 116, no. 6, p. 061102, 2016.

[6] M. Fox, *Quantum optics: an introduction*, vol. 15. Oxford University Press, 2006.

[7] D. F. Walls and G. J. Milburn, *Quantum optics*. Springer Science & Business Media, 2007.

[8] C. Gerry, P. Knight, and P. L. Knight, *Introductory quantum optics*. Cambridge University Press, 2005.

[9] G. Grynberg, A. Aspect, and C. Fabre, *Introduction to quantum optics: from the semi-classical approach to quantized light*. Cambridge University Press, 2010.

[10] R. Loudon, *The quantum theory of light*. OUP Oxford, 2000.

[11] M. O. Scully and M. S. Zubairy, *Quantum optics*. AAPT, 1999.

[12] L. Mandel and E. Wolf, *Optical coherence and quantum optics*. Cambridge University Press, 1995.

[13] H.-A. Bachor and T. C. Ralph, *A guide to experiments in quantum optics*. Wiley, 2004.

[14] J. C. Garrison and R. Y. Chiao, *Quantum Optics*. Oxford University Press, 2008.

[15] J. J. Sakurai and J. Napolitano, *Modern quantum mechanics*. Pearson Education, 2011.

[16] P. Kok and B. W. Lovett, *Introduction to optical quantum information processing*. Cambridge University Press, 2010.

[17] R. Menzel, *Photonics: linear and nonlinear interactions of laser light and matter*. Springer Science & Business Media, 2013.

[18] B. E. Saleh and M. C. Teich, *Fundamentals of photonics*. John Wiley & Sons, 2019.

[19] R. H. Brown and R. Q. Twiss, "Correlation between photons in two coherent beams of light," *Nature*, vol. 177, no. 4497, pp. 27–29, 1956.

[20] R. H. Brown and R. Twiss, "A test of a new type of stellar interferometer on sirius," *Nature*, vol. 178, no. 4541, pp. 1046–1048, 1956.

[21] R. H. Brown and R. Q. Twiss, "Interferometry of the intensity fluctuations in light-i. basic theory: the correlation between photons in coherent beams of radiation," *Proceedings of the Royal Society of London. Series A. Mathematical and Physical Sciences*, vol. 242, no. 1230, pp. 300–324, 1957.

[22] R. H. Brown and R. Twiss, "Interferometry of the intensity fluctuations in light. ii. an experimental test of the theory for partially coherent light," *Proceedings of the Royal Society of London. Series A. Mathematical and Physical Sciences*, vol. 243, no. 1234, pp. 291–319, 1958.

[23] H. J. Kimble, M. Dagenais, and L. Mandel, "Photon antibunching in resonance fluorescence," *Physical Review Letters*, vol. 39, no. 11, p. 691, 1977.

[24] P. Grangier, G. Roger, and A. Aspect, "Experimental evidence for a photon anticorrelation effect on a beam splitter: a new light on single-photon interferences," *EPL (Europhysics Letters)*, vol. 1, no. 4, p. 173, 1986.

[25] R. J. Glauber, *Quantum theory of optical coherence: selected papers and lectures*. John Wiley & Sons, 2007.

[26] C.-K. Hong, Z.-Y. Ou, and L. Mandel, "Measurement of subpicosecond time intervals between two photons by interference," *Physical Review Letters*, vol. 59, no. 18, p. 2044, 1987.

[27] N. K. Langford, *Encoding, manipulating and measuring quantum information in optics*. PhD Thesis, University of Queensland, 2007.

[28] T. Kobayashi, R. Ikuta, S. Yasui, S. Miki, T. Yamashita, H. Terai, T. Yamamoto, M. Koashi, and N. Imoto, "Frequency-domain Hong–Ou–Mandel interference," *Nature Photonics*, vol. 10, no. 7, p. 441, 2016.

[29] R. Lopes, A. Imanaliev, A. Aspect, M. Cheneau, D. Boiron, and C. I. Westbrook, "Atomic Hong–Ou–Mandel experiment," *Nature*, vol. 520, no. 7545, p. 66, 2015.

[30] M. Rambach, W. S. Lau, S. Laibacher, V. Tamma, A. G. White, and T. J. Weinhold, "Hectometer revivals of quantum interference," *Physical Review letters*, vol. 121, no. 9, p. 093603, 2018.

[31] C. Santori, D. Fattal, J. Vučković, G. S. Solomon, and Y. Yamamoto, "Indistinguishable photons from a single-photon device," *Nature*, vol. 419, no. 6907, p. 594, 2002.

[32] Y.-H. Deng, H. Wang, X. Ding, Z.-C. Duan, J. Qin, M.-C. Chen, Y. He, Y.-M. He, J.-P. Li, Y.-H. Li, L.-C. Peng, E. S. Matekole, T. Byrnes, C. Schneider, M. Kamp, D.-W. Wang, J. P. Dowling, S. Höfling, C.-Y. Lu, M. O. Scully, and J.-W. Pan, "Quantum interference between light sources separated by 150 million kilometers," *Phys. Rev. Lett.*, vol. 123, p. 080401, Aug 2019.

[33] M. Jachura and R. Chrapkiewicz, "Shot-by-shot imaging of Hong–Ou–Mandel interference with an intensified sCMOS camera," *Optics letters*, vol. 40, no. 7, pp. 1540–1543, 2015.

[34] *Shot-by-shot imaging of Hong–Ou–Mandel interference with an intensified sCMOS camera*, https://www.youtube.com/watch?v=g8wP4V5GDTI (accessed June 19, 2019).

[35] P. A. M. Dirac, *The principles of quantum mechanics*. No. 27, Oxford University Press, 1981.

[36] I. Aharonovich, D. Englund, and M. Toth, "Solid-state single-photon emitters," *Nature Photonics*, vol. 10, no. 10, p. 631, 2016.

[37] N. Somaschi, V. Giesz, L. De Santis, J. Loredo, M. P. Almeida, G. Hornecker, S. L. Portalupi, T. Grange, C. Antón, J. Demory, *et al.*, "Near-optimal single-photon sources in the solid state," *Nature Photonics*, vol. 10, no. 5, p. 340, 2016.

[38] J. C. Loredo, *Enabling Multi-Photon Experiments with Solid-State Emitters: A Farewell to Downconversion*. PhD Thesis, University of Queensland, 2016.

[39] N. Gisin, G. Ribordy, W. Tittel, and H. Zbinden, "Quantum cryptography," *Reviews of Modern Physics*, vol. 74, no. 1, p. 145, 2002.

[40] C. H. Bennett and G. Brassard, "Quantum cryptography: public key distribution and coin tossing.," *Theor. Comput. Sci.*, vol. 560, no. 12, pp. 7–11, 2014.

[41] R. Raussendorf and H. J. Briegel, "A one-way quantum computer," *Physical Review Letters*, vol. 86, no. 22, p. 5188, 2001.

[42] P. Walther, K. J. Resch, T. Rudolph, E. Schenck, H. Weinfurter, V. Vedral, M. Aspelmeyer, and A. Zeilinger, "Experimental one-way quantum computing," *Nature*, vol. 434, no. 7030, p. 169, 2005.

[43] G. S. Solomon, C. Santori, and A. Kuhn, *Single Emitters in Isolated Quantum Systems*, vol. 45. Elsevier, 2013.

[44] O. Gazzano, S. M. De Vasconcellos, C. Arnold, A. Nowak, E. Galopin, I. Sagnes, L. Lanco, A. Lemaître, and P. Senellart, "Bright solid-state sources of indistinguishable single photons," *Nature Communications*, vol. 4, p. 1425, 2013.

[45] L. Lanco and P. Senellart, "A highly efficient single photon-single quantum dot interface," in *Engineering the Atom-Photon Interaction*, pp. 39–71, Springer, 2015.

[46] P. Senellart, G. Solomon, and A. White, "High-performance semiconductor quantum-dot single-photon sources," *Nature Nanotechnology*, vol. 12, no. 11, p. 1026, 2017.

[47] P. Lodahl, S. Mahmoodian, and S. Stobbe, "Interfacing single photons and single quantum dots with photonic nanostructures," *Reviews of Modern Physics*, vol. 87, no. 2, p. 347, 2015.

[48] M. Fox, *Optical Properties of Solids*. Oxford University Press, 2010.

[49] E. M. Purcell, H. C. Torrey, and R. V. Pound, "Resonance absorption by nuclear magnetic moments in a solid," *Physical Review*, vol. 69, no. 1-2, p. 37, 1946.

[50] S. Haroche and J.-M. Raimond, *Exploring the quantum: atoms, cavities, and photons*. Oxford University Press, 2006.

[51] E. B. Flagg, A. Muller, J. Robertson, S. Founta, D. Deppe, M. Xiao, W. Ma, G. Salamo, and C.-K. Shih, "Resonantly driven coherent oscillations in a solid-state quantum emitter," *Nature Physics*, vol. 5, no. 3, p. 203, 2009.

[52] H. Wang, H. Hu, T.-H. Chung, J. Qin, X. Yang, J.-P. Li, R.-Z. Liu, H.-S. Zhong, Y.-M. He, X. Ding, *et al.*, "On-demand semiconductor source of entangled photons which simultaneously has high fidelity, efficiency, and indistinguishability," *Physical Review Letters*, vol. 122, no. 11, p. 113602, 2019.

[53] *Quandela*, http://quandela.com/ (accessed May 23, 2019).

[54] L. De Santis, C. Antón, B. Reznychenko, N. Somaschi, G. Coppola, J. Senellart, C. Gómez, A. Lemaître, I. Sagnes, and A. G. e. a. White, "A solid-state single-photon filter," *Nature Nanotechnology*, vol. 12, no. 7, p. 663, 2017.

[55] R. W. Boyd, *Nonlinear optics*. Elsevier, 2003.

[56] Y.-R. Shen, *The Principles of Nonlinear Optics*. New York, Wiley-Interscience, 2002.

[57] Z. Tang, R. Chandrasekara, Y. C. Tan, C. Cheng, K. Durak, and A. Ling, "The photon pair source that survived a rocket explosion," *Scientific Reports*, vol. 6, p. 25603, 2016.

[58] A. Christ, A. Fedrizzi, H. Hübel, T. Jennewein, and C. Silberhorn, "Parametric down-conversion," in *Experimental Methods in the Physical Sciences*, vol. 45, pp. 351–410, Elsevier, 2013.

[59] C. Kurtsiefer, M. Oberparleiter, and H. Weinfurter, "Generation of correlated photon pairs in type-ii parametric down conversion—revisited," *Journal of Modern Optics*, vol. 48, no. 13, pp. 1997–2007, 2001.

[60] J. W. Silverstone, D. Bonneau, K. Ohira, N. Suzuki, H. Yoshida, N. Iizuka, M. Ezaki, C. M. Natarajan, M. G. Tanner, R. H. Hadfield, *et al.*, "On-chip quantum interference between silicon photon-pair sources," *Nature Photonics*, vol. 8, no. 2, p. 104, 2014.

[61] J. W. Silverstone, R. Santagati, D. Bonneau, M. J. Strain, M. Sorel, J. L. O'Brien, and M. G. Thompson, "Qubit entanglement between ring-resonator photon-pair sources on a silicon chip," *Nature Communications*, vol. 6, p. 7948, 2015.

[62] A. McMillan, Y.-P. Huang, B. Bell, A. Clark, P. Kumar, and J. Rarity, "Four-wave mixing in single-mode optical fibers," in *Experimental Methods in the Physical Sciences*, vol. 45, pp. 411–465, Elsevier, 2013.

[63] V. G. Dmitriev, G. G. Gurzadyan, and D. N. Nikogosyan, *Handbook of nonlinear optical crystals*, vol. 64. Springer, 2013.

[64] C. Monken, P. S. Ribeiro, and S. Pádua, "Optimizing the photon pair collection efficiency: A step toward a loophole-free bell's inequalities experiment," *Physical Review A*, vol. 57, no. 4, p. R2267, 1998.

[65] D. Bouwmeester, A. Ekert, and A. Zeilinger, *The Physics of Quantum Information: Quantum Cryptography, Quantum Teleportation, Quantum Computation*. Springer, 2000.

[66] R. Horodecki, P. Horodecki, M. Horodecki, and K. Horodecki, "Quantum entanglement," *Reviews of modern physics*, vol. 81, no. 2, p. 865, 2009.

[67] A. Einstein, B. Podolsky, and N. Rosen, "Can quantum-mechanical description of physical reality be considered complete?," *Physical Review*, vol. 47, no. 10, p. 777, 1935.

[68] N. Bohr, "Can quantum-mechanical description of physical reality be considered complete?," *Physical Review*, vol. 48, no. 8, p. 696, 1935.

[69] M. Ringbauer, *Exploring quantum foundations with single photons*. Springer, 2017.

[70] A. Dousse, J. Suffczyński, A. Beveratos, O. Krebs, A. Lemaître, I. Sagnes, J. Bloch, P. Voisin, and P. Senellart, "Ultrabright source of entangled photon pairs," *Nature*, vol. 466, no. 7303, p. 217, 2010.

[71] O. Benson, C. Santori, M. Pelton, and Y. Yamamoto, "Regulated and entangled photons from a single quantum dot," *Physical Review Letters*, vol. 84, no. 11, p. 2513, 2000.

[72] P. G. Kwiat, K. Mattle, H. Weinfurter, A. Zeilinger, A. V. Sergienko, and Y. Shih, "New high-intensity source of polarization-entangled photon pairs," *Physical Review Letters*, vol. 75, no. 24, p. 4337, 1995.

[73] P. G. Kwiat, E. Waks, A. G. White, I. Appelbaum, and P. H. Eberhard, "Ultrabright source of polarization-entangled photons," *Physical Review A*, vol. 60, no. 2, p. R773, 1999.

[74] A. Mair, A. Vaziri, G. Weihs, and A. Zeilinger, "Entanglement of the orbital angular momentum states of photons," *Nature*, vol. 412, no. 6844, p. 313, 2001.

[75] J. T. Barreiro, N. K. Langford, N. A. Peters, and P. G. Kwiat, "Generation of hyperentangled photon pairs," *Phys. Rev. Lett.*, vol. 95, p. 260501, Dec 2005.

[76] P. G. Kwiat, "Hyper-entangled states," *Journal of Modern Optics*, vol. 44, no. 11-12, pp. 2173–2184, 1997.

[77] M. Prilmüller, T. Huber, M. Müller, P. Michler, G. Weihs, and A. Predojević, "Hyperentanglement of photons emitted by a quantum dot," *Phys. Rev. Lett.*, vol. 121, p. 110503, Sep 2018.

[78] A. Aspuru-Guzik and P. Walther, "Photonic quantum simulators," *Nature Physics*, vol. 8, no. 4, p. 285, 2012.

[79] B. P. Lanyon, J. D. Whitfield, G. G. Gillett, M. E. Goggin, M. P. Almeida, I. Kassal, J. D. Biamonte, M. Mohseni, B. J. Powell, M. Barbieri, *et al.*, "Towards quantum chemistry on a quantum computer," *Nature Chemistry*, vol. 2, no. 2, p. 106, 2010.

[80] F. Kaneda, B. G. Christensen, J. J. Wong, H. S. Park, K. T. McCusker, and P. G. Kwiat, "Time-multiplexed heralded single-photon source," *Optica*, vol. 2, no. 12, pp. 1010–1013, 2015.

[81] F. Kaneda and P. G. Kwiat, "High-efficiency single-photon generation via large-scale active time multiplexing," *arXiv:1803.04803*, 2018.

[82] J. B. Spring, P. L. Mennea, B. J. Metcalf, P. C. Humphreys, J. C. Gates, H. L. Rogers, C. Söller, B. J. Smith, W. S. Kolthammer, P. G. Smith, *et al.*, "Chip-based array of near-identical, pure, heralded single-photon sources," *Optica*, vol. 4, no. 1, pp. 90–96, 2017.

[83] H. Wang, W. Li, X. Jiang, Y.-M. He, Y.-H. Li, X. Ding, M.-C. Chen, J. Qin, C.-Z. Peng, C. Schneider, M. Kamp, W.-J. Zhang, H. Li, L.-X. You, Z. Wang, J. P. Dowling, S. Höfling, C.-Y. Lu, and J.-W. Pan, "Toward Scalable Boson Sampling with Photon Loss," *Phys. Rev. Lett.*, vol. 120, p. 230502, Jun 2018.

[84] F. Lenzini, S. Kasture, B. Haylock, and M. Lobino, "Anisotropic model for the fabrication of annealed and reverse proton exchanged waveguides in congruent lithium niobate," *Opt. Express*, vol. 23, pp. 1748–1756, May 2015.

[85] H. F. Taylor, "Optical switching and modulation in parallel dielectric waveguides," *J. Appl. Phys.*, vol. 44, p. 3257, May 1973.

[86] O. Alibart, V. D'Auria, M. De Micheli, F. Doutre, F. Kaiser, L. Labonté, T. Lunghi, E. Picholle, and S. Tanzilli, "Quantum photonics at telecom wavelengths based on lithium niobate waveguides," *Journal of Optics*, vol. 18, no. 10, p. 104001, 2016.

[87] P. Sharapova, K. Luo, H. Herrmann, M. Reichelt, T. Meier, and C. Silberhorn, "Toolbox for the design of linbo3-based passive and active integrated quantum circuits," *New Journal of Physics*, vol. 19, no. 12, p. 123009, 2017.

[88] J. C. Loredo, M. A. Broome, P. Hilaire, O. Gazzano, I. Sagnes, A. Lemaitre, M. P. Almeida, P. Senellart, and A. G. White, "Boson Sampling with Single-Photon Fock States from a Bright Solid-State Source," *Phys. Rev. Lett.*, vol. 118, p. 130503, Mar 2017.

[89] B. Haylock, F. Lenzini, S. Kasture, P. Fisher, E. W. Streed, and M. Lobino, "Nine-channel mid-power bipolar pulse generator based on a field programmable gate array," *Review of Scientific Instruments*, vol. 87, no. 5, p. 054709, 2016.

[90] J. C. Loredo, N. A. Zakaria, N. Somaschi, C. Anton, L. de Santis, V. Giesz, T. Grange, M. A. Broome, O. Gazzano, G. Coppola, I. Sagnes, A. Lemaitre, A. Auffeves, P. Senellart, M. P. Almeida, and A. G. White, "Scalable performance in solid-state single-photon sources," *Optica*, vol. 3, pp. 433–440, Apr 2016.

[91] X. Ding, Y. He, Z.-C. Duan, N. Gregersen, M.-C. Chen, S. Unsleber, S. Maier, C. Schneider, M. Kamp, S. Höfling, C.-Y. Lu, and J.-W. Pan, "On-demand single photons with high extraction efficiency and near-unity indistinguishability from a resonantly driven quantum dot in a micropillar," *Phys. Rev. Lett.*, vol. 116, p. 020401, Jan 2016.

[92] L. Midolo, S. L. Hansen, W. Zhang, C. Papon, R. Schott, A. Ludwig, A. D. Wieck, P. Lodahl, and S. Stobbe, "Electro-optic routing of photons from a single quantum dot in photonic integrated circuits," *Opt. Express*, vol. 25, pp. 33514–33526, Dec 2017.

[93] T. Hummel, C. Ouellet-Plamondon, E. Ugur, I. Kulkova, T. Lund-Hansen, M. A. Broome, R. Uppu, and P. Lodahl, "Efficient demultiplexed single-photon source with a quantum dot coupled to a nanophotonic waveguide," *Applied Physics Letters*, vol. 115, no. 2, p. 021102, 2019.

[94] C. Papon, X. Zhou, H. Thyrrestrup, Z. Liu, S. Stobbe, R. Schott, A. D. Wieck, A. Ludwig, P. Lodahl, and L. Midolo, "Nanomechanical single-photon routing," *Optica*, vol. 6, no. 4, pp. 524–530, 2019.

[95] H. Wang, Z.-C. Duan, Y.-H. Li, S. Chen, J.-P. Li, Y.-M. He, M.-C. Chen, Y. He, X. Ding, C.-Z. Peng, C. Schneider, M. Kamp, S. Höfling, C.-Y. Lu, and J.-W. Pan, "Near-transform-limited single photons from an efficient solid-state quantum emitter," *Phys. Rev. Lett.*, vol. 116, p. 213601, May 2016.

[96] C. Moore and S. Mertens, *The nature of computation*. Oxford University Press, 2011.

[97] E. Desurvire, *Classical and quantum information theory: an introduction for the telecom scientist*. Cambridge University Press, 2009.

[98] Complexity Zoo, *https://complexityzoo.uwaterloo.ca/Complexityzoo*.

[99] L. G. Khachiyan, "A polynomial algorithm in linear programming," *Doklady Academii Nauk SSSR*, vol. 244, pp. 1093–1096, 1979.

[100] J. Edmonds, "Paths, trees, and flowers," *Canadian Journal of mathematics*, vol. 17, pp. 449–467, 1965.

[101] M. Agrawal, N. Kayal, and N. Saxena, "Primes is in p," *Annals of mathematics*, pp. 781–793, 2004.

[102] *co-NP*, https://en.wikipedia.org/wiki/Co-NP (accessed on August 1, 2019).

[103] L. G. Valiant, "The complexity of computing the permanent," *Theoretical computer science*, vol. 8, no. 2, pp. 189–201, 1979.

[104] A. C.-C. Yao, "Quantum circuit complexity," *Proceedings of 1993 IEEE 34th Annual Foundations of Computer Science*, pp. 352–361, 1993.

[105] L. J. Stockmeyer, "The polynomial-time hierarchy," *Theoretical Computer Science*, vol. 3, no. 1, pp. 1–22, 1976.

[106] A. Lund, M. J. Bremner, and T. Ralph, "Quantum sampling problems, BosonSampling and quantum supremacy," *npj Quantum Information*, vol. 3, no. 1, p. 15, 2017.

[107] S. Aaronson and A. Arkhipov, "The computational complexity of linear optics," *Theory of Computing*, vol. 9, no. 4, pp. 143–252, 2013.

[108] A. W. Harrow and A. Montanaro, "Quantum computational supremacy," *Nature*, vol. 549, no. 7671, p. 203, 2017.

[109] P. W. Shor, "Algorithms for quantum computation: Discrete logarithms and factoring," in *Proceedings 35th Annual Symposium on Foundations of Computer Science*, pp. 124–134, IEEE, 1994.

[110] S. Aaronson and A. Ambainis, "Forrelation: A problem that optimally separates quantum from classical computing," *arXiv:1411.5729*, 2014.

[111] C. S. Calude and E. Calude, "The road to quantum computational supremacy," *arXiv:1712.01356*, 2017.

[112] D. J. Brod, E. F. Galvão, A. Crespi, R. Osellame, N. Spagnolo, and F. Sciarrino, "Photonic implementation of boson sampling: a review," *Advanced Photonics*, vol. 1, no. 3, p. 034001, 2019.

[113] F. Arute, K. Arya, R. Babbush, D. Bacon, J. C. Bardin, R. Barends, R. Biswas, S. Boixo, F. G. Brandao, D. A. Buell, *et al.*, "Quantum supremacy using a programmable superconducting processor," *Nature*, vol. 574, no. 7779, pp. 505–510, 2019.

[114] D. Deutsch, "Quantum theory, the church–turing principle and the universal quantum computer," *Proceedings of the Royal Society of London. A. Mathematical and Physical Sciences*, vol. 400, no. 1818, pp. 97–117, 1985.

[115] E. Bernstein and U. Vazirani, "Quantum complexity theory," *SIAM J. Comput.*, vol. 26, p. 1411–1473, Oct. 1997.

[116] P. P. Rohde, K. R. Motes, P. A. Knott, and W. J. Munro, "Will boson-sampling ever disprove the extended church-turing thesis?," *arXiv preprint arXiv:1401.2199*, 2014.

[117] P. Kok, W. J. Munro, K. Nemoto, T. C. Ralph, J. P. Dowling, and G. J. Milburn, "Linear optical quantum computing with photonic qubits," *Reviews of Modern Physics*, vol. 79, no. 1, p. 135, 2007.

[118] E. Knill, R. Laflamme, and G. J. Milburn, "A scheme for efficient quantum computation with linear optics," *Nature*, vol. 409, no. 6816, p. 46, 2001.

[119] M. Reck, A. Zeilinger, H. J. Bernstein, and P. Bertani, "Experimental realization of any discrete unitary operator," *Phys. Rev. Lett.*, vol. 73, pp. 58–61, Jul 1994.

[120] W. R. Clements, P. C. Humphreys, B. J. Metcalf, W. S. Kolthammer, and I. A. Walmsley, "Optimal design for universal multiport interferometers," *Optica*, vol. 3, pp. 1460–1465, Dec 2016.

[121] S. Aaronson, *Quantum Complexity and Quantum Optics I*, https://www.youtube.com/watch?v=9RvKCI5k0aAlist=WLindex=2 (accessed on August 7, 2019).

[122] S. Aaronson, *Quantum Complexity and Quantum Optics II*, https://www.youtube.com/watch?v=bV9EOTrYHA8list=WLindex=4 (accessed on August 7, 2019).

[123] S. Aaronson, *Quantum Complexity and Quantum Optics III*, https://www.youtube.com/watch?v=wSggMd4-X1slist=WLindex=5 (accessed on August 7, 2019).

[124] S. Aaronson, *Quantum Complexity and Quantum Optics IV*, https://www.youtube.com/watch?v=Dvxsap19F1clist=WLindex=6 (accessed on August 7, 2019).

[125] S. Scheel, K. Nemoto, W. J. Munro, and P. L. Knight, "Measurement-induced nonlinearity in linear optics," *Phys. Rev. A*, vol. 68, p. 032310, Sep 2003.

[126] S. Scheel, "Permanents in linear optical networks," *arXiv:0406127*, 2004.

[127] M. A. Broome, A. Fedrizzi, S. Rahimi-Keshari, J. Dove, S. Aaronson, T. C. Ralph, and A. G. White, "Photonic Boson Sampling in a Tunable Circuit," *Science*, vol. 339, no. 6121, pp. 794–798, 2013.

[128] J. B. Spring, B. J. Metcalf, P. C. Humphreys, W. S. Kolthammer, X.-M. Jin, M. Barbieri, A. Datta, N. Thomas-Peter, N. K. Langford, D. Kundys, J. C. Gates, B. J. Smith, P. G. R. Smith, and I. A. Walmsley, "Boson Sampling on a Photonic Chip," *Science*, vol. 339, no. 6121, pp. 798–801, 2013.

[129] A. Crespi, N. Spagnolo, P. Mataloni, R. Ramponi, E. Maiorino, D. Brod, R. Osellame, F. Sciarrino, C. Vitelli, and E. Galvao, "Experimental boson sampling in arbitrary integrated photonic circuits," *Nature Photonics*, vol. 7, p. 545, 2012.

[130] M. Tillmann, B. Dakić, R. Heilmann, S. Nolte, A. Szameit, and P. Walther, "Experimental boson sampling," *Nature Photonics*, vol. 7, no. 7, p. 540, 2013.

[131] T. J. Weinhold, A. Gilchrist, K. J. Resch, A. C. Doherty, J. L. O'Brien, G. J. Pryde, and A. G. White, "Understanding photonic quantum-logic gates: The road to fault tolerance," *arXiv:0808.0794*, 2008.

[132] A. P. Lund, A. Laing, S. Rahimi-Keshari, T. Rudolph, J. L. O'Brien, and T. C. Ralph, "Boson Sampling from a Gaussian State," *Phys. Rev. Lett.*, vol. 113, p. 100502, Sep 2014.

[133] M. Bentivegna, N. Spagnolo, C. Vitelli, F. Flamini, N. Viggianiello, L. Latmiral, P. Mataloni, D. J. Brod, E. F. Galvão, A. Crespi, R. Ramponi, R. Osellame, and F. Sciarrino, "Experimental scattershot boson sampling," *Science Advances*, vol. 1, no. 3, 2015.

[134] C. Cahall, K. L. Nicolich, N. T. Islam, G. P. Lafyatis, A. J. Miller, D. J. Gauthier, and J. Kim, "Multi-photon detection using a conventional superconducting nanowire single-photon detector," *Optica*, vol. 4, pp. 1534–1535, Dec 2017.

[135] P. Lodahl, S. Mahmoodian, and S. Stobbe, "Interfacing single photons and single quantum dots with photonic nanostructures," *Reviews of Modern Physics*, vol. 87, no. 2, p. 347, 2015.

[136] J. C. Loredo, M. A. Broome, P. Hilaire, O. Gazzano, I. Sagnes, A. Lemaitre, M. P. Almeida, P. Senellart, and A. G. White, "Boson sampling with single-photon fock states from a bright solid-state source," *Phys. Rev. Lett.*, vol. 118, p. 130503, Mar 2017.

[137] Y. He, X. Ding, Z.-E. Su, H.-L. Huang, J. Qin, C. Wang, S. Unsleber, C. Chen, H. Wang, Y.-M. He, X.-L. Wang, W.-J. Zhang, S.-J. Chen, C. Schneider, M. Kamp, L.-X. You, Z. Wang, S. Höfling, C.-Y. Lu, and J.-W. Pan, "Time-Bin-Encoded Boson Sampling with a Single-Photon Device," *Phys. Rev. Lett.*, vol. 118, p. 190501, May 2017.

[138] H. Wang, J. Qin, X. Ding, M.-C. Chen, S. Chen, X. You, Y.-M. He, X. Jiang, L. You, Z. Wang, C. Schneider, J. J. Renema, S. Höfling, C.-Y. Lu, and J.-W. Pan, "Boson Sampling with 20 Input Photons and a 60-Mode Interferometer in a 10^{14}-Dimensional Hilbert Space," *Phys. Rev. Lett.*, vol. 123, p. 250503, Dec 2019.

[139] C. S. Hamilton, R. Kruse, L. Sansoni, S. Barkhofen, C. Silberhorn, and I. Jex, "Gaussian Boson Sampling," *Phys. Rev. Lett.*, vol. 119, p. 170501, Oct 2017.

[140] R. Kruse, C. S. Hamilton, L. Sansoni, S. Barkhofen, C. Silberhorn, and I. Jex, "A detailed study of Gaussian Boson Sampling," *arXiv:1801.07488*, 2018.

[141] S. Paesani, Y. Ding, R. Santagati, L. Chakhmakhchyan, C. Vigliar, K. Rottwitt, L. K. Oxenløwe, J. Wang, M. G. Thompson, and A. Laing, "Generation and sampling of quantum states of light in a silicon chip," *Nature Physics*, pp. 1–5, 2019.

[142] A. Arkhipov, "BosonSampling is robust against small errors in the network matrix," *Phys. Rev. A*, vol. 92, p. 062326, Dec 2015.

[143] P. P. Rohde and T. C. Ralph, "Error tolerance of the boson-sampling model for linear optics quantum computing," *Physical Review A*, vol. 85, no. 2, p. 022332, 2012.

[144] S. Aaronson and D. J. Brod, "BosonSampling with lost photons," *Physical Review A*, vol. 93, no. 1, p. 012335, 2016.

[145] A. Leverrier and R. García-Patrón, "Analysis of circuit imperfections in BosonSampling," *Quantum Information & Computation*, vol. 15, pp. 489–512, 2015.

[146] S. Rahimi-Keshari, T. C. Ralph, and C. M. Caves, "Sufficient conditions for efficient classical simulation of quantum optics," *Physical Review X*, vol. 6, no. 2, p. 021039, 2016.

[147] M. Oszmaniec and D. J. Brod, "Classical simulation of photonic linear optics with lost particles," *arXiv:1801.06166*, 2018.

[148] R. García-Patrón, J. J. Renema, and V. Shchesnovich, "Simulating boson sampling in lossy architectures," *arXiv:1712.10037*, 2017.

[149] J. Renema, V. Shchesnovich, and R. Garcia-Patron, "Classical simulability of noisy boson sampling," *arXiv:1809.01953*, 2018.

[150] D. J. Brod and M. Oszmaniec, "Classical simulation of linear optics subject to nonuniform losses," *arXiv:1906.06696*, 2019.

[151] J. Huh, G. G. Guerreschi, B. Peropadre, J. R. McClean, and A. Aspuru-Guzik, "Boson sampling for molecular vibronic spectra," *Nature Photonics*, vol. 9, no. 9, p. 615, 2015.

[152] C. Sparrow, E. Martín-López, N. Maraviglia, A. Neville, C. Harrold, J. Carolan, Y. N. Joglekar, T. Hashimoto, N. Matsuda, J. L. O'Brien, *et al.*, "Simulating the vibrational quantum dynamics of molecules using photonics," *Nature*, vol. 557, no. 7707, p. 660, 2018.

[153] A. Aspuru-Guzik and P. Walther, "Photonic quantum simulators," *Nature Physics*, vol. 8, no. 4, p. 285, 2012.

[154] I. Georgescu, S. Ashhab, and F. Nori, "Quantum simulation," *Reviews of Modern Physics*, vol. 86, no. 1, p. 153, 2014.

[155] J. M. Arrazola, E. Diamanti, and I. Kerenidis, "Quantum superiority for verifying np-complete problems with linear optics," *npj Quantum Information*, vol. 4, no. 1, p. 56, 2018.

[156] K. R. Motes, J. P. Olson, E. J. Rabeaux, J. P. Dowling, S. J. Olson, and P. P. Rohde, "Linear optical quantum metrology with single photons: Exploiting spontaneously generated entanglement to beat the shot-noise limit," *Phys. Rev. Lett.*, vol. 114, p. 170802, Apr 2015.

[157] Z. Huang, P. P. Rohde, D. W. Berry, P. Kok, J. P. Dowling, and C. Lupo, "Boson sampling private-key quantum cryptography," *arXiv:1905.03013*, 2019.

[158] S. Boixo, S. V. Isakov, V. N. Smelyanskiy, R. Babbush, N. Ding, Z. Jiang, M. J. Bremner, J. M. Martinis, and H. Neven, "Characterizing quantum supremacy in near-term devices," *Nature Physics*, vol. 14, no. 6, p. 595, 2018.

[159] C. Neill, P. Roushan, K. Kechedzhi, S. Boixo, S. Isakov, V. Smelyanskiy, A. Megrant, B. Chiaro, A. Dunsworth, K. Arya, *et al.*, "A blueprint for demonstrating quantum supremacy with superconducting qubits," *Science*, vol. 360, no. 6385, pp. 195–199, 2018.

[160] F. Flamini, N. Spagnolo, and F. Sciarrino, "Photonic quantum information processing: a review," *arXiv:1803.02790*, 2018.

[161] A. Neville, C. Sparrow, R. Clifford, E. Johnston, P. M. Birchall, A. Montanaro, and A. Laing, "Classical boson sampling algorithms with superior performance to near-term experiments," *Nature Physics*, vol. 13, no. 12, p. 1153, 2017.

[162] P. Clifford and R. Clifford, "The Classical Complexity of Boson Sampling," *arXiv:1706.01260*, 2017.

[163] S. Yokoyama, R. Ukai, S. C. Armstrong, C. Sornphiphatphong, T. Kaji, S. Suzuki, J.-i. Yoshikawa, H. Yonezawa, N. C. Menicucci, and A. Furusawa, "Ultra-large-scale continuous-variable cluster states multiplexed in the time domain," *Nature Photonics*, vol. 7, no. 12, p. 982, 2013.

[164] J.-i. Yoshikawa, S. Yokoyama, T. Kaji, C. Sornphiphatphong, Y. Shiozawa, K. Makino, and A. Furusawa, "Invited article: Generation of one-million-mode continuous-variable cluster state by unlimited time-domain multiplexing," *APL Photonics*, vol. 1, no. 6, p. 060801, 2016.

[165] H. Vahlbruch, M. Mehmet, K. Danzmann, and R. Schnabel, "Detection of 15 db squeezed states of light and their application for the absolute calibration of photoelectric quantum efficiency," *Phys. Rev. Lett.*, vol. 117, p. 110801, Sep 2016.

[166] N. C. Menicucci, "Fault-tolerant measurement-based quantum computing with continuous-variable cluster states," *Phys. Rev. Lett.*, vol. 112, p. 120504, Mar 2014.

[167] D. Gottesman, A. Kitaev, and J. Preskill, "Encoding a qubit in an oscillator," *Phys. Rev. A*, vol. 64, p. 012310, Jun 2001.

[168] K. R. Motes, A. Gilchrist, J. P. Dowling, and P. P. Rohde, "Scalable Boson Sampling with Time-Bin Encoding Using a Loop-Based Architecture," *Phys. Rev. Lett.*, vol. 113, p. 120501, Sep 2014.

[169] U. Leonhardt, *Measuring the quantum state of light*. Cambridge University Press, 1997.

[170] J. G. Webb, T. C. Ralph, and E. H. Huntington, "Homodyne measurement of the average photon number," *Physical Review A*, vol. 73, no. 3, p. 033808, 2006.

[171] M. M. Wilde, *Quantum Information Theory*. Cambridge University Press, 2013.

[172] M. A. Nielsen and I. L. Chuang, *Quantum computation and Quantum Information*. Cambridge University Press, 2000.

[173] L. Aolita, C. Gogolin, M. Kliesch, and J. Eisert, "Reliable quantum certification of photonic state preparations," *Nature Communications*, vol. 6, nov 2015.

[174] C. Weedbrook, S. Pirandola, R. García-Patrón, N. J. Cerf, T. C. Ralph, J. H. Shapiro, and S. Lloyd, "Gaussian quantum information," *Reviews of Modern Physics*, vol. 84, no. 2, p. 621, 2012.

[175] S. Takeda and A. Furusawa, "Universal quantum computing with measurement-induced continuous-variable gate sequence in a loop-based architecture," *Physical Review Letters*, vol. 119, no. 12, p. 120504, 2017.

[176] T. Serikawa, Y. Shiozawa, H. Ogawa, N. Takanashi, S. Takeda, J.-i. Yoshikawa, and A. Furusawa, "Quantum information processing with a travelling wave of light," in *Integrated Optics: Devices, Materials, and Technologies XXII*, vol. 10535, p. 105351B, International Society for Optics and Photonics, 2018.

[177] S. Takeda and A. Furusawa, "Toward large-scale fault-tolerant universal photonic quantum computing," *APL Photonics*, vol. 4, no. 6, p. 060902, 2019.

[178] V. Giovannetti, S. Lloyd, and L. Maccone, "Advances in quantum metrology," *Nature Photonics*, vol. 5, no. 4, p. 222, 2011.

[179] J. P. Dowling, "Quantum optical metrology – the lowdown on high-N00N states," *Contemporary Physics*, vol. 49, no. 2, pp. 125–143, 2008.

[180] J. S. Sidhu and P. Kok, "A geometric perspective on quantum parameter estimation," *arXiv:1907.06628*, 2019.

[181] S. Ragy, M. Jarzyna, and R. Demkowicz-Dobrzański, "Compatibility in multiparameter quantum metrology," *Physical Review A*, vol. 94, pp. 052108–11, Nov. 2016.

[182] M. J. Rust, M. Bates, and X. Zhuang, "Sub-diffraction-limit imaging by stochastic optical reconstruction microscopy (STORM)," *Nature Methods*, vol. 3, no. 10, p. 793, 2006.

[183] E. Betzig, G. H. Patterson, R. Sougrat, O. W. Lindwasser, S. Olenych, J. S. Bonifacino, M. W. Davidson, J. Lippincott-Schwartz, and H. F. Hess, "Imaging intracellular fluorescent proteins at nanometer resolution," *Science*, vol. 313, no. 5793, pp. 1642–1645, 2006.

[184] M. Fernández-Suárez and A. Y. Ting, "Fluorescent probes for super-resolution imaging in living cells," *Nature Reviews Molecular Cell Biology*, vol. 9, no. 12, p. 929, 2008.

[185] A. N. Boto, P. Kok, D. S. Abrams, S. L. Braunstein, C. P. Williams, and J. P. Dowling, "Quantum interferometric optical lithography: exploiting entanglement to beat the diffraction limit," *Physical Review Letters*, vol. 85, p. 2733, 2000.

[186] M. D'Angelo, M. V. Chekhova, and Y. Shih, "Two-Photon Diffraction and Quantum Lithography," *Physical Review Letters*, vol. 87, no. 1, pp. 777–4, 2001.

[187] Y. Shih, "Quantum imaging," *IEEE Journal of Selected Topics in Quantum Electronics*, vol. 13, no. 4, pp. 1016–1030, 2007.

[188] S. Lloyd, "Enhanced sensitivity of photodetection via quantum illumination," *Science*, vol. 321, no. 5895, pp. 1463–1465, 2008.

[189] G. B. Lemos, V. Borish, G. D. Cole, S. Ramelow, R. Lapkiewicz, and A. Zeilinger, "Quantum imaging with undetected photons," *Nature*, vol. 512, no. 7515, p. 409, 2014.

[190] S. Slussarenko, M. M. Weston, H. M. Chrzanowski, L. K. Shalm, V. B. Verma, S. W. Nam, and G. J. Pryde, "Unconditional violation of the shot-noise limit in photonic quantum metrology," *Nature Photonics*, vol. 11, no. 11, p. 700, 2017.

[191] M. W. Mitchell, J. S. Lundeen, and A. M. Steinberg, "Super-resolving phase measurements with a multiphoton entangled state," *Nature*, vol. 429, no. 6988, pp. 161–164, 2004.

[192] *Super-Resolution Microscopy Tutorial*, https://advanced-microscopy.utah.edu/education/super-res/ (accessed August 14, 2019).

[193] M. Tsang, R. Nair, and X.-M. Lu, "Quantum Theory of Superresolution for Two Incoherent Optical Point Sources," *Physical Review X*, vol. 6, no. 3, pp. 031033–17, 2016.

[194] J. S. Sidhu and P. Kok, "Quantum metrology of spatial deformation using arrays of classical and quantum light emitters," *Physical Review A*, vol. 95, p. 063829, 2017.

[195] M. Tsang, "Subdiffraction incoherent optical imaging via spatial-mode demultiplexing," *New Journal of Physics*, vol. 19, no. 2, pp. 1–15, 2017.

[196] Z. S. Tang, K. Durak, and A. Ling, "Fault-tolerant and finite-error localization for point emitters within the diffraction limit," *Optics Express*, vol. 24, no. 19, pp. 22004–9, 2016.

[197] M. Paúr, B. Stoklasa, Z. Hradil, L. L. Sánchez-Soto, and J. Řeháček, "Achieving the ultimate optical resolution," *Optica*, vol. 3, no. 10, pp. 1144–4, 2016.

[198] F. Yang, A. Tashchilina, E. S. Moiseev, C. Simon, and A. I. Lvovsky, "Far-field linear optical superresolution via heterodyne detection in a higher-order local oscillator mode," *Optica*, vol. 3, no. 10, pp. 1148–5, 2016.

[199] J. Řehaček, Z. Hradil, B. Stoklasa, M. Paúr, J. Grover, A. Krzic, and L. Sánchez-Soto, "Multiparameter quantum metrology of incoherent point sources: Towards realistic superresolution," *Physical Review A*, vol. 96, no. 6, pp. 062107–7, 2017.

[200] R. Schneider, T. Mehringer, G. Mercurio, L. Wenthaus, A. Classen, G. Brenner, O. Gorobtsov, A. Benz, D. Bhatti, L. Bocklage, B. Fischer, S. Lazarev, Y. Obukhov, K. Schlage, P. Skopintsev, J. Wagner, F. Waldmann, S. Willing, I. Zaluzhnyy, W. Wurth, I. A. Vartanyants, R. Röhlsberger, and J. von Zanthier, "Quantum imaging with incoherently scattered light from a free-electron laser," *Nature Physics*, vol. 14, no. 2, p. 126, 2018.

[201] S. Oppel, T. Büttner, P. Kok, and J. von Zanthier, "Superresolving multiphoton interferences with independent light sources," *Physical Review Letters*, vol. 109, p. 233603, 2012.

[202] M. E. Pearce, T. Mehringer, J. von Zanthier, and P. Kok, "Precision estimation of source dimensions from higher-order intensity correlations," *Physical Review A*, vol. 92, no. 4, pp. 043831–12, 2015.

[203] M. Genovese, "Real applications of quantum imaging," *Journal of Optics*, vol. 18, no. 7, pp. 073002–10, 2016.

[204] L. Mandel and E. Wolf, *Optical Coherence and Quantum Optics*. Cambridge University Press, 1995.

[205] M. E. Pearce, E. T. Campbell, and P. Kok, "Optimal quantum metrology of distant black bodies," *Quantum*, vol. 1, p. 21, 2017.

[206] C. W. Helstrom, "Cramer-Rao inequalities for operator-valued measures in quantum mechanics," *International Journal of Theoretical Physics*, vol. 8, no. 5, pp. 361–376, 1973.

[207] W. Martienssen and E. Spiller, "Coherence and Fluctuations in Light Beams," *American Journal of Physics*, vol. 32, no. 1, pp. 919–926, 1964.

[208] K. Pieper, A. Bergmann, R. Dengler, and C. Rockstuhl, "Using a pseudo-thermal light source to teach spatial coherence," *European Journal of Physics*, vol. 39, no. 4, p. 045303, 2018.

[209] K. Pieper, A. Bergmann, R. Dengler, and C. Rockstuhl, "Corrigendum:'using a pseudo-thermal light source to teach spatial coherence'(2018 eur. j. phys. 39 045303)," *European Journal of Physics*, 2018.

[210] A. Haner and N. Isenor, "Intensity correlations from pseudothermal light sources," *American Journal of Physics*, vol. 38, no. 6, pp. 748–750, 1970.

[211] G. G. Gillett, *A hardware signal processor for Transition Edge Sensors*. PhD Thesis, University of Queensland, 2017.

[212] J. C. Matthews, X.-Q. Zhou, H. Cable, P. J. Shadbolt, D. J. Saunders, G. A. Durkin, G. J. Pryde, and J. L. O'Brien, "Towards practical quantum metrology with photon counting," *npj Quantum Information*, vol. 2, no. 1, pp. 1–7, 2016.

[213] W. H. Zurek, "Decoherence and the transition from quantum to classical," *Physics Today*, vol. 44, 1991.

[214] H. Ollivier and W. H. Zurek, "Quantum discord: a measure of the quantumness of correlations," *Phys. Rev. Lett.*, vol. 88, p. 017901, Dec 2001.

[215] L. Henderson and V. Vedral, "Classical, quantum and total correlations," *Journal of Physics A: Mathematical and General*, vol. 34, pp. 6899–6905, aug 2001.

[216] B. Dakić, Y. O. Lipp, X. Ma, M. Ringbauer, S. Kropatschek, S. Barz, T. Paterek, V. Vedral, A. Zeilinger, Č. Brukner, *et al.*, "Quantum discord as resource for remote state preparation," *Nature Physics*, vol. 8, no. 9, p. 666, 2012.

[217] E. Agudelo, J. Sperling, and W. Vogel, "Quasiprobabilities for multipartite quantum correlations of light," *Phys. Rev. A*, vol. 87, p. 033811, Mar 2013.

[218] F. Shahandeh, A. P. Lund, and T. C. Ralph, "Quantum Correlations in Nonlocal Boson Sampling," *Phys. Rev. Lett.*, vol. 119, p. 120502, Sep 2017.

[219] F. Shahandeh, A. P. Lund, and T. C. Ralph, "Quantum correlations and global coherence in distributed quantum computing," *Phys. Rev. A*, vol. 99, p. 052303, May 2019.

[220] G. Adesso, T. R. Bromley, and M. Cianciaruso, "Measures and applications of quantum correlations," *Journal of Physics A: Mathematical and Theoretical*, vol. 49, no. 47, p. 473001, 2016.

[221] D. H. Smith, G. Gillett, M. P. de Almeida, C. Branciard, A. Fedrizzi, T. J. Weinhold, A. Lita, B. Calkins, T. Gerrits, H. M. Wiseman, S. W. Nam, and A. G. White, "Conclusive quantum steering with superconducting transition-edge sensors," *Nature Communications*, vol. 3, pp. 625 EP –, Jan 2012. Article.

[222] V. Händchen, T. Eberle, S. Steinlechner, A. Samblowski, T. Franz, R. F. Werner, and R. Schnabel, "Observation of one-way einstein–podolsky–rosen steering," *Nature Photonics*, vol. 6, no. 8, p. 596, 2012.

[223] B. Wittmann, S. Ramelow, F. Steinlechner, N. K. Langford, N. Brunner, H. M. Wiseman, R. Ursin, and A. Zeilinger, "Loophole-free Einstein–Podolsky–Rosen experiment via quantum steering," *New Journal of Physics*, vol. 14, no. 5, p. 053030, 2012.

[224] N. Tischler, F. Ghafari, T. J. Baker, S. Slussarenko, R. B. Patel, M. M. Weston, S. Wollmann, L. K. Shalm, V. B. Verma, S. W. Nam, H. C. Nguyen, H. M. Wiseman, and G. J. Pryde, "Conclusive Experimental Demonstration of One-Way Einstein-Podolsky-Rosen Steering," *Phys. Rev. Lett.*, vol. 121, p. 100401, Sep 2018.

[225] H. M. Wiseman, S. J. Jones, and A. C. Doherty, "Steering, Entanglement, Nonlocality, and the Einstein-Podolsky-Rosen Paradox," *Phys. Rev. Lett.*, vol. 98, p. 140402, Apr 2007.

[226] J. S. Bell, "On the Einstein Podolsky Rosen paradox," *Physics*, vol. 1, pp. 195–200, Nov 1964.

[227] J. S. Bell, *"Speakable and Unspeakable in Quantum Mechanics"*. Cambridge University Press, 2004.

[228] J. F. Clauser, M. A. Horne, A. Shimony, and R. A. Holt, "Proposed experiment to test local hidden-variable theories," *Phys. Rev. Lett.*, vol. 23, pp. 880–884, Oct 1969.

[229] N. Brunner, D. Cavalcanti, S. Pironio, V. Scarani, and S. Wehner, "Bell nonlocality," *Reviews of Modern Physics*, vol. 86, no. 2, p. 419, 2014.

[230] V. Scarani, *"Bell Nonlocality"*. Oxford University Press, 2019.

[231] Y. Aharonov and D. Rohrlich, *Quantum paradoxes: quantum theory for the perplexed*. Wiley-VCH, 2005.

[232] B. S. Cirel'son, "Quantum generalizations of Bell's inequality," *Letters in Mathematical Physics*, vol. 4, pp. 93–100, Mar 1980.

[233] G. Weihs, T. Jennewein, C. Simon, H. Weinfurter, and A. Zeilinger, "Violation of Bell's Inequality under Strict Einstein Locality Conditions," *Phys. Rev. Lett.*, vol. 81, pp. 5039–5043, Dec 1998.

[234] S. J. Freedman and J. F. Clauser, "Experimental test of local hidden-variable theories," *Phys. Rev. Lett.*, vol. 28, pp. 938–941, Apr 1972.

[235] A. Aspect, P. Grangier, and G. Roger, "Experimental Tests of Realistic Local Theories via Bell's Theorem," *Phys. Rev. Lett.*, vol. 47, pp. 460–463, Aug 1981.

[236] A. Aspect, P. Grangier, and G. Roger, "Experimental Realization of Einstein-Podolsky-Rosen-Bohm Gedankenexperiment: A New Violation of Bell's Inequalities," *Phys. Rev. Lett.*, vol. 49, pp. 91–94, Jul 1982.

[237] A. Aspect, J. Dalibard, and G. Roger, "Experimental Test of Bell's Inequalities Using Time-Varying Analyzers," *Phys. Rev. Lett.*, vol. 49, pp. 1804–1807, Dec 1982.

[238] B. Hensen, H. Bernien, A. E. Dréau, A. Reiserer, N. Kalb, M. S. Blok, J. Ruitenberg, R. F. L. Vermeulen, R. N. Schouten, C. Abellán, W. Amaya, V. Pruneri, M. W. Mitchell, M. Markham, D. J. Twitchen, D. Elkouss, S. Wehner, T. H. Taminiau, and R. Hanson, "Loophole-free Bell inequality violation using electron spins separated by 1.3 kilometres," *Nature*, vol. 526, pp. 682 EP –, Oct 2015.

[239] L. K. Shalm, E. Meyer-Scott, B. G. Christensen, P. Bierhorst, M. A. Wayne, M. J. Stevens, T. Gerrits, S. Glancy, D. R. Hamel, M. S. Allman, K. J. Coakley, S. D. Dyer, C. Hodge, A. E. Lita, V. B. Verma, C. Lambrocco, E. Tortorici, A. L. Migdall, Y. Zhang, D. R. Kumor, W. H. Farr, F. Marsili, M. D. Shaw, J. A. Stern, C. Abellán, W. Amaya, V. Pruneri, T. Jennewein, M. W. Mitchell, P. G. Kwiat, J. C. Bienfang, R. P. Mirin, E. Knill, and S. W. Nam, "Strong Loophole-Free Test of Local Realism," *Phys. Rev. Lett.*, vol. 115, p. 250402, Dec 2015.

[240] M. Giustina, M. A. M. Versteegh, S. Wengerowsky, J. Handsteiner, A. Hochrainer, K. Phelan, F. Steinlechner, J. Kofler, J.-A. Larsson, C. Abellán, W. Amaya, V. Pruneri, M. W. Mitchell, J. Beyer, T. Gerrits, A. E. Lita, L. K. Shalm, S. W. Nam, T. Scheidl, R. Ursin, B. Wittmann, and A. Zeilinger, "Significant-Loophole-Free Test of Bell's Theorem with Entangled Photons," *Phys. Rev. Lett.*, vol. 115, p. 250401, Dec 2015.

[241] H. S. Poh, S. K. Joshi, A. Cerè, A. Cabello, and C. Kurtsiefer, "Approaching Tsirelson's Bound in a Photon Pair Experiment," *Phys. Rev. Lett.*, vol. 115, p. 180408, Oct 2015.

[242] D. Salart, A. Baas, C. Branciard, N. Gisin, and H. Zbinden, "Testing the speed of 'spooky action at a distance'," *Nature*, vol. 454, no. 7206, p. 861, 2008.

[243] J. L. O'Brien, G. J. Pryde, A. G. White, T. C. Ralph, and D. Branning, "Demonstration of an all-optical quantum controlled-not gate," *Nature*, vol. 426, no. 6964, p. 264, 2003.

[244] R. Raussendorf and H. J. Briegel, "A one-way quantum computer," *Phys. Rev. Lett.*, vol. 86, pp. 5188–5191, May 2001.

[245] A. K. Ekert, "Quantum cryptography based on Bell's theorem," *Phys. Rev. Lett.*, vol. 67, pp. 661–663, Aug 1991.

[246] A. Acín, N. Brunner, N. Gisin, S. Massar, S. Pironio, and V. Scarani, "Device-independent security of quantum cryptography against collective attacks," *Phys. Rev. Lett.*, vol. 98, p. 230501, Jun 2007.

[247] C. H. Bennett, G. Brassard, C. Crépeau, R. Jozsa, A. Peres, and W. K. Wootters, "Teleporting an unknown quantum state via dual classical and Einstein-Podolsky-Rosen channels," *Phys. Rev. Lett.*, vol. 70, pp. 1895–1899, Mar 1993.

[248] T. M. Cover and J. A. Thomas, *Elements of Information Theory*. John Wiley & Sons, 2006.

[249] C. E. Shannon, "A mathematical theory of communication," *The Bell System Technical Journal*, vol. 27, pp. 379–423, July 1948.

[250] R. F. Werner, "Quantum states with Einstein-Podolsky-Rosen correlations admitting a hidden-variable model," *Phys. Rev. A*, vol. 40, pp. 4277–4281, Oct 1989.

[251] A. Datta, A. Shaji, and C. M. Caves, "Quantum discord and the power of one qubit," *Phys. Rev. Lett.*, vol. 100, p. 050502, Feb 2008.

[252] B. P. Lanyon, M. Barbieri, M. P. Almeida, and A. G. White, "Experimental quantum computing without entanglement," *Phys. Rev. Lett.*, vol. 101, p. 200501, Nov 2008.

[253] M. Gu, H. M. Chrzanowski, S. M. Assad, T. Symul, K. Modi, T. C. Ralph, V. Vedral, and P. K. Lam, "Observing the operational significance of discord consumption," *Nature Physics*, vol. 8, no. 9, p. 671, 2012.

[254] E. Wigner, "On the quantum correction for thermodynamic equilibrium," *Phys. Rev.*, vol. 40, pp. 749–759, Jun 1932.

[255] R. J. Glauber, "The quantum theory of optical coherence," *Physical Review*, vol. 130, no. 6, p. 2529, 1963.

[256] E. C. G. Sudarshan, "Equivalence of semiclassical and quantum mechanical descriptions of statistical light beams," *Phys. Rev. Lett.*, vol. 10, pp. 277–279, Apr 1963.

[257] A. Datta, "A condition for the nullity of quantum discord," *arXiv:1003.5256*, 2010.

[258] F. Shahandeh, M. Ringbauer, J. C. Loredo, and T. C. Ralph, "Ultrafine entanglement witnessing," *Phys. Rev. Lett.*, vol. 118, p. 110502, Mar 2017.

[259] E. V. Shchukin and W. Vogel, "Nonclassical moments and their measurement," *Phys. Rev. A*, vol. 72, p. 043808, Oct 2005.

[260] S. Gerke, J. Sperling, W. Vogel, Y. Cai, J. Roslund, N. Treps, and C. Fabre, "Full Multipartite Entanglement of Frequency-Comb Gaussian States," *Phys. Rev. Lett.*, vol. 114, p. 050501, Feb 2015.

[261] M. Mraz, J. Sperling, W. Vogel, and B. Hage, "Witnessing the degree of nonclassicality of light," *Phys. Rev. A*, vol. 90, p. 033812, Sep 2014.

[262] J. Sperling, M. Bohmann, W. Vogel, G. Harder, B. Brecht, V. Ansari, and C. Silberhorn, "Uncovering quantum correlations with time-multiplexed click detection," *Physical Review Letters*, vol. 115, no. 2, p. 023601, 2015.

[263] A. Ferraro and M. G. Paris, "Nonclassicality criteria from phase-space representations and information-theoretical constraints are maximally inequivalent," *Physical Review Letters*, vol. 108, no. 26, p. 260403, 2012.

[264] T. Gerrits, A. Lita, B. Calkins, and S. W. Nam, "Superconducting transition edge sensors for quantum optics," in *Superconducting devices in quantum optics*, pp. 31–60, Springer, 2016.

[265] A. E. Lita, A. J. Miller, and S. W. Nam, "Counting near-infrared single-photons with 95% efficiency," *Opt. Express*, vol. 16, pp. 3032–3040, Mar 2008.

[266] A. Garg and N. D. Mermin, "Detector inefficiencies in the Einstein-Podolsky-Rosen experiment," *Phys. Rev. D*, vol. 35, pp. 3831–3835, Jun 1987.

[267] J.-A. Larsson, "Bell's inequality and detector inefficiency," *Phys. Rev. A*, vol. 57, pp. 3304–3308, May 1998.

[268] M. Giustina, A. Mech, S. Ramelow, B. Wittmann, J. Kofler, J. Beyer, A. Lita, B. Calkins, T. Gerrits, S. W. Nam, R. Ursin, and A. Zeilinger, "Bell violation using entangled photons without the fair-sampling assumption," *Nature*, vol. 497, pp. 227 EP –, Apr 2013.

[269] M. A. Rowe, D. Kielpinski, V. Meyer, C. A. Sackett, W. M. Itano, C. Monroe, and D. J. Wineland, "Experimental violation of a Bell's inequality with efficient detection," *Nature*, vol. 409, no. 6822, pp. 791–794, 2001.

[270] I. Gerhardt, Q. Liu, A. Lamas-Linares, J. Skaar, V. Scarani, V. Makarov, and C. Kurtsiefer, "Experimentally Faking the Violation of Bell's Inequalities," *Phys. Rev. Lett.*, vol. 107, p. 170404, Oct 2011.

Appendix A

Transition Edge Sensors for number-resolved photon detection

A.1 Introduction

Usually single-photon detectors refer to Avalanche Photodiodes (APD) or Superconducting Nanowire Detectors (SND). The former are intrinsically not number-resolving, i.e., they can not differentiate the number of impinging photons. The latter has demonstrated limited number resolution, up to 4 photons [134]. In this Appendix, we will discuss *highly efficient and number-resolving photon detectors* called **Transition Edge Sensors (TES)**, which have demonstrated high number-resolution up to 13 photons with the potential for even greater number of photons [211]. These detectors were used for the experiments described in Chapters 4 and 5. The TES installed at the Quantum Technology Laboratory were fabricated by the group of Dr. S. W. Nam at the National Institute of Standards and Technology, Boulder, Colorado, USA. Parts of the hardware and the software to run them were develop by Dr. Geoff Gillett [211]. Here we will briefly discuss TES operation, but further description can be found in Reference [264]. Additionally, our TES were previously used in a quantum optics experiment to test quantum steering [221].

A.2 Transition Edge Sensors

Transition Edge Sensors are sensitive calorimeters that measure the photon energy and operate in the transition between the superconducting and normal conduction states where resistance changes sharply with temperature. When detecting monochromatic light, a TES acts as a number-resolving photon detector. Our TES are made of thin film of Tungsten whose critical temperature is $T_C = 150$ mK. The operation of a TES as a photon detector is explained in the sequence of Figures A.1, A.2, and A.3. Considerable work was employed to post-process all the data generated by the TES. A final number attribution leads to a histogram as depicted in Fig. A.4, and zoomed in Fig. A.5.

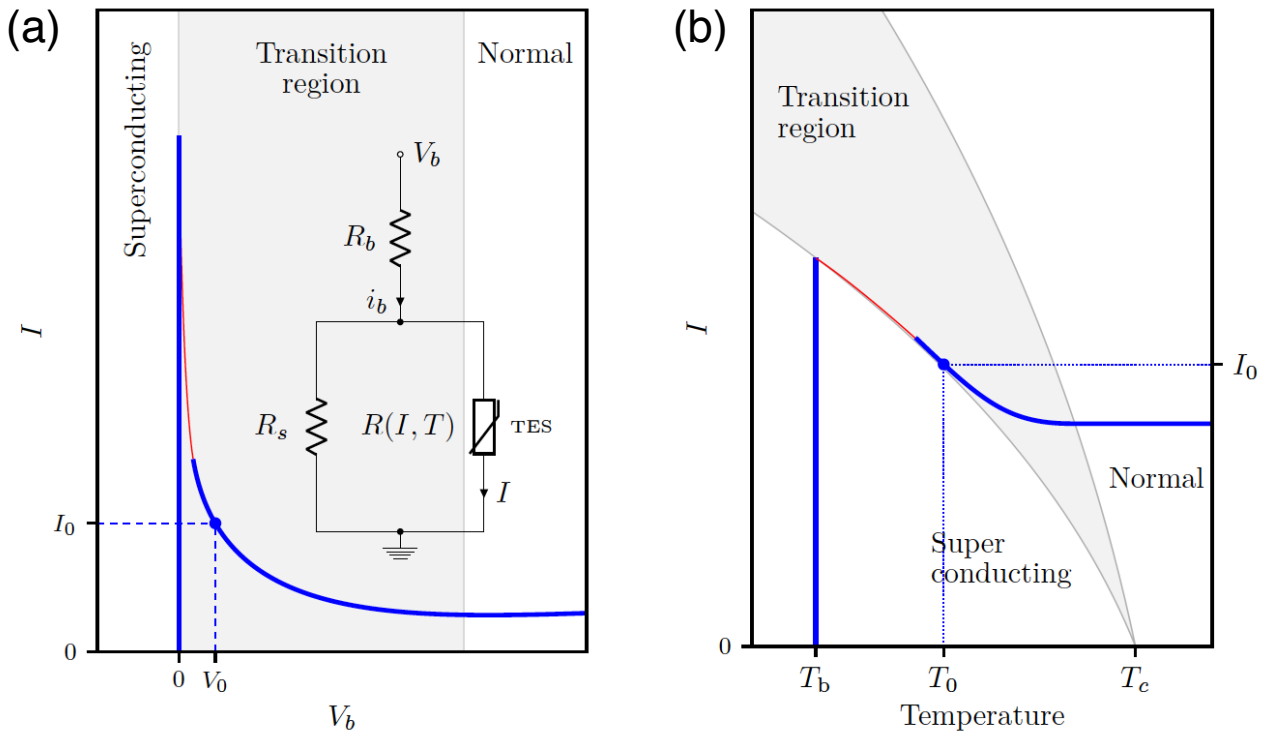

Figure A.1: Adjusting a Transition Edge Sensor (TES) for photon detection. (a) I *vs* V_b. (b) I vs Temperature. "Sensor trajectory as bias voltage is changed: At 0 V bias the sensor is at the bath temperature (T_b) well below its superconducting transition temperature (T_C) and has 0 resistance. When the bias voltage (V_b) is increased above 0 V the sensor current (I) rapidly increases until it reaches the critical value and the sensor enters the transition between the superconducting and normal phases. In the transition the sensor state can be considered a mixture of the superconducting and normal phases with the proportion of normal phase and resistance increasing with temperature. Current flowing through the the non-zero resistance dissipates power increasing the sensors temperature. For any fixed bias voltage the bias current (i_b) is also fixed, variation in the sensors resistance varies the sensor current I by changing the division of i_b between the sensor and the shunt resistance R_s. As I changes so does the power dissipated which in turn changes the sensor temperature. This feedback between current and temperature is known as electro-thermal feedback (ETF). For a fixed v_b, ETF acts to stabilise the TES at some equilibrium point int the phase diagram. The blue line indicates the trajectory of this equilibrium point through the phase diagram as v_b is increased. The equilibrium temperature increases and the equilibrium current decreases as v_b increases until the sensor leaves the transition and enters the normal resistance region. The thin red segments in the figures are regions where the no stable equilibrium exists. The bias voltage is adjusted to find the equilibrium point (I_0, T_0) that achieves the highest gain for converting temperature change into a current change." [211]. Credit of image: Dr. Gillett. [211].

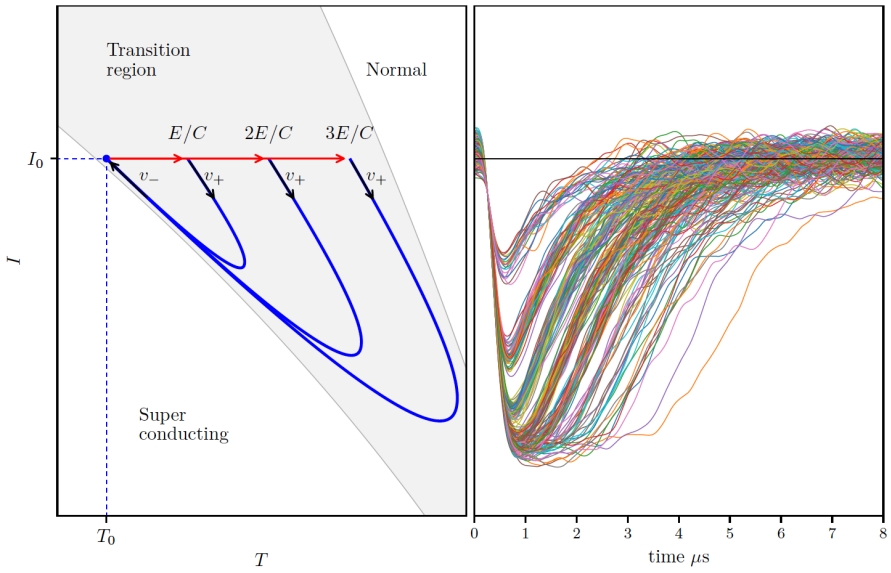

Figure A.2: The operation of a Transition Edge Sensor (TES) for photon detection. Left: conceptual description of the TES for photon detection under the small signal model. The TES absorbs a single photon with energy E, causing the sensor temperature to rise by E/C, where C is the heat capacity. The signs v_+ and v_- indicate the rise and fall, respectively, of the detection pulse. Right: Post-processed TES detection pulses for a coherent pulsed diode laser with wavelength ∼830 nm, 100 kHz repetition rate, and average photon number ∼2. Credit of image: Dr. Gillett. [211].

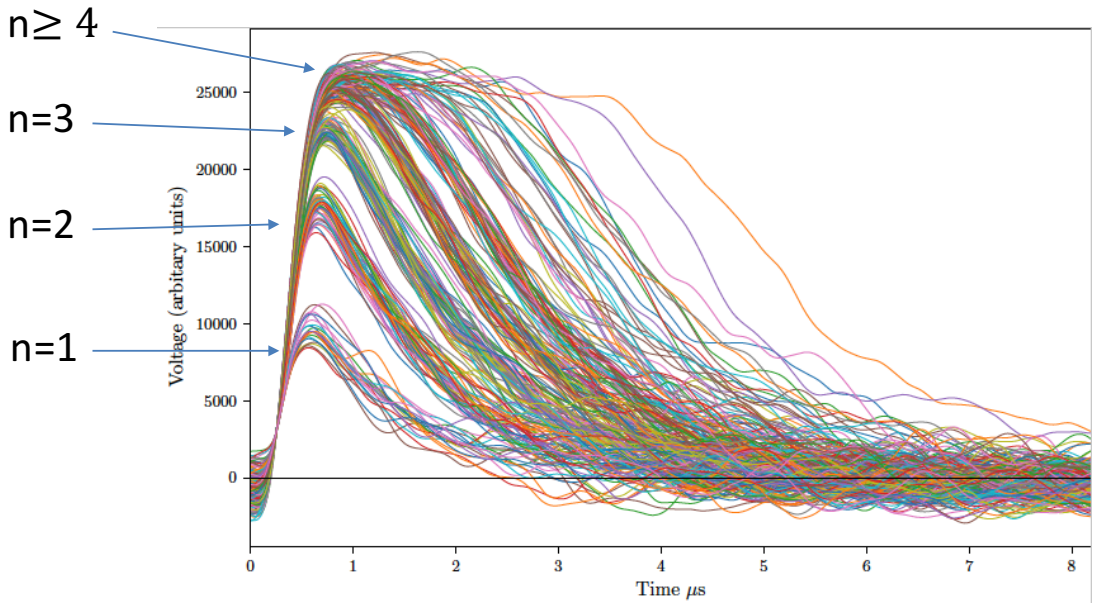

Figure A.3: Photon number-resolution from trace curves. From the right side of Fig. A.2, one can observe different structures each associate with a particular number of n photons. Here $n \geq 4$ are truncated together, however signal analysis can help to resolve a greater number of photons. Credit of image: adapted from Dr. Gillett. [211].

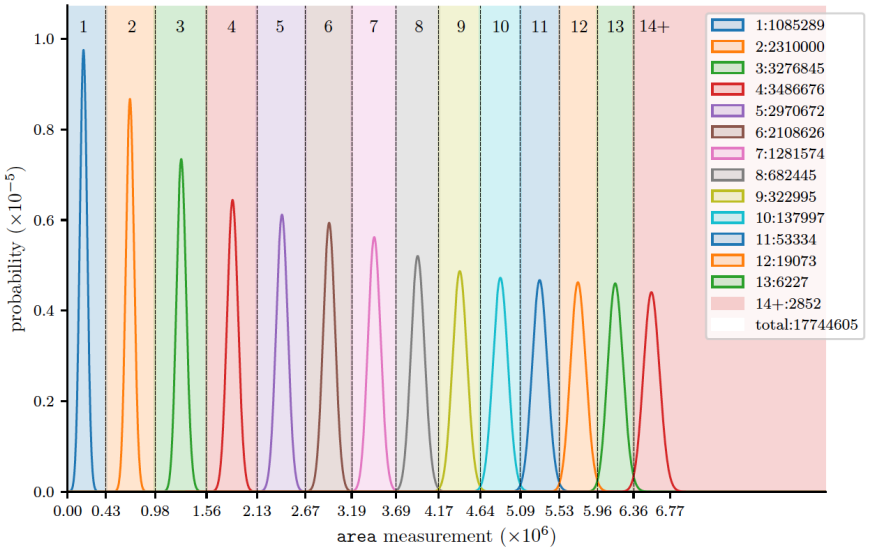

Figure A.4: TES photon counting. Using a 820 nm laser diode (coherent light) pulsed for 10 kHz and 2 nm spectrum filters, the TES calibration was executed and the final photon counting is presented. The legend box displays the number of detection events for each number of photons. Note that the data presented here comes from a different data set than Figures A.2 and A.3. Credit of image: Dr. Gillett. [211].

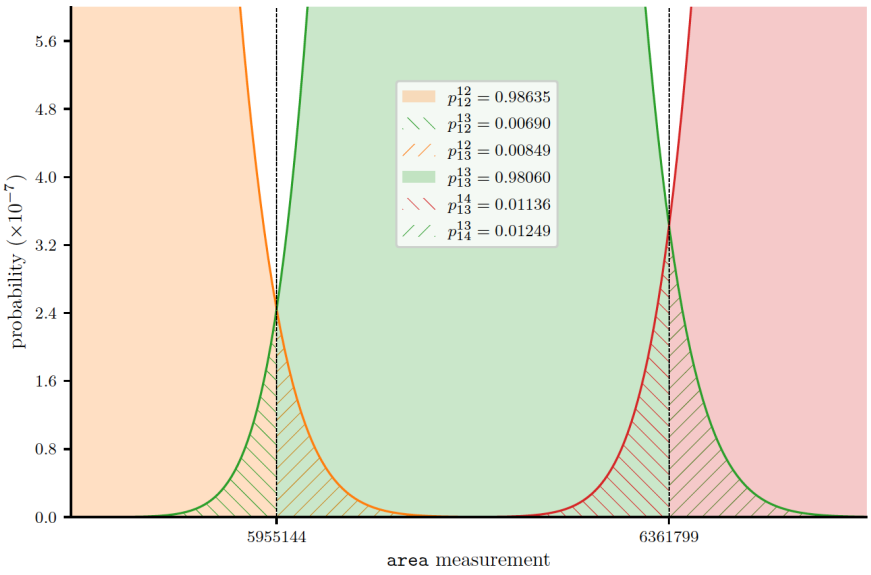

Figure A.5: Zoom in Fig. A.4. The legend notation p_n^f stands for "the probability of assigning photon number n to a measurement of Fock state f" [211]. For example, $p_{12}^{12} = 0.98635$ means that the probability of correctly assigning photon number $n = 12$ for a Fock state $f = 12$ is 98.635%, while $p_{12}^{13} = 0.00690$ means that the probability of incorrectly assigning photon number $n = 12$ for a Fock state $f = 13$ is 0.690%. The number resolution for low Fock states is even better. Credit of image: Dr. Gillett. [211].

A.3 TES metrics

In this section, we will comment on some of the metrics for using TES as photon detectors according to Reference [211]:

1. **Detection Efficiency:** TES are remarkably high efficient in terms of photon detection, and can reach above 95% detection efficiency [265]. This mean, that once a photon interacts with the TES, it has at least 95% chance of being detected. High efficiency can be a demand of some particular use of photon detectors. For example, to perform a detection loophole-free Bell Test, one needs to use highly efficient detectors [238–240, 266–270].

2. **Dark Counts:** TES have no dark counts, i.e., no intrinsic detection event caused by electronic noise. However, due to the high detection efficiency of TES, they also record detection events from stray light, or blackbody radiation (depending on TES response to particular frequencies), and those should not be confused with dark counts or ordinary single photon counts.

3. **Time Jitter:** as any detector, there is an uncertainty associated with the timing of the detection event. The TES system used at the Quantum Technology Laboratory at the UQ has an approximate 80 ns (FWHM) jitter.

4. **Recovery Time or Dead Time:** TES have no intrinsic recovery time, what means that TES can continuously detect single photons. However, in practical terms, TES present a *piled-up time*, i.e., when a new photon arrives at the TES before the detector has completely recovered from the previous photon detection. If this happens, TES can operate in a regime where they can no longer present number resolution. This is a kind of “blind by brightness”. For instance, to give a proper recovery time to our TES system, the experiment reported on Chapter 5 operates near 100 kHz.

Additionally, it is important to keep in mind that TES are not polarization sensitive.

STAT CRUX DUM VOLVITUR ORBIS